T.C.
MANISA CELAL BAYAR UNIVERSITY
GRADUATE EDUCATION INSTITUTE

M.Sc. THESIS
DEPARTMENT OF BIOENGINEERING
SCIENCE OF BIOENGINEERING

DISCOVERY OF NEW DRUG INGREDIENTS WITH HER2 PROTEIN SUPPRESSING EFFECT IN BREAST CANCER TREATMENT WITH MOLECULAR MODELING METHODS

Merve Yağmur UZAM

Supervisor
Asst. Prof. Dr. Deniz KARATAS

MANISA–2025

LETTER OF COMMITMENT

This thesis was prepared in accordance with the principles of scientific research and publication ethics within the Department of Bioengineering at Manisa Celal Bayar University, Institute of Graduate Education. All literature sources used in the study have been properly cited, and relevant information is presented within the bibliography. The thesis is entirely my own work, and no artificial intelligence applications or automated programming tools were used.

Merve Yağmur UZAM

ÖZET

Yüksek Lisans Tezi

Moleküler Modelleme Yöntemleriyle Meme Kanseri Tedavisinde HER2 Proteinini Baskılayıcı Etkiye Sahip Yeni İlaç İçeriklerinin Keşfi

Merve Yağmur UZAM

Manisa Celal Bayar Üniversitesi
Lisansüstü Eğitim Enstitüsü
Biyomühendislik Anabilim Dalı

Danışman: Dr. Öğretim Üyesi Deniz KARATAŞ

Moleküler modelleme, biyolojik sistemlerdeki moleküler etkileşimlerin bilgisayar destekli yöntemlerle incelenmesini sağlayan bir yaklaşımdır. Bu kapsamda moleküler docking, bir ligandın hedef moleküle bağlanma şeklini ve afinitesini öngörürken; moleküler dinamik simülasyonlar, bu etkileşimin zamana bağlı davranışını analiz eder. Her iki yöntem birlikte kullanıldığında, ilaç tasarımı ve biyomoleküler mekanizmaların anlaşılmasına yönelik güçlü ve bütüncül bir değerlendirme sunar. Bu çalışmada, meme kanserinde prognostik ve terapötik önemi bulunan HER2 (erbB-2) gen ekspresyonunun modülasyonu açısından, krill yağı kaynaklı omega-3 yağ asitleri EPA ve DHA ligandlarının potansiyel inhibitör etkileri araştırılmıştır. Çalışmanın sonuçları, krill yağı kaynaklı omega-3 yağ asitlerinin, HER2 aracılı proliferatif sinyalleşmeyi baskılayarak potansiyel hedef-ödaklı antineoplastik etkiler gösterebileceğini öne sürmektedir. Bu bulgular, moleküler docking ve dinamik simülasyon sonuçlarıyla desteklenerek, yeni HER2 inhibitörlerinin tasarımında DHA ve EPA türevlerinin alternatif ligand adayları olabileceğini ortaya koymaktadır.

Anahtar Kelimeler: moleküler docking, moleküler simülasyon, Autodock, gromacs, breast cancer, krill yağı

2025, 144 sayfa

ABSTRACT

M.Sc. Thesis

Discovery of New Drug Ingredients with HER2 Protein Suppressing Effect in Breast Cancer Treatment with Molecular Modeling Methods

Merve Yağmur UZAM

Manisa Celal Bayar University
Graduate Education Intitute
Department of Bioengineering

Supervisor: Asst. Prof. Dr. Deniz KARATAŞ

Molecular modeling is a computer-aided approach to study molecular interactions in biological systems. In this context, molecular docking predicts the binding pattern and affinity of a ligand to a target molecule, while molecular dynamics simulations analyze the time-dependent behavior of this interaction. When used together, both methods provide a powerful and holistic assessment for drug design and understanding biomolecular mechanisms. This study investigated the potential inhibitory effects of krill oil-derived omega-3 fatty acid ligands EPA and DHA in modulating HER2 (erbB-2) gene expression, which has prognostic and therapeutic importance in breast cancer. The results of the study suggest that krill oil-derived omega-3 fatty acids may exert potential target-oriented antineoplastic effects by suppressing HER2-mediated proliferative signaling. These findings, supported by molecular docking and dynamics simulation results, suggest that DHA and EPA derivatives may be alternative ligand candidates for the design of novel HER2 inhibitors.

Keywords: molecular docking, molecular simulations, Autodock, gromacs, breast cancer, krill oil

2025, 144 pages

FOREWORD AND ACKNOWLEDGMENTS

I would like to express my sincere gratitude to my esteemed advisor, Asst. Prof. Dr. Deniz Karataş, who guided me with his knowledge, academic guidance, and continuous support throughout all stages of my master's thesis and contributed with his experience and academic knowledge throughout my graduate education.

Merve Yağmur UZAM
Manisa, 2025

SYMBOLS AND ABBREVATIONS INDEX

EPA	Eicosapentaenoic Acid
DHA	Docosahexaenoic Acid
WHO	World Health Organization
BRCA1	Breast Cancer 1 Gene
BRCA2	Breast Cancer 2 Gene
ER	Estrogen Receptor
MD	Molecular Docking
MDS	Molecular Dynamic Simulation
LDL	Low-density
pH	Power of Hydrogen
PBC	Periodic Boundary Conditions
PME	Particle Mesh Ewald
BSE	Breast-Self Examinations
MRI	Magnetic Resonance Imaging
DCIS	Ductal Carcinoma *In Situ*
IDC	Invasive Ductal Carcinoma
LCIS	Lobular Carcinoma *In Situ*
ILC	Invasive Lobular Carcinoma
HER2	Human Epidermal Growth Factor 2
ER+	Estrogen Receptor Positive
PR+	Progesterone Receptor Positive
TNM	Tumor-Node-Metastasis
UICC	Union International Center Cancer
AJCC	American Joint Committee on Cancer
DNA	Deoxyribonucleic Acid
RNA	Ribonucleic Acid
FDA	Food and Drug Administration
CAF	Cyclophosphamide Adriamycin Fluorouracil
CMF	Cyclophosphamide Methotrexate Fluorouracil
TAC	Taxotere Adriamycin Cyclophosphamide
SERMs	Selective Estrogen Modulators
LH	Luteinizing Hormone

IC50	Half Maximal Inhibitory Concentration
PDB ID	Protein Data Bank Identification Number
UCSF Chimera	University of California, San Francisco Chimera
ChEMBL	Chemical Database of Bioactive Molecules
UniProtKB	Universal Protein Resource Knowledgebase
UHeM	The National Center for High Performance Computing
MSD	Mean Square Displacement
PubChem	Public Chemical Database
PDBQT	Protein Data Bank, Partial Charge (Q), Atom Type (T)
RMSD	Root Mean Square Deviation
RMSF	Root Mean Square Fluctuation
Rg	Gyration Radius

FIGURES INDEX

Page

TABLE INDEX

CONTENT

1. INTRODUCTION

Cancer refers to a group of disorders marked by the abnormal and uncontrolled growth of cells, resulting from genetic and epigenetic modifications.This disease can originate in any part of the body and has the capacity to invade surrounding tissues and metastasize to distant sites. The hallmark of cancer is the deviation of cells from their normal growth and programmed cell death cycles, leading to limitless replication. This process is facilitated by changes in genetic material as well as the influence of environmental factors (Brown et al., 2023).

Cancer is one of the oldest diseases known to humanity. One of the earliest written records, the Edwin Smith Papyrus dating back to around 1600 BCE, includes a description of breast cancer, which was considered incurable at the time. In the 5th century BCE, Hippocrates referred to tumors as "karkinos" and associated the disease with an excess of black bile. This humoral theory was later adopted by physicians such as Galen and remained the dominant explanation throughout the Middle Ages (Hajdu, 2011). With the advent of the Renaissance, advances in the study of human anatomy contributed to a better understanding of cancer. In the 18th century, Percivall Pott was the first to scientifically demonstrate the role of environmental factors in cancer development by linking scrotal cancer observed in chimney sweeps to exposure to soot (Hajdu, 2011). In the 19th century, the widespread use of the microscope facilitated the investigation of the cellular origins of cancer. Johannes Müller and Rudolf Virchow demonstrated that tumors arise from normal cells. Additionally, Virchow proposed that chronic inflammation could be a contributing factor in cancer development (Hanahan & Weinberg, 2000). In the 20th century, the genetic foundations of cancer began to be elucidated, with Theodor Boveri proposing that chromosomal abnormalities play a key role in cancer development. During this period, the association between tobacco use and lung cancer was statistically confirmed, highlighting the significance of environmental and lifestyle factors in cancer etiology (Sanchez-Cespedes et al., 2001). In the 1940s, chemotherapy was developed, with Sidney Farber successfully applying drug treatment to childhood leukemia. In 1971, U.S. President Richard Nixon launched the "War on Cancer" initiative, which significantly increased funding for scientific research in the field (DeVita & Chu, 2008). In the 2000s, research on the molecular biology of cancer was systematized

through the landmark article "The Hallmarks of Cancer." During this period, advances such as genetic profiling, targeted therapies (e.g., imatinib), and immunotherapies (including PD-1/PD-L1 inhibitors and CAR-T cell therapy) were developed. These innovations contributed to the emergence of personalized medicine as a central approach in cancer treatment (Hansford & Huntsman, 2014).

CHAPTER I. ORGANIZATION OF THESIS

1.1. Therapeutic and Biomedical Utilization of Marine Organisms in Health Sciences

Marine organisms have played a significant role in the treatment of various diseases throughout history, both in traditional and modern medicine. Written records from the Ancient Greek and Byzantine periods indicate that approximately 38 different marine invertebrate species were used in the treatment of digestive, dermatological, and urogenital disorders (Senthilkumar & Kim, 2013). Similarly, in regions such as West Africa, South America, and Southeast Asia, marine-derived products like sea turtle, dolphin oil, and sea snail have long been utilized in folk medicine as antipyretic agents, wound healers, or immune system enhancers. Since the 20th century, the therapeutic use of naturally derived agents from marine organisms has expanded considerably in modern pharmaceuticals. For instance, ω-conotoxin, isolated from the marine snail *Conus magus*, has been developed into a drug for chronic pain management (Molinski et al., 2009). Likewise, ecteinascidin 743 (trabectedin), derived from the marine tunicate *Ecteinascidia turbinata*, has been approved as an anticancer agent for the treatment of certain soft tissue sarcomas (Tremont et al., 1993). Modern studies on the sea cucumber (*Holothuria* spp.), which has been a long-standing component of traditional medicine in East Asia, have revealed its anti-inflammatory, immunomodulatory, and wound healing properties (Khotimchenko, 2018). These effects are primarily attributed to triterpene glycosides, which enhance immune responses by stimulating macrophage activity (Pislyagin et al., 2014). Additionally, sulfated polysaccharides such as fucoidan, extracted from marine algae, have attracted substantial interest in pharmaceutical research due to their antiviral, anticoagulant, and antitumor activities (Fitton, 2011). These examples, spanning from historical usage to

contemporary applications, highlight the growing importance of marine organisms not only in traditional knowledge systems but also as integral components of modern medical science.

1.1.1 Krill Oil: Structure and Health Applications

Krill oil is a valuable marine-derived lipid, primarily extracted from small crustaceans such as Antarctic krill (*Euphausia superba*). Its chemical composition is notably rich in omega-3 fatty acids, particularly eicosapentaenoic acid (EPA) and docosahexaenoic acid (DHA). A distinguishing characteristic of krill oil is that these omega-3 fatty acids are predominantly present in phospholipid form. This phospholipid structure is significant as it enhances bioavailability and facilitates more effective integration into cellular membranes when compared to the triglyceride form found in other marine oils (Sarıyer et al., 2025). Moreover, krill oil naturally contains the antioxidant pigment astaxanthin, which not only improves lipid stability by preventing oxidation but also contributes additional health-protective effects (Bunea et al., 2004).

Table 1.1. Chemical Structures and 3D Molecular Models of EPA and DHA

EPA (Eicosapentaenoic acid) PubChem CID 5282847	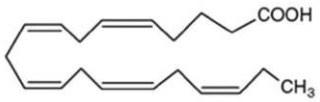	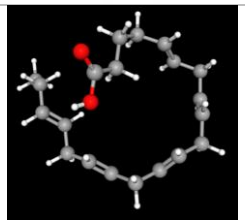
DHA (Docosahexaenoic acid) PubChem CID 45934466	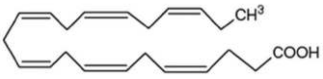	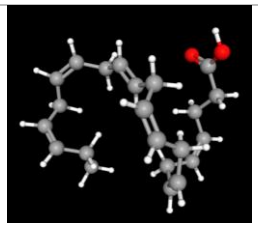

From a historical perspective, krill have traditionally been consumed as seafood, particularly in the Asia-Pacific region. However, the systematic extraction and use of krill oil for health purposes only began in the late 20th century. In recent decades, growing demand for omega-3 supplements and increasing interest in marine-based functional foods have led to the large-scale commercial production of krill oil.

Today, krill oil is widely available in both dietary supplement and pharmaceutical forms (Tou et al., 2007).

The health-related applications of krill oil are primarily attributed to its high EPA and DHA content. These fatty acids play a vital role in the prevention of cardiovascular diseases by improving lipid profiles—reducing total cholesterol, lowering low-density lipoprotein (LDL) levels, and decreasing triglyceride concentrations (Berge et al., 2014). Additionally, the anti-inflammatory properties of krill oil provide therapeutic benefits in managing metabolic disorders where chronic inflammation is a contributing factor. Research has explored its efficacy in alleviating symptoms of conditions such as rheumatoid arthritis and inflammatory bowel diseases (Deutsch, 2007). Moreover, krill oil exhibits neuroprotective effects that could help delay the advancement of neurodegenerative conditions like Alzheimer's disease. These effects are linked to the protective role of phospholipids in neuronal cell membranes and the oil's antioxidant capacity (J. H. Kim et al., 2020).

In addition, the potential dermatological benefits of krill oil have also been investigated. Due to its astaxanthin content, krill oil may protect skin cells against oxidative stress, thereby contributing to delayed signs of aging and enhanced wound healing (Berge et al., 2014). It has also been found to support joint health and aid in reducing symptoms of osteoarthritis (Deutsch, 2007).

.

CHAPTER II. GENERAL INFORMATIONS

Bioinformatics is an interdisciplinary scientific field that integrates computer science, statistics, and molecular biology for the purpose of collecting, storing, analyzing, and interpreting biological data. In the processing of large datasets related to biomolecules such as DNA, RNA, and proteins, algorithms, data mining techniques, and statistical analysis methods are widely employed (Thampi, 2009). The term "bioinformatics" was first introduced in 1970 by Paulien Hogeweg and Ben Hesper to describe the study of information flow and processing in biological systems (Hesper & Hogeweg, 2021). The foundation of bioinformatics as a discipline was established

through key developments such as the discovery of DNA's structure in molecular biology (1953) and the computational analysis of protein sequences (Hagen, 2000).

One of the pioneers in this scientific domain, Margaret O. Dayhoff, developed the first computerized systems for analyzing protein sequences during the 1960s and published the seminal work "Atlas of Protein Sequence and Structure." She also introduced the PAM (Point Accepted Mutation) matrix (Dayhoff et al., 1978), which laid the groundwork for modern protein sequence databases and alignment algorithms. Subsequent advancements included the CLUSTAL-W and CLUSTAL-X algorithms, developed by Desmond G. Higgins and Toby Gibson, which revolutionized multiple sequence alignments and remain widely used today (Higgins & Sharp, 1988). Similarly, large-scale protein function prediction studies led by Edward M. Marcotte and colleagues significantly contributed to the development of systems biology (Marcotte et al., 1999).

Currently, bioinformatics is utilized across diverse fields. In genomics, it supports mutation analyses and genome-wide association studies (GWAS) based on DNA sequencing data; in proteomics, it facilitates protein structure prediction, homology modeling, and molecular docking studies (Jumper et al., 2021). In clinical medicine, bioinformatics analyses have enabled the diagnosis of genetic diseases and the development of personalized treatment strategies (Collins & Varmus, 2015). In agriculture, the analysis of plant genomes, identification of genetic variations, and biotechnological interventions are also carried out using bioinformatics tools (Varshney et al., 2005). Additionally, microbial genomics and metagenomics research are supported by bioinformatics infrastructures. Recently, artificial intelligence-driven bioinformatics applications have gained prominence, especially with the advent of DeepMind's AlphaFold model, which marked a breakthrough in protein structure prediction by achieving outstanding results in the CASP14 (Jumper et al., 2021).

In summary, bioinformatics aims to integrate biology, computer science, and mathematics to make sense of large biological datasets. It has become indispensable in both fundamental research and applied medicine. Its applications are expanding across a wide spectrum, from genome sequencing and structural biology to drug design and environmental biotechnology.

Molecular modeling is a computer-based approach that simulates the geometry, energy profiles, and dynamic behavior of biomolecular systems at the atomic level based on force fields and physical laws . Bioinformatics, on the other hand, is an interdisciplinary field that enables the storage, analysis, and algorithmic execution of structural predictions and modeling for large datasets pertaining to biomolecules such as DNA, RNA, and proteins. Molecular modeling plays a critical role within bioinformatics, particularly in structural genomics, protein structure prediction, and folding simulations (Thampi, 2009).

The integration of molecular modeling with bioinformatics offers a broad range of applications, from biological data analysis and three-dimensional protein structure prediction to ligand-receptor interaction studies and virtual screening. AI-supported structural prediction methods, especially deep learning-based systems like AlphaFold, have accelerated the integration of molecular modeling outputs into bioinformatics platforms and helped fill knowledge gaps in protein folding (Jumper et al., 2021).

The historical development of molecular modeling traces back to molecular mechanics theories of the 1940s, with Westheimer's 1946 work laying the foundation (Schlick et al., 2011).

In the 1960s, scientists such as Lifson, Scheraga, and Warshel developed systematic force fields utilizing quantum chemical data, while Levitt and Lifson applied energy minimization techniques to protein molecules in 1969 (Schlick et al., 2011).

During the 1970s, Rahman and Stillinger performed the first molecular dynamics simulations on water molecules (Schlick et al., 2011). In the 1990s, docking programs such as DOCK and AutoDock began modeling ligand-receptor interactions using Monte Carlo and genetic algorithms; in the 2000s, homology modeling tools like MODELLER and I-TASSER became popular (Rakhshani et al., 2018).

Molecular modeling provides numerous advantages, including lower cost and time requirements compared to experimental methods, atomic-level mechanistic insights, virtual screening and optimization capabilities in drug discovery, prediction of mutation effects, and simulation of diverse scenarios (Schlick et al., 2011).

Table 2.1. Main types of molecular modeling.

Energy minimization (Molecular Mechanics)	The determination of stable conformations of molecules using force fields and Hooke-type bond terms. (Schlick et al., 2011)
Molecular dynamics (MD) simulations	The modeling of the time-dependent behavior of a system through atomic motions based on Newton's equations of motion, enabling the study of phenomena such as protein folding and folding kinetics. (Schlick et al., 201)
Docking / virtual scanning	The modeling of ligand-receptor binding modes and the estimation of binding energies are utilized for virtual screening purposes in drug design (Kamal & Chakrabarti, 2023).
Homology modeling / structural prediction	The prediction of three-dimensional structures of novel proteins based on reference to known homologous structures (Sali & Blundell, 1993).
Quantum mechanical (QM) methods	The calculation of reactions involving bond formation and cleavage at the electronic level; the investigation of chemical processes such as enzymatic reactions (Náray-Szabó et al., 2013).

Modeling techniques are primarily divided into two main categories: force field-based classical methods and quantum mechanics-based methods. Force field approaches describe atoms as point charges and mass centers, calculating the system's potential energy based on bond lengths, bond angles, torsional angles, van der Waals forces, and electrostatic interactions. Molecular mechanics (MM) falls within this category and is used to determine stable structures of the system through energy minimization. Molecular dynamics (MD) simulations, on the other hand, compute the time-dependent movements of atoms based on Newton's equations of motion and are widely applied to study protein folding, ligand binding, and the behavior of biomolecular complexes (Jing et al., 2019).

Monte Carlo (MC) simulations perform random sampling of structures based on statistical sampling methods and are particularly utilized in thermodynamic calculations, phase transitions, and exploration of energy surfaces. Molecular docking

is a technique aimed at predicting how and with what binding energy a ligand associates with a specific target molecule. During this process, interactions between the ligand and receptor are evaluated using various scoring functions to identify the most favorable binding mode. Software such as AutoDock, AutoDock Vina, and GOLD are widely employed for this purpose (Rakhshani et al., 2018).

Homology modeling aims to predict the structures of novel proteins by referencing homologous proteins with known structures. This approach is crucial for estimating the three-dimensional structures of proteins that have not yet been resolved through experimental methods and is implemented by tools such as MODELLER and SWISS-MODEL. Quantum mechanical (QM) methods enable calculations at the electronic level of molecular systems and are particularly used to investigate chemical reaction mechanisms. Additionally, QM/MM hybrid approaches, which treat the active site quantum mechanically and the remainder of the system with molecular mechanics, allow for detailed analysis of complex biological processes (Sali & Blundell, 1993).

2.1. Principles of Molecular Docking

Molecular docking is a method for computationally predicting how a small molecule (ligand) binds to a specific biological target (usually a protein). This technique was developed to assess how the ligand positions itself within the target structure, the conformations in which it can bind, and the strength of this binding. The primary goal is to find the optimal binding position and analyze the interactions at this position using energy-based evaluation systems (scoring functions) (Huang et al., 2010).

The molecular docking process typically comprises three main steps: sampling, scoring, and ranking. During the sampling phase, various possible binding modes and orientations of the ligand on the receptor surface are generated. Subsequently, each conformation is evaluated energetically using scoring functions. These functions estimate the binding free energy, thereby predicting the strength of the ligand's interaction with the target. In the final step, the conformations are ranked, prioritizing those with the lowest estimated binding energies (Huang et al., 2010).

Initially, molecular docking was applied to fixed structures, where both the ligand and receptor were assumed rigid. However, over time, models developed to consider the flexibility of molecules during binding. This approach, known as "induced fit," offers more realistic results by predicting that the receptor can change shape at the binding site (Lexa & Carlson, 2012).

Today, molecular docking plays a crucial role, particularly in drug design and virtual screening studies. During the discovery of new drug candidates, large molecular libraries can be screened using docking algorithms to identify compounds with the most favorable binding affinities. This approach offers significant advantages in terms of time and cost efficiency by narrowing down potential candidates prior to experimental validation (Ferreira et al., 2015).

Docking applications are not limited to analyzing interactions between small molecules and proteins. They can also be adapted to model protein–protein, protein–nucleic acid, and protein–carbohydrate interactions. With advances in technology, artificial intelligence-assisted scoring functions are increasingly being integrated into docking workflows, thereby enhancing the accuracy of molecular interaction modeling (Pagadala et al., 2017).

Two fundamental models stand out in the field of molecular docking: the lock-and-key model and the induced fit model (Figure 2.1). In the lock-and-key model, the ligand fits perfectly into a predetermined, unchanging structure specific to the target molecule's binding site. This model assumes a rigid binding surface and is based on simple structural pairings. On the other hand, the inducible fit model proposes that conformational changes occur in the target molecule's binding site during ligand binding. This results in more flexible binding, and molecules can mutually change shape, resulting in higher affinity. Currently, more realistic and dynamic binding models are being developed in molecular docking studies, taking into account protein flexibility and ligand mobility, thereby improving accuracy in drug discovery processes (Tripathi & Bankaitis, 2017).

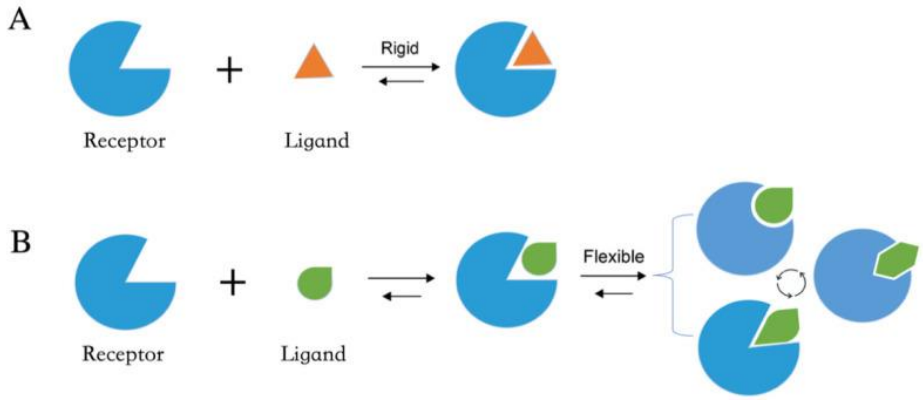

Figure 2.1. Molecular Docking Models: (A) Lock and Key Model, (B) Induced Fit Model (Yang et al., 2022).

2.2. Protein-Ligand Docking

Protein-ligand docking is a structure-based computational method for predicting the binding strength and position of a ligand on a target protein. This method is critical for drug design and understanding biomolecular interactions. The docking process generally consists of three stages: sampling, scoring, and ranking (Table 2.2). In the sampling stage, different conformations of the ligand at the target binding site are modeled. These conformations are analyzed with energy-based scoring functions that evaluate binding affinities. In the final stage, the ligand positions are ranked according to their binding energy to determine the most likely binding mode (Meng et al., 2011).

Table 2.2. Schematic of protein-ligand classification (Sousa et al., 2006).

Name of Steps	**Explanation**	**Methods**
Sampling	Examples of positions created when docking the ligand to the target site	Systematic search, Monte Carlo, Genetic algorithms, soft keter, flexible side chain
Scoring	Calculating the binding energy of each position	Physical (force field), empirical, knowledge-based, ML-based scoring functions
Ranking	Selecting the best conformations based on scoring functions	Ranking with RMSD, energy, MSP, ML based methods

The most well-known docking models are the "lock and key" model and the "induced fit" model. The lock and key model assumes that the ligand binds to the target

structure in only a specific manner, while the inducible fit model considers flexibility in both the ligand and receptor structures. This model allows for simulating conformational changes that occur in the protein structure during ligand binding (Yang et al., 2022).

Today, molecular docking systems utilize machine learning-based scoring functions in addition to classical methods. These advancements allow for higher accuracy in predicting binding positions and affinities. Protein-ligand docking, particularly in virtual screening processes, allows for rapid and systematic analysis of hundreds of thousands of compounds, significantly reducing the cost and time of experimental studies (Meng et al., 2011).

2.3. Molecular Dynamics: Principles and Techniques

Molecular dynamics (MD) simulations are a computational approach that applies Newton's second law of motion to investigate how molecular systems evolve over time (Badar, Shamsi, & Ahmed, 2022). This method allows for the modeling of biomolecules at the atomic level, enabling detailed investigation of biological phenomena such as protein folding, ligand binding processes, and enzymatic mechanisms (Hollingsworth & Dror, 2018).

MD simulations begin with the preparation of the system; during this phase, the atomic coordinates, bonds, angles, charges, and initial velocities are defined (Friedrichs et al., 2009). The forces between atoms are then determined, and how they move over time under the influence of these forces is calculated. This process is typically performed using time integration algorithms such as Verlet or leapfrog, with time steps on the order of femtoseconds (10^{-15} s). Potential energy functions form the basis of molecular dynamics simulations, and these functions are generated by force fields that describe the interactions between atoms. Commonly used force fields include AMBER, CHARMM, and GROMOS. These models generate the energy profile of the system by describing interatomic bond lengths, angles, torsions, and van der Waals or electrostatic interactions (Badar et al., 2022).

MD simulations historically began in the 1950s with the modeling of simple systems and experienced a significant turning point with the simulation performed by Rahman and Stillinger on the water molecule in 1960. Ab initio simulations, developed

by Car and Parrinello in the 1980s and based on quantum mechanics, emerged as an alternative to classical approaches (Kühne et al., 2007).

While all atoms are explicitly modeled in classical MD simulations, coarse-grained models represent groups of atoms as single units, reducing computational costs. For more complex systems, quantum mechanical molecular dynamics (e.g., ab initio or Car–Parrinello MD) methods are preferred. These methods include electrons, allowing detailed analysis of chemical reactions such as bond formation and breaking (Kühne et al., 2007). MD simulations have also been enriched with QM/MM (quantum mechanical/molecular mechanics) approaches. In these methods, the active region of the system is represented quantum mechanically, and the rest is represented classically mechanically. This reduces computational costs and allows for accurate simulation of chemical reactions (Badar et al., 2022).

The advantages of MD include providing detailed information at the atomic level, allowing observation of transient structures not obtainable by experimental methods, and enabling thermodynamic and kinetic analyses. However, it also has limitations, such as high computational cost, timescale limitations, and the accuracy of the force fields used. To overcome these limitations, parallel computing techniques, enhanced sampling methods (e.g., metadynamics), and machine learning-based simulation systems are widely used today. Figure 2.3 summarizes the MD simulation process (Martyna et al., 1999).

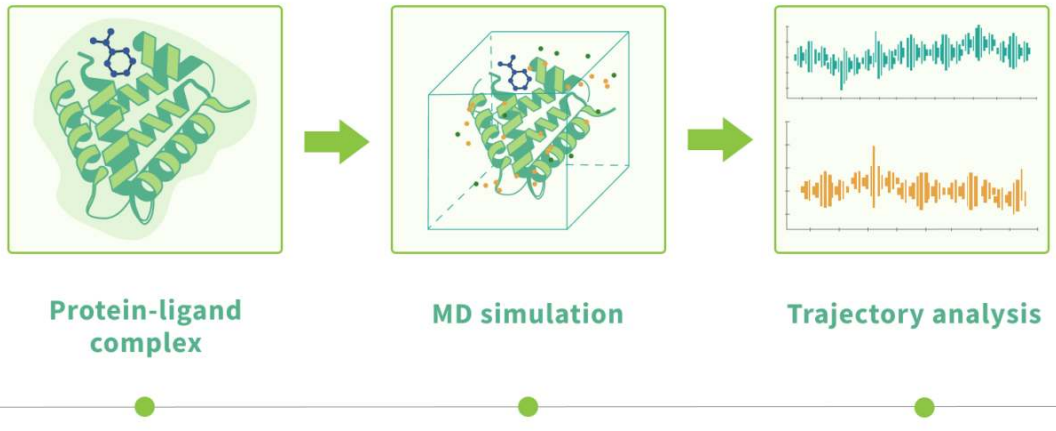

Figure 2.2. MD simulation process (*(6) Molecular Dynamics Simulations: Concepts and Applications | LinkedIn*, n.d.).

Molecular dynamics (MD) simulations are powerful computer-based methods that enable the understanding of biological processes at the micromolecular level in the healthcare field. They offer critical clinical benefits, particularly by examining protein-ligand interactions, the flexibility of drug target structures, and the dynamic behavior of drug candidates (Mortier et al., 2015).

During the COVID-19 pandemic, MD simulations have become a fundamental method used in many studies, from drug discovery to target identification. For example, Aris and colleagues evaluated the interaction of griseofulvin and its derivatives with the SARS-CoV-2 protease enzyme using MD and demonstrated potential therapeutic potential. Similarly, a study analyzing the binding stability of natural inhibitors to the ACE2 receptor using MD simulations yielded stable ligand-receptor complexes for compounds such as cinnamic acid, thymoquinone, and andrographolide, indicating the therapeutic potential of these natural molecules (Aris et al., 2022).

In a study conducted within the framework of drug repurposing, the binding stability of FDA-approved drugs to SARS CoV-2 Mpro protease was tested by MD; candidates such as Simeprevir, Ergotamine, Bromocriptine and Tadalafil formed stable complexes over time and were analyzed as indicators of suitable binding energies (Ray et al., 2022).

MD simulations are valuable not only for drug discovery but also for membrane permeation and pharmacokinetic prediction. Ghaed Sharaf & Omidvar (2022) analyzed the permeation dynamics of COVID-19 drugs such as favipiravir and hydroxychloroquine through the cell membrane using MD and DFT, demonstrating that favipiravir has a lower free energy barrier and greater membrane permeability (Ghaed-Sharaf & Omidvar, 2022).

The table below summarizes examples of the use of MD simulations in clinical research:

Table 2.3. Protein-ligand classification

Application Area	Explanation	Methods
	Griseofulvin derivatives MD in SARS CoV 2	Estimation of enzyme inhibition potential

COVID 19 therapeutic discovery	protease (Aris et al., 2022)	
ACE2 modulation by natural inhibitors	Cinnamic acid, thymoquinone specific ligand ACE2 stability (Aris et al., 2022)	Potential to block cell entry
Drug repurposing	Mpro binding for agents like Simeprevir, Ergotamine, Tadalafil (Kumar et al., 2020)	Repurposing approved drugs for COVID-19 treatment
Membrane permeability studies	Favipiravir and HCQ transition dynamics (Ghaed Sharaf & Omidvar, 2022)	Prediction of drug pharmacokinetic properties

2.3.1. Computational Algorithms in MD Simulations

The computational algorithms used in Molecular Dynamics (MD) simulations are crucial for simulation accuracy, stability, and computational efficiency. These algorithms primarily encompass functions such as time integration, force calculation, thermodynamic control, and sampling acceleration.

First, time integration algorithms provide numerical solutions of Newton's equations of motion. The Störmer–Verlet algorithm and its derivatives, the Leapfrog and Velocity Verlet algorithms, are widely used in simulations. These methods offer stability in long-term simulations thanks to their energy-conserving and symmetric structures (Mazur, 1997). The Beeman algorithm, on the other hand, improves kinetic energy calculations by increasing accuracy, particularly in velocity estimation (Amini et al., 1987).

The calculation of electrostatic and long-range forces is a critical step in MD simulations. The Ewald Summation method is a classical algorithm used to calculate long-range Coulombic interactions under periodic boundary conditions. Nevertheless, because of the intensive computational demands, modern simulations tend to favor FFT-based accelerated methods like Particle Mesh Ewald (PME) and Smooth Particle Mesh Ewald (SPME). These algorithms significantly reduce computational time while

preserving the accuracy of the electrostatic interactions in the system (Essmann et al., 1995).

Neighbor list algorithms (Verlet list and cell list) are used to calculate short-range forces. These methods quickly determine whether atom pairs are within a certain cutoff distance, preventing unnecessary computations and improving simulation efficiency (Rapaport, 2004).

Various thermostat and barostat algorithms have been developed for thermodynamic control. The Nosé–Hoover thermostat provides a deterministic temperature control mechanism for the canonical (NVT) ensemble, while Langevin dynamics achieves thermal equilibrium using stochastic forces. As barostats, the Parrinello-Rahman and Martyna-Tobias-Klein algorithms provide pressure control and can dynamically adjust the system volume, particularly under isobaric (NPT) conditions (Martyna et al., 1994).

Advanced sampling techniques are also used to increase the efficiency of MD simulations. The Replica Exchange Molecular Dynamics (REMD) method facilitates overcoming energy barriers by performing parallel simulations at different temperatures. Metadynamics, on the other hand, accelerates the discovery of new conformations by adding bias to collective variables. In recent years, machine learning-assisted adaptive sampling techniques have also been the subject of research and have been used to speed up simulations and increase sampling efficiency (Bernardi et al., 2015). Table 2.4 provides a general summary of the relevant methods.

Table 2.4. Overview of Computational Methods in Molecular Dynamics

Time Integration Algorithms	Verlet (Störmer–Verlet) Algorithm, Leapfrog, Verlet Algorithm, Velocity Verlet Algorithm, Beeman Algorithm, Gear Predictor-Corrector Algorithm
Electrostatic and Long-Range Force Calculation Algorithms	Ewald Summation, Particle Mesh Ewald (PME), Smooth Particle Mesh Ewald (SPME), Reaction Field Method, Fast Multipole Method (FMM)

Short-Range Force and Neighbor List Algorithms	Verlet List, Cell Linked
Thermostat Algorithms (Temperature Control)	Berendsen Thermostat, Nosé–Hoover Thermostat, Langevin Dynamics, Andersen Thermostat
Barostat Algorithms (Pressure Control)	Berendsen Barostat, Parrinello-Rahman Barostat, Martyna-Tobias-Klein (MTK) Barostat
Advanced Sampling and Acceleration Techniques	Replica Exchange Molecular Dynamics (REMD), Metadynamics, Simulated Annealing, Accelerated Molecular Dynamics (aMD), Adaptive Sampling / Machine Learning Driven Sampling

2.4. Integrative Role of Molecular Docking and Molecular Dynamics Simulations in the Drug Discovery

Molecular modeling methods are frequently used in modern drug discovery processes to reduce experimental burden and increase the efficacy of targeted therapies. Molecular docking and molecular dynamics (MD) simulations, in particular, play critical roles in elucidating both the static and dynamic aspects of ligand-protein interactions. Integrating these two approaches increases the accuracy of binding affinity predictions and allows for a more reliable assessment of the pharmacological potential of candidate molecules (Ferreira et al., 2015; Meng et al., 2011).

Molecular docking is a structure-based computational method used to predict the binding pattern and binding affinity of small molecules to biological targets (mostly proteins). This method offers significant advantages in preliminary screening of potential inhibitors by determining the optimal conformation and position of the ligand on the target protein. Docking algorithms typically approximate the free energy of the ligand-protein complex based on scoring functions. However, these calculations are often performed on static crystal structures and take limited account of the flexibility of proteins (Pagadala et al., 2017).

At this point, molecular dynamics simulations play a critical role in assessing the stability, structural changes, and binding behavior of the resulting complexes over time after docking. MD simulations provide time-varying structural information at the atomic level, allowing us to observe the protein's conformational flexibility and the

ligand's behavior at the binding site. This allows us to correct potential binding modes or weakly predicted interactions overlooked in docking analyses (Hollingsworth & Dror, 2018).

The integration of docking and molecular dynamics (MD) simulations is employed throughout multiple phases of the drug discovery pipeline, including virtual screening, lead optimization, structure-guided drug design, and toxicity assessment. This combined approach offers significant advantages in areas such as docking. For example, when the molecules with the highest scores are subsequently subjected to MD simulation, molecules that exhibit binding stability not only in static configurations but also in dynamic environments are selected, further enhancing the process of drug candidate identification (Geromichalos, 2007).

Furthermore, this integrative approach plays an important complementary role in the field of structural bioinformatics. In particular, the combined use of MD simulation platforms such as Gromacs, AMBER, and NAMD with docking software such as Autodock, Glide, and GOLD enables atomic-level mechanistic predictions and reduces the need for experimental validation (Gioia et al., 2017).

2.5. Breast Cancer: An Assessment of Historical Development, Epidemiology, and Risk Factors

Breast cancer stands out as one of the oldest known diseases throughout history. The Edwin Smith Papyrus, dating back to 1600 BC in ancient Egypt, states that breast lumps are incurable and often fatal. Pioneers in medical history, such as Hippocrates and Galen, linked breast cancer to the accumulation of "black bile" (melancholia), a phenomenon that persisted throughout the Middle Ages. However, the first systematic scientific evaluations of breast cancer began in the 19th century, and with the development of histopathological classifications and microscopy techniques, the disease began to be better understood. By the 20th century, the effects of hormonal factors, genetic predispositions, and environmental factors on breast cancer began to be investigated using epidemiological methods (Lukong, 2017).

At present, breast cancer is the most commonly diagnosed malignancy among women worldwide. Based on GLOBOCAN 2020 statistics, around 2.3 million women are diagnosed annually, making up about 11.7% of all cancer cases. Worldwide, breast cancer stands as the second leading cause of cancer-related deaths among women, accounting for over 685,000 fatalities. This burden impacts not only healthcare systems but also societal and economic structures. Breast cancer incidence rates vary significantly across geographic, socioeconomic, and cultural factors. Although breast cancer diagnosis rates are high in developed countries, mortality rates are low thanks to early diagnosis and effective treatment protocols. In contrast, despite lower incidence rates in low- and middle-income countries, high mortality rates are associated with limited access to healthcare services, inadequate screening programs, and late diagnosis. Figure 2.3 shows the highest and lowest breast cancer incidence and mortality rates by country as of 2020. According to the table, the normalized incidence ratio (ASIR), for example, is 112/100,000 in Belgium, while it is around 36/100,000 in lower-incidence countries like Iran. Life expectancy and new diagnosis rates vary significantly between countries (Sung et al., 2021).

Figure 2.3 provides a comparative overview of female breast cancer incidence and mortality rates across various global regions, age-standardized to the world population as of 2018. Regions are ordered by decreasing incidence rates, while peak national values within each region are indicated to emphasize intra-regional disparities.

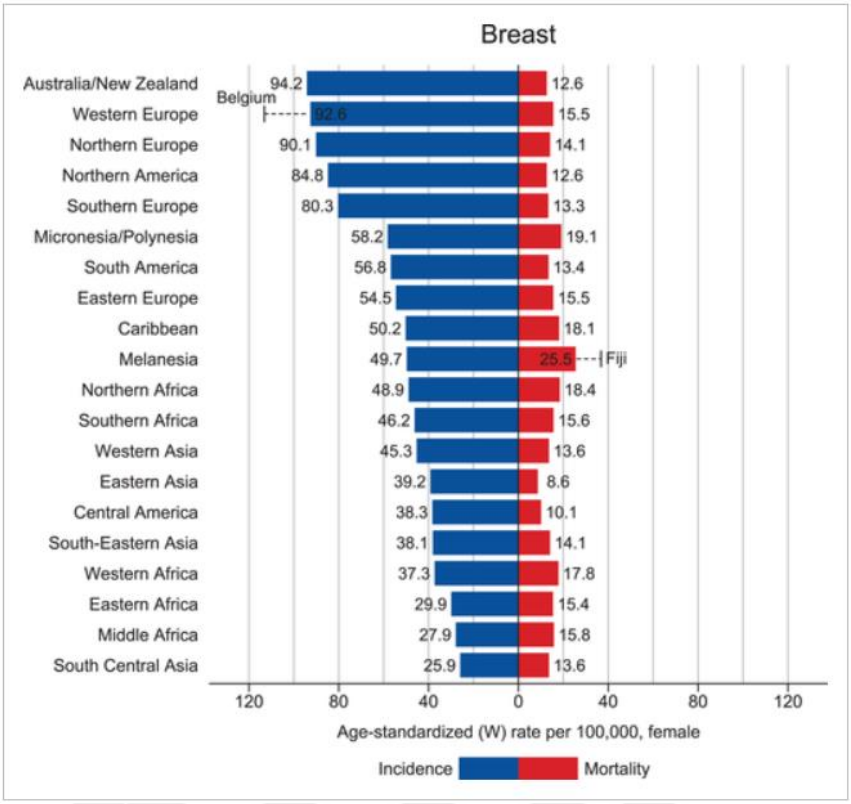

Figure 2.3 Breast Cancer in Women: Regional Distribution of Global Incidence and Mortality

In Turkey, breast cancer is the most commonly diagnosed form of cancer in women. According to the Turkish Cancer Statistics, breast cancer constitutes approximately 24% of all cancer cases among women. In Turkey, the disease is typically diagnosed at a younger age, with the average age at diagnosis being 49. This rate is approximately 10-14 years earlier than in Western countries and is thought to be due to genetic, environmental, or cultural factors. A large cohort study conducted at Istanbul University Faculty of Medicine evaluated the clinical data of more than 6,000 women and demonstrated that young diagnosis is common. The incidence of breast cancer in Turkey varies by region; while the rate is close to 50 cases per 100,000 people in western provinces, this rate is below 20 in eastern provinces. This disparity is believed to be associated with differences in lifestyle, reproductive factors, and levels of awareness regarding cancer screening. (Bayrakçeken et al., 2024).

Risk factors for breast cancer include increasing age, inherited mutations in the BRCA1 and BRCA2 genes, a family history of the disease, early menarche, late menopause, advanced age at first childbirth, nulliparity, alcohol consumption, obesity, physical inactivity, and the use of hormone replacement therapy. Additionally, breast

tissue density is also a risk factor and can affect the sensitivity of screening methods. At the molecular level, breast cancer is categorized into distinct subtypes, including hormone receptor-positive (estrogen receptor [ER+] and/or progesterone receptor [PR+]), human epidermal growth factor receptor 2-positive (HER2+), and triple-negative breast cancer (TNBC). This classification is important for treatment planning and prognosis (Bayrakçeken et al., 2024).

Recent epidemiological studies indicate that breast cancer mortality increases with age. The Global Burden of Disease study, spanning the period from 1990 to 2021, reported a notable rise in breast cancer-related mortality rates among women aged 70 years and above. This increase is explained by the increased complexity of diagnosis and treatment in this age group and the associated comorbidities (Liu et al., 2024). A similar analysis conducted in Turkey noted that age-standardized mortality ratios (ASMR) increased from 12.26 in 1990 to 12.65 in 2019, with this increase particularly concentrated among women aged 70 and older. However, a decrease in mortality rates was observed in the 50–69 age group, which was partially attributed to the impact of screening programs targeting this age group (Yekdeş et al., n.d.).

However, the effectiveness of screening programs varies across countries. National screening programs in Turkey recommend biennial mammography for women aged 40–69, but participation rates are below 30%. A 2024 study reported clinical breast examination rates of 8.9%, self-examinations of 11.8%, and mammography rates of 11.3%. These low rates have been linked to a lack of awareness, education level, socioeconomic status, and distrust in the healthcare system (Bayrakçeken et al., 2024).

Table 2.5. Breast cancer risk factors.

Risk Factor	**Effect / Protective Effect**	**Source**
Positive Family History	OR = 4.67–5.7 times increase	(Farooq & Ilyas, 2023)
Smoking	OR ≈ 1.75 (Sivas); $p < 0.05$ (Ankara)	('Breast Cancer Risk Factors in Turkey', 2011)
Early Menarche (<15 years)	OR = 1.72	(Kuru et al., 2002)

First Birth ≥30 Years of Age	OR = 2.86	(Kuru et al., 2002)
Oral Contraceptive Use	OR = 1.51	(Kuru et al., 2002)
Menstrual Irregularity	OR = 1.61	(Kuru et al., 2002)
Long-Term Breastfeeding (>5 years)	OR = 0.31 (protector)	(Kuru et al., 2002)
HRT (>36 months use)	Significant increased risk	('Breast Cancer Risk Factors in Turkey', 2011)
Fast Food/Low Fiber–Vitamin Intake	Increased risk / Fiber & vitamin C as a protective effect	(Alim & Kiziltan, 2016)

2.5.1. Structural Features of Breast Tissue

The human breast is situated between the second and sixth ribs, extending laterally from the sternum to the midaxillary line. The breast, resting on the fascia of the pectoralis major muscle, is nestled between the superficial and deep fascial layers. This anatomical structure is anchored to the skin by Cooper's ligaments, connective tissue bands that provide structural support and help preserve the breast's shape. (Duncan et al., 2022).

The breast is composed of three primary components: glandular (secretory), stromal (connective and fatty tissue), and vasculo-lymphatic structures. The glandular structure consists of small mammary glands called lobules and the lactiferous ducts (ductus lactiferi) that carry these lobules to the nipple. The glandular tissue consists of units called terminal duct lobular units (TDUs). This structure is the starting point for many types of breast cancer (Cieśla et al., 2020).

The breast parenchyma (functional tissue) consists of 15–20 lobules, arranged radially around the areola. Each lobule is composed of smaller lobules, which contain groups of alveolar cells. The lobules consist of lactating epithelial cells and

surrounding myoepthelial cells. Myoepthelial cells have contractile properties to facilitate milk flow (Cieśla et al., 2020).

Stromal tissue is the supportive connective tissue surrounding the glandular tissue. This structure contains fibroblasts, collagen fibers, fat cells, and immune cells. The majority of breast volume consists of adipose tissue; the proportion of glandular tissue varies from person to person, depending on age, hormonal status, and menopause (Duncan et al., 2022).

Cooper's ligaments are fibrous structures that extend from the deep fascia through the glandular and stromal tissue to the subcutaneous tissue. Figure 2.4 shows the breast lying between two layers: the superficial fascia and the deep fascia covering the pectoralis major muscle. Cooper's ligaments extend between these two layers, connecting the breast to the chest wall. The deep retromammary space is also located between these layers. These ligaments shape the breast and can lead to clinical findings such as skin retraction or an "orange peel" appearance in pathological processes (e.g., tumor invasion) (Briot et al., 2022).

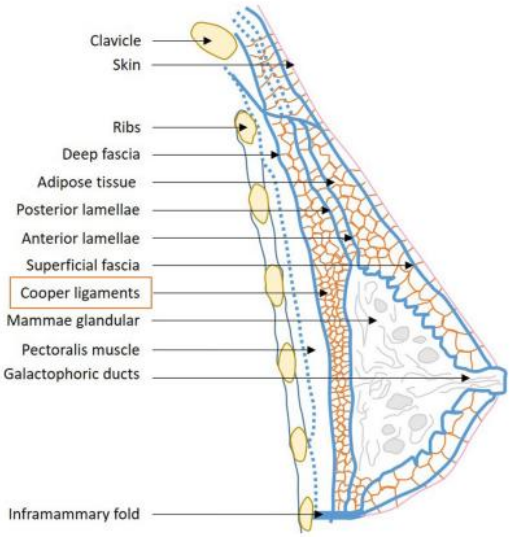

Figure 2.4. Human Female Beast Internal Structure (Briot et al., 2022).

The breast's blood supply is provided by the internal thoracic artery, the lateral thoracic artery, and the posterior intercostal arteries. Venous drainage occurs via venous systems parallel to these arteriesLymphatic fluid drains primarily into the

axillary lymph nodes as well as the internal thoracic (parasternal) lymph nodes. This distribution of the lymphatic system is critical for understanding the metastatic pattern of breast cancer (Fenech et al., 2025).

The nipple and areola region is supplied with small sebaceous glands, Montgomery glands, sensory nerve endings, and muscle fibers located in the pigmented skin of the areola. Sensory innervation of the areola and nipple is provided predominantly by the fourth intercostal nerve (Zucca-Matthes et al., 2016).

Embryologically, breast tissue begins to develop along the milk line in the sixth week, with thickening of ectodermal cells. This line extends from the axilla to the groin, and during normal development, only the thoracic region develops into a breast. Developmental remnants may result in the formation of accessory breasts or supernumerary breasts in the axillary tissue (Lee et al., 2021).

The upper outer quadrant, due to embryological development, has a denser glandular structure and is the region where breast cancer is most frequently observed. This is important for both anatomical and pathological evaluations (Lee et al., 2021).

2.5.2. Clinical Features of Breast Cancer

Breast cancer is the most common malignant tumor affecting women worldwide and constitutes a leading cause of cancer-related death. In 2020, approximately 2.3 million women were diagnosed with breast cancer globally. While breast cancer is quite rare in men, a slight increase in its incidence has been observed in recent years (Sung et al., 2021).

The disease has a heterogeneous structure, both clinically and molecularly. Divided into subtypes such as luminal A, luminal B, HER2-positive, and triple-negative, breast cancer also varies in terms of the type and severity of symptoms (Orrantia-Borunda et al., 2022). While the disease is often asymptomatic in the early stages, it can present with both local and systemic symptoms in later stages. These symptoms may include a mass, nipple changes, skin retraction or edema, axillary lymphadenopathy, and evidence of distant metastasis (Barlow et al., 2002; Orrantia-Borunda et al., 2022). A summary is shown in Table 2.6.

Recognizing clinical symptoms is critical for early diagnosis and effective treatment. While survival rates for breast cancer diagnosed at an early stage exceed 90%, this rate drops significantly in advanced stages. Therefore, healthcare professionals' sensitivity to clinical symptoms is essential in combating the disease (Libson & Lippman, 2014).

Table 2.6. Symptoms of breast cancer (Barlow et al., 2002).

Symptom	Definition and Clinical Features	Status of occurrence	Clinical Significance
Palpable breast mass	Painless, hard, irregularly defined mass	Most frequently	The most critical symptom for early diagnosis
Skin changes	Orange peel, edema, retraction, ulceration	Medium-high	Indicator of local invasion and inflammatory type
Nipple retraction/discharge	Inhalation, ulceration, sero-sanguinous discharge	Moderate prevalence	Suggests centrally located tumors
Lymphadenopathy	Axillary/supraclavicular hard and painless lymph nodes	Widespread	Indicator of lymphatic spread
Localized pain/tenderness	Pain, warmth and redness, especially in inflammatory types	Less often	Indicator of advanced stage or aggressive type
Systemic and metastatic findings	Weight loss, bone pain, dyspnea, neurological symptoms	Late stage	Indicates the presence of metastatic spread

The most common clinical symptom of breast cancer is a painless, firm, irregularly circumscribed mass, usually noticed by the woman or her physician. The most common location is the upper outer quadrant, where breast tissue is most dense. The mass is usually unilateral and may be mobile or fixed. The mass's size, location, and palpable characteristics provide important clues about the stage of the disease (Barlow et al., 2002).

Changes seen on the breast skin often develop due to lymphatic obstruction and may indicate advanced-stage disease. The most common findings include an orange peel appearance, skin redness, edema, ulceration, and hyperemia. These findings are particularly prominent in inflammatory breast cancer and are considered indicators of an aggressive course. Skin retraction occurs when the underlying tumor tissue fuses with the skin and pulls it inward and generally suggests advanced local invasion (Libson & Lippman, 2014).

Nipple retraction (indrawing), erosion, ulceration, or nipple discharge are other notable findings of breast cancer. The type of discharge is an important diagnostic indicator: unilateral, spontaneous, and serosaguinous discharge should be interpreted as a sign of malignancy. Furthermore, eczema-like lesions on the nipple may suggest Paget's disease; This condition is a special form associated with ductal carcinoma and requires diagnostic attention (Orrantia-Borunda et al., 2022).

Breast cancer tends to metastasize through the lymphatic system. The axillary lymph nodes are the most commonly affected sites. These nodes are usually firm, painless, and palpable with reduced mobility. In more advanced stages, supraclavicular or cervical lymph nodes may also be affected. The presence of lymphadenopathy is important in determining the regional spread of the disease and its prognostic status (Fenech et al., 2025).

Although breast cancer is generally a painless disease, localized pain and tenderness can be observed in some subtypes—especially inflammatory breast cancer. Pain is usually felt in areas adjacent to the mass and is often accompanied by inflammatory findings such as increased warmth and erythema. Furthermore, in advanced stages, neuralgic pain due to nerve invasion may also be observed (Orrantia-Borunda et al., 2022).

Systemic symptoms may develop in advanced breast cancer cases. These symptoms encompass fatigue, decreased appetite, weight loss, night sweats, and fever. Organ-specific symptoms related to metastatic spread also occur. For example, bone pain and fractures due to osteolytic lesions may occur in bone metastases; hepatomegaly and jaundice may occur in liver metastases; and dyspnea and persistent

cough may occur in lung metastases. Brain metastases may present with neurological findings such as headache, confusion, and seizures (Fenech et al., 2025).

2.5.3. Methods for Early Breast Cancer Detection

Diagnosing breast cancer at an early stage is critical for reducing mortality and morbidity. Early diagnosis allows for localized tumor detection, which increases the likelihood of a complete cure with less invasive treatments. Diagnostic modalities are utilized both for screening asymptomatic populations and for the clinical evaluation of symptomatic patients. In this regard, several methods are widely utilized, including mammography, ultrasonography, magnetic resonance imaging (MRI), clinical breast examination, and breast self-examination (L. Wang, 2017).

- **Clinical and Physical Examination Methods**

These methods constitute the first non-imaging evaluation steps in the early diagnosis of breast cancer. These methods are considered important screening tools, especially in resource-limited areas, and contribute to raising awareness.

Breast Self-Examination (BSE) allows individuals to identify abnormalities through regular self-examination. Nonetheless, evidence from randomized controlled trials indicates that breast self-examination (BSE) does not lead to a significant decrease in breast cancer mortality. While this method is important for raising awareness and monitoring personal health, it can lead to unnecessary medical visits due to false-positive alerts. It is easy to implement and increases individual awareness. It has low scientific validity and can cause false-positive results and unnecessary anxiety (L. Wang, 2017).

Clinical breast examination is the physical detection of lumps, nodules, or other abnormalities in the breast tissue by systematic palpation performed by healthcare professionals. CBE, when combined with mammography, contributes to the diagnosis of early-stage cancers, but its use alone has low sensitivity and there is evidence that it does not significantly reduce mortality (Nelson et al., 2016). Standardization challenges arise due to operator dependency and interindividual variability. Low cost; availability; early detection; low sensitivity and specificity; risk of missing early lesions; and dependence on training and experience (L. Wang, 2017).

- **Imaging-Based Methods**

Imaging-based methods are essential diagnostic tools for the early detection of breast cancer, and screening with mammography, particularly in women aged 50–69, can reduce mortality by 25–40%. These methods play a critical role in identifying asymptomatic cases due to their high sensitivity and diagnostic accuracy (K. A. Smith et al., 2023).

Mammography is considered the gold standard for early-stage breast cancer detection. It is used in routine screening programs, particularly in women aged 50–74, and is widely credited with reducing breast cancer mortality by 25–40% in this age group (Nelson et al., 2016). Mammography uses X-rays to visualize masses, microcalcifications, and other pathological changes in breast tissue. However, the sensitivity of mammography decreases in women with high breast density because dense fibroglandular tissue makes it difficult to visualize masses. Therefore, adding digital tomosynthesis to mammographic imaging enables layer-by-layer scanning of breast tissue and allows for three-dimensional separation of lesions. This reduces false-negative and positive rates, particularly in individuals with dense breast tissue (Alabousi et al., 2020). The clinical utility of digital tomosynthesis is validated by evidence-based studies and integrated into standard mammography protocols. Widely available, high-level evidence suggests mortality reduction, and low invasiveness. Use of ionizing radiation, low sensitivity in dense breast, different efficacy depending on age group, risk of overdiagnosis.

Contrast-enhanced spectral mammography is an advanced imaging method that uses iodinated contrast material to assess the vascular structure and angiogenesis of breast tissue. CESM provides higher sensitivity and better lesion detection than standard mammography, especially in patients with dense breast tissue (AJR CESM study, 2017). This method reveals vascular enhancement even in the early stages of breast cancer, making lesions more visible. However, the use of iodinated contrast should be used with caution due to the risk of allergic reactions and renal dysfunction. This high sensitivity, improved vascular assessment, and improved lesion detection compared to standard mammography are associated with the need for contrast, increased radiation dose, and contrast-related side effects (Nelson et al., 2016).

Magnetic Resonance Imaging (MRI) is a method that provides high-resolution, radiation-free assessment of breast tissue, particularly recommended for high-risk individuals (such as those carrying BRCA mutations). MRI has a sensitivity of approximately 90% and is very effective in detecting early-stage disease such as multifocal, multicentric, and ductal carcinoma in situ (DCIS). However, its specificity is lower than that of mammography and ultrasound, leading to an increase in false-positive results. Furthermore, due to its cost and time-consuming nature, MRI is used in selected high-risk patients rather than in routine screening. Radiation-free; high sensitivity; detection of early-stage and multifocal lesions; high cost; limited availability; low specificity; and risks associated with the contrast agent (Elahi & Nazari, 2024).

- **Molecular and Biologically Based Methods**

Molecular and biologically based techniques provide a non-invasive and highly sensitive means for the early detection of breast cancer by targeting tumor-specific genetic alterations and biomarkers. Notably, biomarkers such as circulating tumor DNA (ctDNA) can be identified in 62–74% of patients with early-stage breast cancer and hold significant prognostic value for disease monitoring. (Wu & Chu, 2022).

Liquid biopsy is a non-invasive diagnostic and monitoring method that detects tumor DNA (ctDNA) or tumor cells (CTCs) released into the blood by the tumor. Although ctDNA levels are generally low in early-stage breast cancer, some studies have shown high specificity and sensitivity even at an early stage (Zhang et al., 2019; Wan et al., 2020). It also plays a crucial role in assessing prognosis in advanced stages of the disease. (Breast Cancer Research, 2025). The detection of CTCs is a valuable biomarker for assessing treatment response, especially in metastatic patients (STIC CTC study). However, limited detection rates in early stages and technological costs preclude the use of these methods in routine screening. Non-invasive; reflects tumor heterogeneity; monitors treatment response. Low detection rate in early stages; high cost; technical difficulties; does not provide tumor localization (van der Poort et al., 2022).

The PIC-Seq method aims to determine the molecular profile of tumors for early diagnosis based on cfDNA fragment analysis. While still in the research phase for early-stage breast cancer, promising results have been reported. Furthermore, ctDNA detection in breast milk is being evaluated as a new and potential method for early diagnosis, particularly in the postpartum period (VHIO study). Early molecular subtyping is non-invasive. Clinical use is still in its early stages; standardization and large-scale validation are lacking (L. Wang, 2017).

2.5.4. Breast Cancer Staging: Anatomy and Prognostics

Breast cancer is one of the most common malignant neoplasms affecting women worldwide, with staging serving a pivotal function in both diagnosis and treatment. The process of staging, which assesses the anatomical extent of the disease, is essential for prognosis prediction, selection of therapeutic strategies, and guiding clinical decisions. The TNM (Tumor, Node, Metastasis) classification system, developed by the American Joint Committee on Cancer (AJCC) and the Union for International Cancer Control (UICC), has been widely accepted as the standard model for cancer staging. This system stages breast cancer anatomically based on primary tumor size (T), regional lymph node involvement (N), and the presence of distant metastases (M) (Hu et al., 2017).

However, this system, based solely on anatomical criteria, has been observed to lead to significant differences in clinical course and treatment response among patients with the same TNM stage. Therefore, with the 8th edition of the AJCC, which entered into force in 2018, a prognostic staging system that incorporates the biological characteristics of the tumor in addition to the classical TNM staging was implemented (Sun et al., 2020). In this new system, tumor histological grade, estrogen (ER) and progesterone (PR) receptor status, HER2 (human epidermal growth factor receptor 2) status, and, in some cases, gene expression panels (e.g., Oncotype DX, MammaPrint, EndoPredict) have become decisive factors in staging. This allows for the classification of patients into more accurate prognostic groups, considering not only tumor size and metastatic spread but also their potential biological behavior (Prat et al., 2012).

The staging approach created by integrating these biomarkers reveals that patients with similar anatomic stages may have different prognoses and allows for personalized treatment. For example, a patient with T1N0 disease who is hormone receptor positive, HER2 negative, and has a low proliferation index (like luminal A) can be classified into different stages based on their biological characteristics and be directed to different treatment strategies, compared to a patient with the same anatomic stage but a triple-negative subtype (triple-negative) (Prat et al., 2012).

Staging systems are used not only at diagnosis but also in the evaluation of residual disease after treatment. In this context, a distinction is made between clinical staging (cTNM), pathological staging (pTNM), and post-neoadjuvant therapy staging (ypTNM), each of which can address different clinical questions. Furthermore, the harmonious use of these staging systems is recommended, particularly in advanced-stage patients, for assessing treatment response and predicting survival (AJCC Cancer Staging Manual, 8th Ed., 2018).

Today, staging has become a multidimensional tool that predicts not only the extent of cancer spread but also the biological behavior of the tumor, its response to treatment, and long-term survival. Therefore, the combined use of anatomical and prognostic staging systems represents a current and effective approach to breast cancer management (AJCC Cancer Staging Manual, 8th Ed., 2018).

2.5.4.1. Anatomical TNM Staging

The anatomic TNM staging system (Table 2.7) is a globally accepted classification method that categorizes cancer based on the primary tumor's size and extent of invasion (T), involvement of regional lymph nodes (N), and the presence of distant metastases (M). This classification is critical for both diagnosis and treatment planning (Lian et al., 2021).

Table 2.7. T, N, and M Categories: Definitions and Subgroups (Sun et al., 2020).

Category	Definition and Subgroups
T (Tumor)	Tis (in situ), T1 (≤2cm subcategories), T2 (>2 ≤5cm), T3 (>5cm), T4 (skin/chest wall invasion and subgroups: T4a-d)
N (Lymph nodes)	N0 (absent), N1 (mobile ipsilateral axillary I-II), N2 (fixed/matted axillary or IM), N3 (infraclavicular, supraclavicular, IM + axillary)
M (Metastasis)	M0 (absent), M1 (distant metastasis)

The T-Category defines the primary tumor size and local soft tissue/skin/chest wall invasion: it ranges from Tis (in situ) to T4d (inflammatory breast cancer) subtypes. For example, T1c tumors are between 10–20 mm and do not contain invasion; in the T4 classification, the tumor is subclassified based on chest wall or skin invasion (Sun et al., 2020).

The N-Category indicates whether metastases are present in the axillary, supraclavicular, or internal mammary nodes. N0 indicates no nodal involvement, N1 indicates mobile axillary nodal involvement, and N3 indicates fixed nodes with supraclavicular and/or internal mammary metastases. The M-Category defines the presence of distant metastases: M0 indicates no metastasis, while M1 indicates the presence of distant metastases, either clinically or histologically. TNM classifies combinations from stage 0 to stage IV; for example, Stage I: T1N0M0; Stage III: T3 and/or N2 or T4N0–2M0; Stage IV: any T, any N, or M1 (Wikipedia TNM system, 2024). It is important to note that the staging model uses only anatomical criteria and does not include biological markers (ER, PR, HER2, grade) (Lian et al., 2021).

Prognosis statistics by stage are as follows: 5-year survival for patients with Stage 0 and I is ~100%, Stage II is ~90%, Stage III is ~70%, and Stage IV is ~30% (SEER; VerywellHealth, 2023; Cancer Research UK, 2025). While these rates may vary across geographic regions and treatment periods, they provide a general clinical perspective (Laohavinij et al., 2013). A summary is shown in Table 2.8.

Table 2.8. Breast Cancer TNM Stages and Survival Rates (Laohavinij et al., 2013).

Stage	TNM Definition (Examples)	Approximate 5-Year Survival Rate
Stage 0	Tis, N0, M0 (in situ lesions)	~%100
Stage I	T1, N0, M0 (≤2cm, no nodal metastasis and distant metastasis)	~%100
Stage II	T0–T2, N1, M0 or T2–T3, N0, M0	~%90
Stage III	T3–T4, N1–N3, M0 (locally advanced disease)	~%70
Stage IV	Her T, Her N, M1 (there is distant organ metastasis)	~%30

Clinical staging (cTNM) is based on the patient's physical examination findings at the time of diagnosis, imaging studies (mammography, ultrasonography, MRI), and biopsy results. In this staging, the cT, cN, and cM categories, denoted by the prefix "c" (clinical), are the first tools for assessing anatomic spread. For example, mobile, fixed, or internal mammary node involvement of the axillary and supraclavicular lymph nodes is classified as cN1–cN3 (AJR, 2020). Clinical staging is critical for prognostic assessment and treatment strategy during the initial stage when surgical and neoadjuvant treatment decisions are made (AJCC 8th edition, 2018).

Pathological staging (pTNM) is determined by histopathological examination of tissue samples obtained after surgery; the "p" prefix reflects pathologically confirmed tumor size (pT), nodal involvement (pN), and metastatic status (pM). Compared to cTNM, it provides a more precise definition of anatomic stage, making pathology the gold standard for prognostic assessment. Additionally, additional parameters such as residual tumor burden, number of nodal metastases, and histological grade increase the accuracy of this staging (Lian et al., 2021).

In patients undergoing neoadjuvant (pre-treatment) systemic therapy, restaging is performed based on pathological data obtained through surgery after treatment (ypTNM); the prefix "yp" ("y" = after therapy) is used in this category. Residual tumor size (ypT), nodal involvement (ypN), and metastatic status (ypM) are evaluated, and the patient is reclassified according to their response to treatment. Nodal status is

particularly prognostic after nAC, and the presence of residual nodal metastases (ypN+) significantly negatively impacts survival (5-year OS: ~83.3% vs. ypN0: ~91%). Furthermore, patients with pCR (pathologic complete response, ypT0/is ypN0) at this stage have a similar high prognosis to cases with noninvasive residual DCIS, with restaging to TNM categories. Post-neoadjuvant staging resulted in downstaging in approximately 24% (45/185) of patients (Bachawal et al., 2013).

2.5.4.2. Prognostic Staging: AJCC 8th Edition Innovation

The 8th edition of the AJCC (published in 2018) significantly evolved breast cancer staging by integrating not only anatomic TNM criteria but also biomarkers (e.g., tumor grade, hormone receptor status ER/PR, HER2 expression) and, in some clinical settings, multigene expression panels (e.g., OncotypeDX. This new approach allows for the recognition of important prognostic differences among patients with similar anatomic stages and adds greater accuracy to treatment planning and survival prediction (I. Kim et al., 2018).

Histologic grade is a measure of how well differentiated a tumor is and is classified in the R0–R3 format using the Nottingham-modified Scarff–Bloom–Richardson system. Grade is a strong prognostic factor that determines survival independently of, and not only with, TNM parameters (Lian et al., 2021)..

ER and PR-positive tumors generally respond well to hormonal therapies; while HER2-positive tumors, despite their more aggressive course, have significantly improved prognoses with anti-HER2 therapies. The 8th edition of the AJCC mandated the assessment of these biomarkers for all invasive breast cancers (PMC abstract, 2018^4; Kosaka et al., 2017^3) (Mittendorf et al., 2018).

Incorporating the Oncotype DX score into prognostic staging is recommended in certain clinical scenarios, particularly for T1-T2N0, ER-positive, and HER2-negative patients. For example, early-stage patients defined as having an RS < 11 can be classified as pathological prognostic stage I-A, regardless of anatomic stage. This information makes chemotherapy decisions more objective (Mittendorf et al., 2018).

Studies show that prognostic staging leads to upstaging or downstaging in approximately 30% of patients (Sopin et al., 2019^2). Prognostic stage grouping demonstrates higher prognostic sensitivity than traditional anatomic staging (C-index ≈0.84 vs. 0.74; lower AIC), making it a more powerful tool for clinical decision support systems (Kim et al., 2018^1; Sopin et al., 2019^2).

This system plays a crucial role in treatment decisions, particularly for patients with ER+/HER2− subtypes. For example, while most patients with Oncotype <11 are successfully managed with hormonal therapy, treatment strategies, such as chemotherapy recommendations, are more clearly defined in patients with a high RR (data such as those from the TAILORx study^2). Additionally, prognostic staging in triple-negative or high-grade tumors may predict that a more aggressive approach will be required (I. Kim et al., 2018).

2.5.4.3. Classification of Histological Subtypes

The histological classification of breast cancer is based on guidelines published by the WHO and systematically defines both in situ and invasive tumor subtypes; this classification plays a fundamental role in diagnostic accuracy, prognostic assessment, and treatment decisions. With the updates included in the 5th WHO edition, in addition to the classic ductal and lobular types, metaplastic, apocrine, medullary, micropapillary, mucinous, tubular, cribriform, papillary, and other rare types are further defined under separate categories. Each of these subtypes has distinct clinical courses and survival outcomes, based on their microscopic margins, cellular characteristics, and immunophenotypes (Cserni, 2020).

Ductal carcinoma in situ (DCIS) is defined by its subtypes, including micropapillary, comedo, cribriform, and papillary. The risk of recurrence varies depending on the grade; the rate of progression to invasive disease is significantly higher after high-grade DCIS. Lobular carcinoma in situ (LCIS) is characterized by both pleomorphic and classic subtypes; pleomorphic LCIS is a more aggressive form with a risk of invasive development (Cserni, 2020).

The most common subtype, invasive ductal carcinoma no special type (IDC-NST), accounts for approximately 75–80% of invasive breast cancers and comprises a

highly biologically heterogeneous group (Li, 2010). Invasive lobular carcinoma (ILC), the second most common subtype, is characterized by E-cadherin loss, single-row infiltration, and a segmental targetoid structure and includes lower-grade, ER/PR-positive cases with a good prognosis. The five-year survival rate for ILC has been reported to be approximately 85%.

Tubular, cribriform, and mucinous (colloid) carcinomas are generally ER/PR positive, low-proliferating, and Grade 1, with a very good medical prognosis (Cserni, 2020). Micropapillary carcinoma, however, is an aggressive subtype with a high rate of lymphatic invasion and generally exhibits a luminal B phenotype (Kim Koreya study, 2020). Medullary carcinoma is less common and may have a triple-negative immunophenotype, but due to intense lymphocytic infiltration and good chemotherapy response, it exhibits better survival rates, with an absolute mortality risk of up to 50% reduced compared to IDC (Li, 2010). Metaplastic carcinoma is very rare and triple-negative, and tumors with spindle cell or matrix-producing subforms are reported to be associated with a high grade and poor prognosis (Cserni, 2020).

Apocrine carcinoma is a rare but potential therapeutic target subtype that is ER/PR negative, AR positive, and sometimes HER2 positive (Wikipedia-apocrine, 2024). Neuroendocrine carcinoma, defined by synaptophysin and chromogranin A positivity, is rare but warrants clinical attention for specific treatment approaches. The 5th WHO edition defined these rare types in separate categories and recommended stratification based on the clinical characteristics of each (Cserni, 2020).

Retrospective analyses using SEER data have shown that mucinous, tubular, and medullary carcinomas carry a 31–79% lower mortality risk compared to IDC-NST. In contrast, inflammatory breast cancer is among the most prognostically unfavorable types, with a 50–53% increased mortality risk depending on age (Li, 2010). Kim et al.'s study in a Korean database found that specific histologic types had similar overall survival rates to benign NST, but the medullary type had a better prognosis, while the metaplastic type had a worse prognosis (Kim et al., 2020).

Correlating histological classifications with molecular subtypes is also important for prognostic assessment. For example, tubular, cribriform, and mucinous

types overlap with the luminal A-like immunophenotype, while medullary and metaplastic types generally fall into the basal-like/triple-negative classification (Kim et al., 2020). Such overlapping patterns directly impact clinical practice in terms of effective classification and targeted approaches in treatment planning.

2.5.5. Breast Cancer Treatment Methods

Breast cancer is one of the most commonly diagnosed malignant tumors in women globally and ranks among the primary causes of illness and death. The biological and clinical heterogeneity of the disease necessitates the implementation of multidisciplinary and individualized approaches in the treatment. Treatment modalities primarily consist of surgery, radiotherapy, and systemic treatments, and the combination of these methods is determined by the disease stage, molecular subtype, and patient-specific factors (Waks & Winer, 2019).

Today, the identification of molecular markers, particularly estrogen and progesterone receptors and HER2 status, plays a decisive role in treatment planning (Smith et al., 2014). While hormonal therapies constitute the primary systemic treatment method for hormone receptor-positive tumors, targeted agents have yielded significant improvements in survival in HER2-positive patients (Han & Wei, 2025). Additionally, treatment algorithms for triple-negative breast cancer are expanding with the addition of new agents such as immunotherapy or PARP inhibitors to chemotherapy (Barchiesi et al., 2021).

This study details breast cancer treatment approaches under the headings of surgery, radiotherapy, and systemic therapy, and aims to comprehensively evaluate the efficacy, indications, and limitations of each method in light of clinical evidence and current guidelines. Figure 2.11 shows the scheme of the topics to be examined (Leclerc et al., 2016).

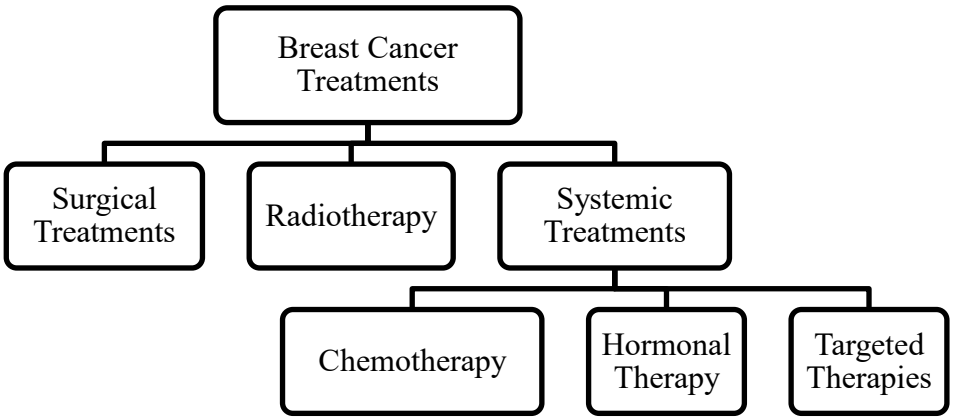

Figure 2.5. Schematic Image of Breast Cancer Treatment Methods

2.5.5.1. Surgical Treatments

Breast cancer is the most frequently diagnosed malignancy among women worldwide and constitutes a significant public health challenge owing to its elevated morbidity and mortality rates. With evolving diagnostic methods, early-stage detection rates have increased, leading to more preventative, functional, and patient-centered surgical treatment approaches. Surgical intervention is the most fundamental treatment step in achieving local tumor control, and the type of surgical method chosen is directly related to the tumor's stage, location, biological characteristics, and individual patient preferences (Sung et al., 2021).

Today, surgical approaches have evolved from radical methods such as modified radical mastectomy to more conservative options such as nipple-sparing mastectomy and breast-conserving surgery. These methods are supported by systematic reviews and multicenter randomized controlled trials in terms of both oncological safety and aesthetic outcomes. In addition, axillary surgery is performed with less invasive techniques such as sentinel lymph node biopsy instead of classical dissection; this reduces postoperative complications and improves the quality of life of patients (Si et al., 2025).

Table 2.9. Overview of Surgical Options in Breast Cancer Treatment.

Surgical Method	Indication	Oncological Safety	Aesthetics / Morbidity
Lumpectomy + Radiotherapy	Early stage, well-differentiated tumors	OS ≈ mastectomy, low local recurrence	Aesthetic goodness, low morbidity
SSLNB	Node-negative patients	OS and EFS are similar, lymphedema risk is low	Morbidity decreases
NSM	Selected early-stage cases	Local recurrence ≈5%, OS ~96%	Aesthetic satisfaction is high, complications are ~22%

Breast Conserving Surgery (Lumpectomy)

Breast-conserving surgery offers survival comparable to mastectomy in patients with early-stage invasive disease, and local control is effective when supported by radiotherapy (Fisher et al., 2002). Based on 20-year follow-up data from the NSABP B-06 trial, the ipsilateral recurrence rate was 14.3% in the lumpectomy plus radiotherapy group, compared to 39.2% in the lumpectomy-only group, while overall survival rates showed no significant difference between the two groups (Fisher et al., 2002). A 12-year update also found no difference in the core survival data (Fisher et al., 1995).

Sentinel Lymph Node Biopsy (SLNB) and Axillary Dissection

Sentinel lymph node biopsy is preferred over axillary dissection in patients with node-negative early-stage breast cancer and significantly reduces surgical morbidity, particularly the rate of lymphedema. In a randomized trial with 15 years of follow-up, overall survival and e-freelive survival rates in the SLNB-referred patient group were similar to those in the axillary dissection group (OS 82.0% in the SLNB arm; 78.8% in the ALND arm; $p = 0.502$) (Agha et al., 2019).

Comparison of Mastectomy and Its Types

Surgical interventions are among the primary treatment approaches for breast cancer treatment, aiming to achieve local tumor control and improve survival. Breast-conserving surgery remains the preferred treatment for early-stage lesions; however, mastectomy is also indicated, especially in cases of multifocal tumors, a high tumor-to-breast size ratio, or according to patient choice. Mastectomy methods have diversified, considering cosmetic and functional outcomes as well as oncological safety, paving the way for the development of more conservative techniques over time (Agha et al., 2019).

Current mastectomy types include modified radical mastectomy, skin-sparing mastectomy, nipple-sparing mastectomy, and subcutaneous mastectomy, each selected based on specific clinical characteristics (Clarijs et al., 2023). The effectiveness of these surgical techniques has been evaluated in numerous randomized controlled trials and observational studies, and comparisons have been made regarding local recurrence rates, survival data, and complication profiles (Agha et al., 2019).

- **Modified Radical Mastectomy (MRM):** MRM is the standard surgery in which all breast tissue and axillary lymph nodes are removed; it is preferred especially in multicentric or large lesions and provides long-term local control (Holland & Fisher, 2006).
- **Nipple-Sparing Mastectomy (NSM):** Nipple-sparing mastectomy (NSM) is a surgical technique that facilitates reconstruction by preserving the nipple-areola complex and is considered oncologically safe when patients are appropriately selected. According to the results of a study including 1989 patients from Italy, 5-year overall survival in invasive cases was reported as 96.1%, local recurrence rate as 5.3%, and NAC recurrence rate as 1.8% (Galimberti et al., 2018). In a systematic review analysis, the local recurrence rate was 5.4%, NAC recurrence rate as 1.3%, and distant metastasis rate as 4.8% (Zaborowski et al., 2023). A meta-analysis revealed no statistically significant differences between nipple-sparing mastectomy (NSM) and conventional mastectomy regarding overall survival (OS), disease-free survival (DFS), and local recurrence rates (0.4% local recurrence difference;

p>0.05) . The complication rate of NSM is reported as approximately 22.6%; This is largely due to local complications such as nipple necrosis. However, the aesthetic satisfaction rate is higher than with SSM (De La Cruz et al., 2015).

- **Skin-Sparing Mastectomy (SSM):** Skin-sparing mastectomy involves preserving a significant amount of skin tissue during the removal of breast tissue, which can result in more aesthetically pleasing and natural-looking reconstructions. Multicenter meta-analyses have shown no significant difference in local recurrence and survival between SSM and modified radical mastectomy. For example, in a study of 3,700 patients, the local recurrence rate was 6.2% for MRM and 4.0% for SSM, with no statistically significant difference (OR = 1.25; 95% CI 0.81–1.94) (De La Cruz et al., 2015).
- **Protokeratic Mastectomy and Radical Mastectomy:** While historically used, radical mastectomy (Halsted) removes extensive tissue, including the chest muscles, it is no longer preferred today unless the tumor has invaded the chest muscles. With the development of modern surgery, this radical approach has been limited to select patients requiring only chest wall intervention (Magnoni et al., 2021).
- **Subcutaneous (Skin-Sparing) Mastectomy and Reconstruction:** Subcutaneous mastectomy or cosmetic flat mastectomy options can be performed without nipple removal or with minimal tissue preservation. These surgeries meet the aesthetic and psychosocial needs of patients by allowing simultaneous reconstruction with implants or autogenous tissue. Prepectoral implant placement, in particular, has been shown in some studies to be associated with lower postoperative pain and functional morbidity (Magnoni et al., 2021).

2.5.5.2. Radiotherapy

Radiotherapy is widely used as adjuvant therapy after breast-conserving surgery; this strategy significantly reduces the rate of ipsilateral local breast recurrence and improves overall survival. The standard whole-breast irradiation (WBI) treatment plan typically delivers a total dose of 45–50 Gy in fractions lasting 5–7 weeks, maintaining local control and maintaining cosmetic results (Mukesh et al., 2016).

Approximately one-third of patients experience acute skin toxicities (e.g., moist dermatitis, hyperpigmentation) after Whole-Breast Irradiation (WBI); these side effects can lead to a decreased quality of life. Intensity-modulated radiotherapy (IMRT) techniques provide more precise dose distribution to the target volume, reduce normal tissue exposure, and significantly reduce acute toxicity rates (Hickey et al., n.d.).

In selected early-stage patients undergoing lumpectomy, Accelerated Partial Breast Irradiation (APBI) methods have been developed that focus solely on the tumor bed and surrounding area; these approaches significantly reduce treatment time and improve cosmetic outcomes (Hickey et al., 2016).

Intraoperative Radiotherapy (IORT), which can be administered as a single dose during surgery, is particularly effective in low-risk, early-stage cases, and long-term local control rates are comparable to WBI. The TARGIT-A randomized clinical trial demonstrated that single-dose targeted intraoperative radiotherapy (TARGIT-IORT) during lumpectomy in early-stage breast cancer patients provided comparable long-term local control and survival outcomes to conventional whole breast external beam radiation therapy (EBRT). Furthermore, lower mortality from other causes was reported in the TARGIT-IORT group. These findings support the idea that TARGIT-IORT is an effective and safe treatment option with appropriate patient selection (Vaidya et al., 2020). Conversely, the ELIOT study reported a higher risk of recurrence and reported a higher rate of local recurrence in the IORT group (Veronesi et al., 2013).

The combination of fractionated radiotherapy with Volumetric Modulated Arc Therapy (VMAT) and Deep Inspiration Breath Hold (DIBH) significantly reduces cardiac dose, particularly in patients with left-sided breast cancer; in a retrospective study, cardiac dose was reduced from 2.8 Gy to 1.8 Gy (Tamburella et al., 2019). While randomized clinical data on the use of these techniques are still limited, their dosimetric advantages have been clearly demonstrated.

2.5.5.3. Chemotherapy

Breast cancer is one of the most common malignant neoplasms in women and a significant cause of cancer-related deaths worldwide (Waks & Winer, 2019). In the systemic management of this disease, chemotherapy is administered with either curative or palliative objectives, contingent upon the disease stage and the tumor's biological characteristics. Chemotherapeutic agents target rapidly dividing cancer cells, disrupting the cell cycle and inducing apoptosis, thus aiming to reduce tumor burden (Cortazar et al., 2014).

In early-stage breast cancer, chemotherapy administered adjuvantly after surgery eliminates micrometastatic disease and prolongs disease-free survival (Thomssen et al., 2021). Additionally, preoperative neoadjuvant chemotherapy has the potential to decrease tumor size, thereby enhancing the feasibility of breast-conserving surgery (Cortazar et al., 2014). In advanced or metastatic disease, chemotherapy is administered as a palliative approach to slow disease progression and improve quality of life (Waks & Winer, 2019).

Chemotherapy regimens generally include anthracyclines, taxanes, alkylating agents, and antimetabolites. Treatment selection is made based on the tumor's molecular subtype (e.g., hormone receptor status or HER2 expression) and the patient's clinical condition (Anampa et al., 2015). Furthermore, genomic testing and biomarkers allow the identification of patient groups with high sensitivity to chemotherapy, thus minimizing the risk of unnecessary toxicity survival (Thomssen et al., 2021).

Today, chemotherapy in breast cancer has become part of an integrated, individualized treatment strategy that includes hormonotherapy, targeted therapies, and immunotherapy, rather than a stand-alone treatment approach (Waks & Winer, 2019).

Chemotherapy drugs are cytotoxic agents used to inhibit the proliferation of cancer cells or eliminate them through apoptosis. These drugs are classified according to their chemical structures and intracellular targets and used in different treatment strategies. Classification is based on the drugs' effects on the cell cycle and their molecular targets (Tacar et al., 2013).

- **Alkylating Agents:** This group of drugs alkylates DNA, creating cross-links between base pairs and inhibiting replication. They can be effective at any stage of the cell cycle. The most common agents include cyclophosphamide, ifosfamide, and busulfan. These agents induce cell death by causing DNA damage, particularly in rapidly dividing cells (Kondo et al., 2010).
- **Antimetabolites:** Antimetabolites are compounds that are structurally similar to the cell's normal metabolites and act by disrupting nucleic acid synthesis. This group includes pyrimidine (e.g., 5-fluorouracil), purine (e.g., 6-mercaptopurine), and folate antagonists (e.g., methotrexate). They generally act in the S phase (Thomas & Zalcberg, 1998).
- **Natural Products (Plant-Derived Agents):** Plant-derived chemotherapy drugs disrupt mitosis by affecting the cytoskeleton and mitotic spindle fibers. Vinca alkaloids (e.g., vinblastine, vinorelbine) inhibit microtubule polymerization, while taxanes (e.g., paclitaxel, docetaxel) prevent microtubule depolymerization. These agents are generally effective in the M phase (Jordan & Wilson, 2004).
- **Antibiotic-Derived Antineoplastics:** This group is of bacterial origin and acts by intercalating into DNA. Anthracyclines (e.g., doxorubicin, daunorubicin) act as topoisomerase II inhibitors, halting DNA replication and causing cell damage through free radical production (Minotti et al., 2004).
- **Topoisomerase Inhibitors:** Topoisomerase I inhibitors (e.g., topotecan, irinotecan) and topoisomerase II inhibitors (e.g., etoposide) disrupt the supercoiling structure of DNA, interfering with transcription and replication. These inhibitors are not specific to the cell cycle but are more effective in the S and G2 phases (Pommier, 2006).
- **Platinum Compounds:** Agents such as cisplatin, carboplatin, and oxaliplatin inhibit replication by forming covalent bonds between DNA strands. They function similarly to alkylating agents but have a different chemical structure. They are widely used, particularly in the treatment of solid tumors (D. Wang & Lippard, 2005).

These drug groups act at different stages of the cell cycle, allowing for selective targeting of cancer cells (Table 2.10). However, dose adjustments must be made with caution, given that these agents can also affect healthy cells.

Table 2.10. FDA-Approved Breast Cancer Drugs (Chaurasia et al., 2023).

Drug / Combination	FDA Approval	Indication
Fam-trastuzumab deruxtecan-nxki (Enhertu)	December 2019 (HER2 positive); August 2022 (HER2 low/ultra low)	Metastatic or inoperable HER2-positive and HER2-low breast cancer
Trastuzumab emtansine (T-DM1; Kadcyla)	February 2013 (metastatic); May 2019 (adjuvant)	Adjuvant therapy for HER2-positive metastatic and post-neoadjuvant residual disease
Abemaciclib (Verzenio)	October 2021 (adjuvant); March 2023 (expanded approval)	HR positive, HER2 negative early stage high-risk breast cancer
Sacituzumab govitecan-hziy (Trodelvy)	April 2021 (TNBC); February 2023 (HR positive HER2 negative)	Metastatic triple-negative and HR-positive HER2-negative breast cancer
Elacestrant (Orserdu)	January 2023	ESR1-mutated, ER-positive, HER2-negative metastatic breast cancer
Inavolisib Palbociclib Fulvestrant	October 2024	PIK3CA-mutated, HR-positive, HER2-negative advanced breast cancer

Chemotherapy in breast cancer treatment is administered in combination regimens tailored to the stage of the disease, its biological characteristics, and patient-specific risk factors. These regimens can be designed for curative (adjuvant/neoadjuvant) or palliative (metastatic) purposes and are often combined to take advantage of the synergistic effects of different agents.

One of the most commonly used regimens in early-stage breast cancer is the AC (doxorubicin + cyclophosphamide) regimen. This regimen is usually administered

sequentially (AC→T) with a taxane (paclitaxel or docetaxel) and is particularly preferred in node-positive or high-risk patients. The beneficial effects of this approach on disease-free survival (DFS) and overall survival (OS) are well documented (Chen et al., 2021).

The TC regimen (docetaxel + cyclophosphamide) is a safe alternative in patients at risk of cardiotoxicity due to its lack of anthracyclines. However, chemotherapy is often combined with anti-HER2 agents in HER2-positive tumors. In this context, TCH (docetaxel + carboplatin + trastuzumab) and its more potent version, TCHP (with the addition of trastuzumab + pertuzumab), are standard neoadjuvant options for HER2-positive early-stage breast cancer. Classic combinations such as CMF (cyclophosphamide + methotrexate + 5-FU) are still used in select cases for less aggressive tumors or in elderly and frail patients. In addition, anthracycline-based regimens such as CAF (cyclophosphamide + doxorubicin + 5-FU) or FEC (alternation with epirubicin), which are common in European countries, continue to be used as adjuvant or neoadjuvant in selected cases (Cardoso et al., 2019).

In metastatic breast cancer, treatment is generally tailored to the biological subtype of the disease, response to treatment, and the patient's performance status. Among the regimens used for this purpose, the combination of capecitabine and docetaxel (oral and intravenous agents) offers the advantage of reducing hospitalization. The choice of chemotherapy combinations is individualized not only according to tumor biology but also according to the toxicity profile and patient preference, thus aiming for maximum therapeutic effect (Morishita & Leonard, 2008).

2.5.5.4. Hormone Therapy

A significant subgroup of breast cancer is comprised of estrogen and/or progesterone receptor-positive (HR+) tumors. Because the growth of these tumors depends on the effects of steroid hormones, hormone therapy (endocrine therapy) is one of the primary treatment strategies for these patients. The primary goal of hormone therapy is to block hormone receptors on tumor cells or suppress endogenous hormone production, thereby inhibiting tumor proliferation (Johnston & Dowsett, 2003).

Hormone therapy is planned differently depending on menopausal status. The standard treatment protocol for premenopausal women generally includes selective estrogen receptor modulators (SERMs) such as tamoxifen, while aromatase inhibitors— including letrozole, anastrozole, and exemestane—are preferred for postmenopausal patients. Aromatase inhibitors reduce systemic estrogen levels by inhibiting estrogen synthesis from adrenal androstenedione (Early Breast Cancer Trialists' Collaborative Group (Early Breast Cancer Trialists' Collaborative Group (EBCTCG), 2015).

Tamoxifen acts by competitively blocking the effects of estrogen and has proven particularly effective in premenopausal patients. Tamoxifen use for up to five years significantly reduces the risk of recurrence and death. This treatment can be combined with ovarian function suppression; this combination has been shown to be more effective in high-risk young patients (Francis et al., 2018).

In postmenopausal patients, aromatase inhibitors are more effective than tamoxifen. Five years of aromatase inhibitor treatment reduces both local recurrence and distant metastasis rates and improves long-term survival (Bekes & Huober, 2023). Furthermore, some studies have shown sequential treatment regimens, starting with tamoxifen and then switching to an aromatase inhibitor, to be an effective alternative (Dowsett et al., 2010).

Hormone therapy is also the primary systemic approach in metastatic hormone receptor-positive (HR+) patients. In recent years, hormone therapy combined with CDK4/6 inhibitors (palbociclib, ribociclib, abemaciclib) has significantly prolonged progression-free survival (Finn et al., 2016). This combination is considered a major advance, particularly in preventing endocrine resistance.

In conclusion, hormone therapy is an essential treatment modality for both early-stage and metastatic disease in HR+ breast cancer. Creating individualized treatment plans that consider menopausal status, disease risk, and treatment tolerability is crucial for maximizing clinical benefit.

CHAPTER III. MATERIALS AND METHODS

This theoretical investigation aimed to thoroughly analyze the receptors implicated in breast cancer pathogenesis, placing special emphasis on the human epidermal growth factor receptor 2 (HER2) within the framework of ligand binding. In this context, a comprehensive modeling process was conducted using high-computational capacity computer simulations. The primary focus of the study was the structural analysis of HER2 receptors and their interactions. Detailed structural analyses of the receptors were performed using the 5MY6 (D'Huyvetter et al., 2017), 7PCD (Wilding et al., 2022), and 8U8X (Hicken et al., 2024) gene sequences obtained from the Protein Data Bank (PDB).

The study investigated four important biomolecules that interact with HER2: docosahexaenoic acid (DHA) and eicosapentaenoic acid (EPA). Various computational chemistry and bioinformatics techniques were used to analyze the effects of these components, derived from krill oil, at the molecular level. The binding sites and affinities of DHA and EPA for the HER2 receptor were predicted using Molecular Dynamics Simulation (MDS). Simulations were performed to assess the dynamic behavior of ligand-receptor interactions, and the stability of these interactions was monitored.

Literature searches indicate that anticancer peptides and components such as DHA and EPA in krill oil have growth-suppressing effects on cancer cells (Jayathilake et al., 2016). In this context, the molecular formulas and structural properties of DHA and EPA were obtained from the PubChem database. In computational analyses, the biological activity and IC50 values of DHA and EPA against HER2 receptors were evaluated using the PubChem and ChEMBL databases. These assessments provide critical information for understanding the binding affinities of ligands to their target receptors and their effects on cancer.

Furthermore, biochemical and biological data related to ligands and receptors were obtained from the UniProtKB database. This database provides comprehensive information on the functions, structural motifs, and biochemical properties of proteins associated with HER2 receptors. During the research process, the structures coded

7PCD, 5MY6, and 8U8X in the RCSB PDB database were compared with literature reviews on breast cancer, and previous experimental studies were considered.

In this study, potential ligands with low IC50 values were identified through literature searches in clinical databases and ChEMBL. To more accurately simulate ligand-receptor interactions, extensive modeling was performed in the presence of environmental factors such as water molecules and ions. For each receptor, 54 drugs were selected and docking was performed, and the binding energies of the ligands were calculated in kcal/mol. Based on the obtained data, the ligands with the lowest binding energies were identified and subjected to further analysis.

To evaluate receptor-ligand interactions at the molecular level, both the receptor and the ligand were optimized using AutoDock Vina software. This optimization is highly effective in evaluating potential inhibitors by calculating binding positions, orientations, and predicted binding energies. Its high-speed and precise algorithm makes it a preferred choice in drug discovery (Trott & Olson, 2010). The simulations were supplemented with Molecular Dynamics Simulations (MDS) performed with GROMACS software, specifically to investigate the dynamic behavior of protein-ligand complexes. These simulations were used to understand the motion of ligands on proteins and the structural stability they achieve over time (Hollingsworth & Dror, 2018).

The high computing power required for the simulations was provided by the National Center for High-Performance Computing (UHeM). This center's high-performance computing infrastructure enabled the simulations to be run efficiently.

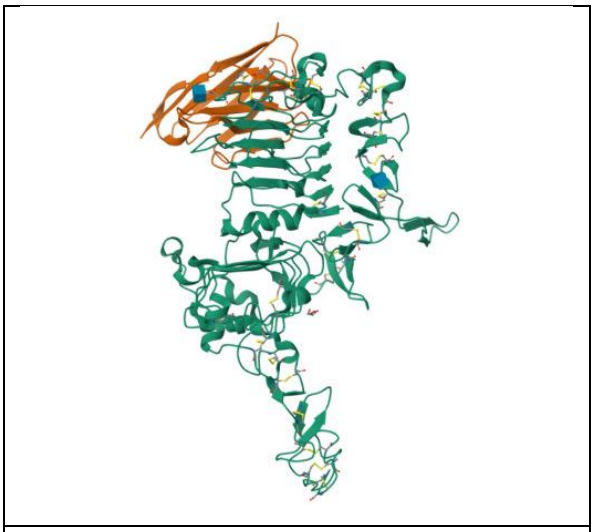

5MY6

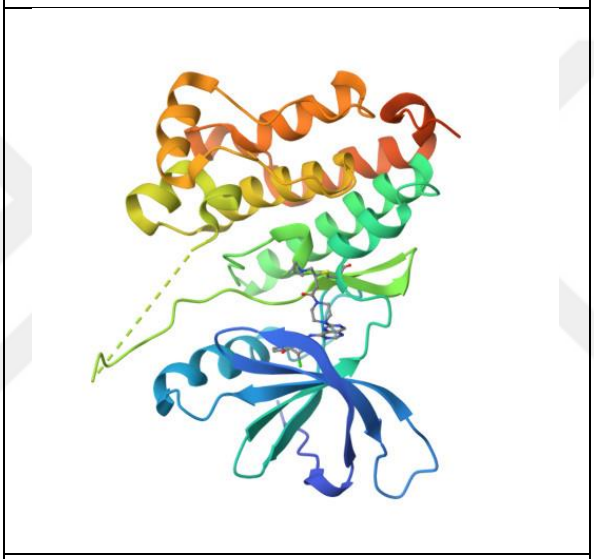

7PCD

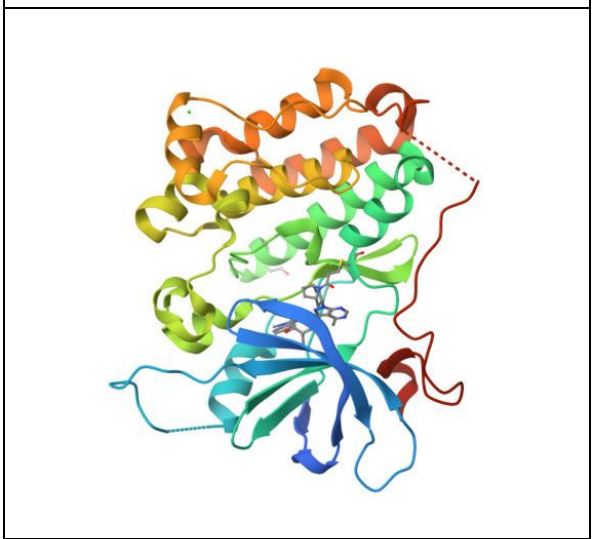

8U8X

Figure 3.1. 3D image of 5MY6, 7PCD and 8U8X receptors obtained from Protein Data Bank.

Following MDS, various analyses were performed to further investigate the dynamic behavior of the system and the stability of ligand-receptor interactions. These analyses included metrics such as RMSD (Root Mean Square Deviation), RMSF (Root Mean Square Fluctuation), Hydrogen Bond Analysis, and Radius of Gyration (Rg). These analyses reveal the electron distributions and reactivity potentials of ligands at the interaction sites on the protein (Calais, 1993). Thus, how ligands interact with receptors at the molecular level, in terms of binding energies and electronic properties at the interaction sites, was comprehensively elucidated (Lemkul, 2024).

3.1 Code Selection

In this study, two natural compounds were selected as ligands for use in molecular docking analyses. Eicosapentaenoic acid (EPA) and docosahexaenoic acid (DHA) are derived from krill oil, a marine phospholipid source. The biological effects of these compounds are well documented in the literature, and the aim was to investigate their potential interactions with target proteins due to their anti-inflammatory and antioxidant properties. Chembl and PubChem databases were used to obtain the applied structures of the selected structures (Table 2.11).

Table 3.1. Receptor-ligand and drug codes.

RECEPTOR	DRUG	LIGAND
5MY6	Lapatinib (CID: 208908)	DHA (CID: 15608515)
		EPA (CID: 446284)
7PCD		DHA (CID: 15608515)
		EPA (CID: 446284)
8U8X		DHA (CID: 15608515)
		EPA (CID: 446284)

3.2 Protein Preparation

Crystal structures of 5MY6, 7PCD, and 8U8X, target proteins associated with breast cancer, were obtained from the RCSB Protein Data Bank (PDB) and preprocessed using AutoDock Tools prior to molecular docking. This process involved removing water molecules from the crystal structure, incorporating missing hydrogen atoms, and optimizing the binding site to make each protein structure suitable for

analysis. These structures were then stored in separate folders in a suitable format to facilitate the study of target protein-ligand interactions and to form the basis for subsequent molecular dynamics simulations.

3.3. Ligand Preparation

The 3D molecular structures of EPA and DHA were downloaded from the PubChem database in standard .sdf or .mol2 formats. These structures were optimized using Open Babel and AutoDock Tools (ADT) to address potential structural deficiencies (hydrogen addition, bond correction, energy minimization, etc.) before being converted to a format supported by AutoDock software.

After determining the number of rotatable bonds for each ligand and defining the necessary flexibility, the ligand structures were saved in .pdbqt format to be compatible with AutoDock Vina. As a result of these processes, EPA and DHA derived from krill oil were prepared for molecular docking analyses with target proteins.

3.4. Protein-Ligand Docking

Molecular docking analyses were conducted using AutoDock Vina software to investigate potential interactions between the protein structures 5MY6, 7PCD, and 8U8X and specific natural compounds. For each target protein, a three-dimensional grid box centered on the active site was defined, and the docking parameters were configured accordingly. AGFR software was used for this purpose.

Following the docking simulations, the binding modes and affinities of the ligands with the active sites of the target proteins were evaluated. Based on the obtained data, the most suitable conformations of the ligands were determined, and the binding energies of these positions were calculated. Thus, the potential interaction profiles of the relevant compounds with the target proteins were revealed at the molecular level.

3.5. Molecular Docking Application with AutoDock Vina

AutoDock Vina, widely used in molecular modeling and virtual screening, is powerful tools for predicting protein-ligand interactions. These software not only calculate the binding affinities of ligands to target proteins but also enable structural bioinformatics applications such as analyzing molecular surfaces, calculating hydrogen bonds, and visualizing secondary structure chains. These software, particularly widely used in inhibition-based drug discovery studies, offer effective computational approaches for predicting the binding modes of ligands with their protein targets.

In this study, molecular docking analyses were performed on the structures of 5MY6, 7PCD, and 8U8X, target protein receptors associated with breast cancer. The three-dimensional crystal structures of these receptors were obtained from the Protein Data Bank (RCSB PDB). To increase the reliability of the docking analyses, the grid box surrounding the binding site for each target protein was defined based on known active sites. The grid box center coordinates (x, y, z) and dimensions (size_x, size_y, size_z) were adjusted to completely encompass the potential binding pocket of the target protein (Table 2.12).

To determine the most probable binding conformations, the configuration was adjusted to create 100 different binding modes for each ligand. The energy range parameter was set to 4 kcal/mol to allow comparison between binding energies. This allowed for a detailed analysis of the alternative binding positions that the ligands could exhibit against the target proteins (Table 2.12).

Table 3.2. Area of the Grid box of the receptors with AGFR.

RECEPTORS	**5MY6**	**7PCD**	**8U8X**
center_x	7,436	8,226	-18,479
center_y	-33,204	-6,115	10,713
center_z	-41,119	-17,232	18,055
size_x	17,250	22,500	18
size_y	18	21	30
size_z	19	36	23
num modes = 100 energy range = 4			

Prior to docking, target proteins and ligands were converted to .pdbqt format to make them compatible with AutoDock Vina. Ligand structures were optimized based on their three-dimensional forms downloaded from the PubChem database. After energy minimization, rotary bonds were identified and Gasteiger charges were assigned to the ligandsIn the protein structures, water molecules and small cofactors were eliminated, polar hydrogen atoms were incorporated, and Kollman charges were assigned. These charges were calculated based on the AMBER force field, taking into account orbital electron densities, allowing for more accurate modeling of intermolecular electrostatic interactions.

Following the preparation steps, docking simulations were run for each receptor-ligand pair using AutoDock Vina. Docking parameters were defined in a configuration file and the simulations were initiated. Vina generated multiple binding conformations for each ligand and calculated the binding affinities (in kcal/mol) corresponding to these positions. The positions with the lowest binding energy were considered to reflect the potentially strongest interaction and were subjected to detailed analysis.

3.6. Molecular Dynamics Simulations with GROMACS

GROMACS software was used to perform molecular dynamics (MD) simulations to understand the dynamic behavior of protein-ligand complexes in biological environments. Based on docking analyses, the complexes with the lowest binding energy were selected, and simulations were initiated on these complexes. The atomic types, three-dimensional integrity, and bond structures of the selected structures were examined in detail using UCSF Chimera software, and necessary corrections were made.

After obtaining the ligand molecules from the PubChem database, structural energy minimization was applied and they were adapted for the simulation environment. After the protein and ligand structures were docking, coordinate information was determined, and the docking process was completed based on this information. The resulting complexes were saved as individual structures representing the best binding positions.

Topology and parameter files for the ligands were generated using the SwissParam tool to adapt small organic molecules to atomic force fields. These files include formats containing molecular structure information and force field parameters. Additionally, the necessary configuration files for use in protein-ligand simulations were obtained from open-source platforms and compiled. Polarized force fields were chosen to more realistically reflect the effects of the dielectric medium in the simulations, and a GROMACS-compatible force field such as CHARMM36 or CHARMM27 was selected.

After preparing the topology files, a three-dimensional simulation box large enough to contain all the atoms of the protein-ligand complex was created. The system was solvated by adding a sufficient number of water molecules to this box. The water model used was TIP3P, a computationally efficient and widely used model. The edges of the simulation box were generally kept at a distance of 2 nanometers to accurately model the interactions between molecules.

Following the solvation process, ion addition was performed to ensure the electrical neutrality of the system and lower its potential energy level. Following these preparatory steps, energy minimization was performed. This step is critical for eliminating high-energy conformations in the system and achieving a suitable initial conformation for simulationThe Particle Mesh Ewald (PME) method was employed to accurately compute long-range electrostatic interactions.

Following energy minimization, the system's thermal and mechanical equilibrium was achieved. First, NVT equilibration was performed for temperature equilibrium under constant volume conditions. This stage ensured that the temperature stabilized over time, and the system was fixed at a specific temperature. Subsequently, NPT equilibration was performed under constant pressure conditions, allowing the system's volume to be dynamically changed, and the desired pressure was achieved. Both equilibration processes took approximately 100 picoseconds, and commonly used thermostat and barostat algorithms were used in these stages.

Following the equilibrations, the system was prepared for molecular dynamics simulation, and the production phase began. During this production simulation, the

behavior of the protein-ligand complex was monitored over time, and the stability of the system was observed. Each simulation was planned to last approximately 50 nanoseconds. Conformational changes, bond interactions, and energy profiles were recorded throughout the simulation.

Once the simulation was completed, structural and dynamic analyses were performed using the obtained data. These analyses encompassed root mean square deviation (RMSD), root mean square fluctuation (RMSF), radius of gyration, hydrogen bond analysis, and energy calculations.. All of these analyses are crucial for assessing how protein-ligand interactions change over time and binding stability.

Table 3.3. Ligand Parameterization Files and Configuration Data for GROMACS Protein Ligand Simulation (*Welcome to the GROMACS Documentation! — GROMACS Documentation*, n.d.).

File Name	Explanation
LIG.mol2	The format containing the three-dimensional structure of the ligand and atomic information is used in parametric transformation.
LIG.pdb	Structural file containing coordinate information of the ligand; compatible with GROMACS.
LIG.itp	The file containing the topology definitions for the ligand is required for the energy calculation of the system in GROMACS.
LIG.rtf	CHARMM contains force field specific ligand topology information.
LIG.prm /LIG.par	It contains parametric data such as atom types, bond lengths and angles.
LIG.crd	Contains coordinate data of the ligand in fixed format; used for position control in some systems.

LIG.psf	File containing the full system topology in CHARMM format; defines the connections between atoms.
EM.mdp	It contains the control parameters required for energy minimization.
NVT.mdp	Parameter file used for temperature compensation at constant volume.
NPT.mdp	Used for pressure equilibration under constant pressure.
MD.mdp	Contains molecular dynamics simulation parameters during the production phase.
ions.mdp	It is the parameter file used when adding ions to the system.
sort_mol2_bonds.pl	It is a Perl script used to edit the bond information in ligand files.
topol.top	It is the main topology file that covers all molecules throughout the system.

3.7. Molecular Dynamics Simulations (Protein-Ligand Complex) Analysis

3.7.1. Pocket selection

Cluster analysis was performed to identify the different conformational states of the protein-ligand complex. This allowed the structures obtained during the simulation to be grouped based on their structural similarities. The RMSD (Root Mean Square Change) value for each structure was calculated to create an RMSD matrix, and then representative squares from each group were selected based on the resulting clusters. This analysis allowed the identification of the dominant conformations of the system and the identification of meaningful representative structures for use in further structural studies.

3.7.2. RMSD (Root Mean Square Deviation)

Root Mean Square Deviation (RMSD) analysis was conducted to assess the temporal structural fluctuations of the protein-ligand complex. This analysis quantitatively reveals the extent to which the molecular structure deviates from its initial reference conformation during the dynamic simulation. It is a particularly

effective method for determining the differences between the predicted structures obtained after modeling and the actual structures obtained during the simulation.

The RMSD value is defined as the root mean square difference between the atomic coordinates of the structure at each time step and the coordinates of the reference structure. This value is a key indicator for understanding the stability or conformational change of the system over time. In particular, this value is used to interpret whether proteins or complexes remain stable or undergo major structural transformations.

RMSD is calculated using the following mathematical formula (Sargsyan et al., 2017):

$$RMSD = \sqrt{\frac{\sum_{i=1}^{N} di^2}{N}}$$

Here, *N* is the total number of equivalent atoms, *di* is the distance between atom, and *i* in the two structures. Calculations are generally performed using atoms belonging to the protein backbone (e.g., Cα atoms), as this region is more decisive in terms of structural stability.

The resulting RMSD curve graphically represents the magnitude of the structural deviation against time. For example, a curve that exhibits high early fluctuations and then stabilizes may indicate that the system has reached a stable structure over time. Conversely, RMSD values that exhibit continuous increases or sudden changes indicate system instability or possible structural rearrangements.

RMSD.xvg code: “gmx rms -s MD.tpr -f MD_noPBC.xtc -o rmsd.xvg -tu ns”

3.7.3. RMSF (Root Mean Square Fluctuations)

In molecular dynamics simulations, RMSF (Root Mean Square Fluctuation) analysis is one of the most important analysis methods used to understand the dynamic

behavior of a biomolecule, especially proteins. RMSF measures the degree of flexibility—the extent to which each atom or residue moves relative to a specific reference position—over time. This provides detailed structural information about which regions of the protein are more rigid and which are more flexible.

Generally, low RMSF values indicate stable regions of the protein, while high RMSF values indicate regions with greater mobility or conformational changes. Such changes are most often observed in binding pockets, surface loops, terminals, or ligand-binding sites. RMSF analysis is critical for examining the structural changes that occur after binding, especially in the interaction regions of protein-ligand complexes (Pitera, 2014).

$$RMSF = \sqrt{\frac{1}{T}\sum_{j=1}^{T}\left[\vec{r}_{j,i} - \frac{1}{T}\sum_{k=1}^{T}\vec{r}_{k,i}\right]^2}$$

The RMSF expression represents the fluctuation, or mobility, of the atom in the simulation with respect to time. Here, rj,i denotes the position vector of the i-th atom at the j-th time step of the simulation, and ⟨ri⟩ denotes the average position of the same atom throughout the simulation. k is the counter used to sum the atom positions across all time steps to determine the average position. The total number of time steps is denoted by T. This formula provides a quantitative measure of local mobility and flexibility within the protein or molecule by calculating the extent to which each atom deviates from its mean position over time (Pitera, 2014).

RMSF.xvg code: “gmx rmsf -s MD.tpr -f nojump.xtc -o rmsf.xvg”

3.7.4. Hydrogen Bond Analysis (H-Bond)

Hydrogen bonds (H-bonds) are critical forms of stabilization in protein-ligand complexes, particularly in the active site. During molecular dynamics simulations, the number and positions of these bonds over time play a significant role in determining the dynamic stability of the complex (Prasad & Chakraborty, 2022).

The quantity and locations of hydrogen bonds formed between the ligand and receptor groups were examined using the GROMACS gmx hbond command. Using default geometric criteria (donor-acceptor distance ≤0.35 nm, H–D–A angle ≤30°), the continuity and durability of the bonds were examined.

hb.xvg: code running from the “gmx hbond -s MD.tpr -f nojump.xtc -num hb04.xvg -b 0 -e 4 -tu ns” to “gmx hbond -s MD.tpr -f nojump.xtc -num hb4650.xvg -b 46.01 -e 50 -tu ns”

3.7.5. Radius of Gyration (Rg)

Radius of gyration (Rg) is a widely used measure to assess the structural integrity and compactness of a macromolecule, particularly proteins, in three-dimensional space. This parameter is defined as the square root of the average squared distances of all atoms in a molecule from the center of mass. In other words, Rg quantifies how far the atoms surrounding the molecule are "spread out" relative to the center of mass.

In molecular dynamics simulations, the Rg value is calculated over time to analyze conformational changes that occur in a protein's structural stability or compactness. It is a particularly important indicator for understanding how factors such as ligand binding, pH changes, or mutations affect the protein's folding structure (*Theoretical Modeling of Nanostructured Formation in Polymer Blends | Request PDF*, n.d.).

m_i is identical mass,

r_i is variable distance,

$$Rg^2 = \frac{\sum m_i {r_i}^2}{\sum m_i}$$

gyrate1.xvg code: “gmx gyrate -s MD.tpr -f nojump.xtc -o gyrate1.xvg”

3.8. SwissADME: Pharmacokinetic and Toxicological Profiling

Computer-aided drug design (CADD) is a crucial methodology that facilitates the modeling of target-ligand interactions at the molecular scale, aiding in the identification of potential drug candidates. In this process, initial evaluation typically

begins with molecular docking analyses. Docking studies help predict binding modes and affinity levels by calculating how and with what strength small molecules interact with target protein binding sites. However, high binding energy alone is not sufficient for a compound to be an effective drug candidate. During the drug development process, it is necessary to evaluate the toxicological properties of candidate molecules, along with their absorption, distribution, metabolism, and elimination (ADME) profiles. Such in silico predictions provide significant time and cost advantages in early-stage screening (Daina et al., 2017).

In this study, the binding properties of lapatinib, a reference molecule with anticancer activity, along with eicosapentaenoic acid (EPA) and docosahexaenoic acid (DHA), both natural omega-3 fatty acids derived from krill oil, on the protein targets 5MY6, 7PCD, and 8U8X were investigated using molecular docking. Following the docking analyses, the pharmaceutical suitability and pharmacokinetic profiles of these compounds were assessed using the SwissADME platform.

SwissADME is an open-access, user-friendly web tool that can predict various pharmacokinetic, lipophilicity, and drug-likeness parameters based on molecule structural data in SMILES format. The platform employs algorithms specifically optimized for small molecules and utilizes various models for prediction. These include: These include the ESOL model, which calculates the molecule's water solubility; the BOILED-Egg model, which evaluates gastrointestinal absorption and blood-brain barrier passage; and the Bioavailability Radar, which visualizes drug similarity profiles (Daina et al., 2017).

SwissADME also provides pharmaceutical suitability filters by evaluating molecules according to classical drug similarity rules such as Lipinski, Veber, Ghose, Egan, and Muegge. Furthermore, it can identify functional groups that pose a potential risk of toxicity or that may cause problems in screening libraries using the PAINS and Brenk structural alert filters (Brenk et al., 2008). The synthetic accessibility (SA) score, used to assess a molecule's synthesizability, is calculated on a scale ranging from 1 to 10, based on the molecule's structural complexity (Daina et al., 2017).

One of the key advantages of SwissADME is its ability to perform rapid, multi-molecular analysis without access barriers. Furthermore, thanks to its integration with the SwissDrugDesign platform, users can also perform analyses compatible with other tools such as SwissDock, SwissSimilarity, and SwissTargetPrediction. These features make SwissADME a widely used tool for preliminary evaluation of candidate molecules in the early stages of drug discovery (Daina et al., 2017).

CHAPTER IV. RESEARCH FINDING AND DISCUSSION

In this study, conformational changes were examined through molecular docking and molecular dynamics (MD) simulation techniques, focusing on the HER2 protein within breast cancer research. Three different crystal structures of the HER2 protein (PDB ID: 5MY6, 7PCD, and 8U8X) were selected based on a literature search. Docking studies were conducted targeting the active sites of these receptors.

Lapatinib, a widely used drug, was used as the reference drug, and its interactions with HER2 receptors were compared. Comparative docking analyses were conducted with a total of 54 drug molecules. Additionally, eicosapentaenoic acid (EPA) and docosahexaenoic acid (DHA), derived from krill oil, a natural source, were included in the study to assess their potential interactions with HER2.

Following the docking analyses, further analyses were conducted. Molecular dynamics simulations were performed to form a HER2 complex with these two ligands and a drug, and the binding stability, dynamic behavior, and structural effects of the ligands were examined in detail.

The results indicate that natural compounds such as EPA and DHA can be considered as potential therapeutic candidates in the design of new HER2-targeting molecules. This study was conducted to contribute to the development of targeted drugs for the treatment of breast cancer.

4.1. Molecular Docking Results

Molecular docking analyses were primarily conducted to evaluate the interaction potential of EPA (Eicosapentaenoic Acid) and DHA (Docosahexaenoic

Acid), derived from krill oil, with the breast cancer-associated HER2 protein. The docking phase was conducted with 54 different anticancer drugs from the literature and Lapatinib as a reference compound to comparatively examine the therapeutic effects of these natural compounds.

To ensure accuracy and comprehensive analysis of the results, the docking processes were performed using three different software programs: AutoDock Vina and UCSF Chimera software were employed in this study. AutoDock Vina was utilized to compute the binding energies of the molecules to the HER2 receptor, while UCSF Chimera facilitated the preparation of protein and ligand structures, the definition of binding sites, and the optimization of grid box parameters.

In each docking study, binding sites were positioned to focus on the active site of the HER2 receptor; Grid boxes were sized to completely encompass the target regions. This systematic approach increased the accuracy of the binding scores obtained and ensured the structural accuracy of the ligands' binding positions.

As a result of docking analyses, the binding affinities of EPA and DHA with the HER2 protein were evaluated in terms of both binding energies and molecular interaction profiles. The findings suggest that these natural compounds may exhibit potential inhibitory properties on HER2 and contribute to the understanding of interaction mechanisms at the molecular level.

Table 4.1. Ligand-receptor complexes with lowest binding energy

Receptors	Ligands and drug with CHEMBL ID	Lowest Binding Energy (kcal/mol)
5MY6	Lapatinib	-8,2
	EPA	-6,2
	DHA	-6,5
7PCD	Lapatinib	-10,8
	EPA	-7,1
	DHA	-7,3
8U8X	Lapatinib	-11,7
	EPA	-7,7
	DHA	-8,0

.

4.1.1. Molecular Docking Studies with 5MY6

In breast cancer, overexpression of the HER2 (Human Epidermal Growth Factor Receptor 2) protein drives aggressive tumor progression by enhancing cellular proliferation. Small molecule inhibitors targeting this receptor play a crucial role, particularly in the treatment of HER2-positive breast cancer. This study investigated the therapeutic potential of natural compounds using the 5MY6 receptor, which has the crystal structure of HER2.

Lapatinib was selected as the reference compound, and comparative molecular docking studies were conducted with the omega-3 fatty acids EPA (eicosapentaenoic acid) and DHA (docosahexaenoic acid) derived from krill oil. Docking analyses were performed using AutoDock Vina software.

The optimized grid box dimensions and center coordinates for the 5MY6 receptor for docking studies are detailed in Table 4.2. For more precise identification of binding sites, the grid box coordinates were kept constant; Separate docking simulations were performed using the actual position of the center coordinate and three different grid sizes (20, 30, 40). As a result of these studies, the potential binding sites of EPA and DHA on the HER2 receptor were determined, and the obtained binding energies were compared with the reference drug Lapatinib to evaluate the therapeutic capacity of these compounds.

Table 4.2. Grid parameter file of 5MY6 receptor and ligands with AutuDock

GRID PARAMETER FILE			
Macromolecule	**5MY6**		
Models	Lapatinib	EPA	DHA
# of grind size in xyz	17.250 18.000 19.500		
Spacing (Å)	0.375		
xyz grid-center coordinates	7.436		
	-33.204		
	-41.119		
Temperature (K)	298.15		
Charges	Gasteiger		
Num_modes	100		
Energy_range	4		
Exhaustiveness	16		

Table 4.2 contains information on the grid parameters used in molecular docking analyses against the 5MY6 protein. The grid parameter file contains the basic settings used to identify potential sites where ligands can bind to the target protein and optimize the search space. In this context, the models created for Lapatinib, EPA (eicosapentaenoic acid), and DHA (docosahexaenoic acid) ligands were based on a common grid structure.

Initially, the grid dimensions (dimensions along the x, y, and z axes) were set to 17,250, 18,000, and 19,500 Å, respectively. These values define the three-dimensional boundaries of the area where ligands can bind. The grid spacing was set to 0.375 Å; this value represents the distance between grid points during the docking process; smaller values allow for more precise but more time-consuming calculations. The coordinates of the grid center were determined as x = 7.436, y = -33.204, and z = -41.119, respectively. This center defines the region where the binding pocket is positioned and ensures that ligands are optimized in regions with the highest binding potential. Docking calculations were performed at 298.15 K (25 °C), which is close to standard biological temperature. This parameter allows molecular dynamics behavior to be modeled in accordance with physiological conditions. Gasteiger charges were used in the analyses. This charge type rapidly and parametrically estimates the electrostatic charge distribution on ligands. It is widely preferred in docking studies, especially with small molecules, and shows high compatibility with AutoDock-based programs. In addition, a maximum of 100 different binding modes (Num_modes) were scanned for each ligand in the docking protocol, the energy range (Energy_range) was set at 4 kcal/mol, and the exhaustiveness (computational coverage) value was selected as 16. These parameters both increase the diversity of binding modes and control the level of detail of the simulation.

As a result, the grid structure created based on these parameters allowed for accurate and efficient analysis of the binding behavior of ligands towards the 5MY6 protein.

Based on the AutoDock Vina results, the conformations with the lowest binding energy were selected and visualized using Discovery Studio. Figure 4.1 shows

the interaction structure of the amino acids in the conformation obtained after docking between the 5MY6 receptor and the Lapatinib molecule.

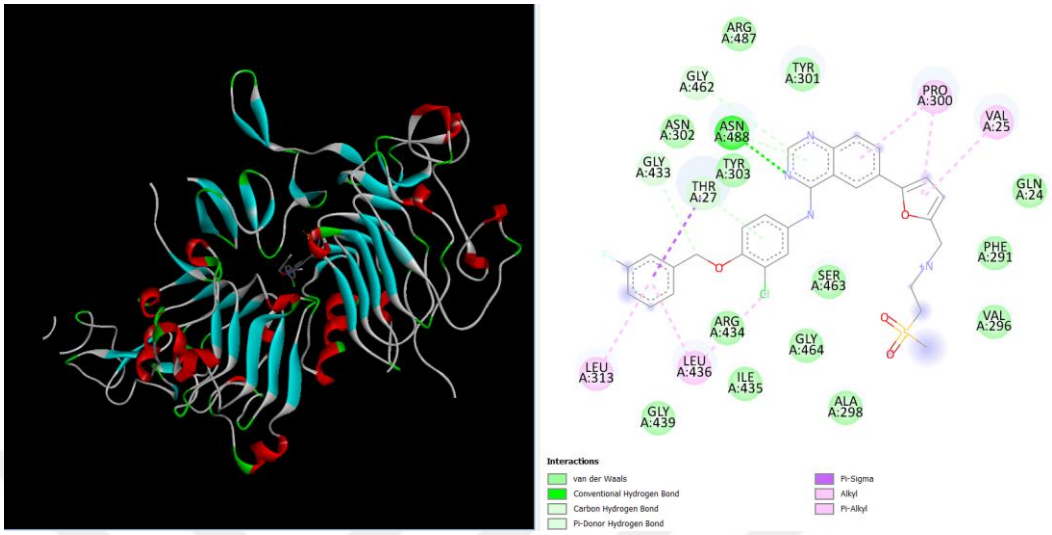

Figure 4.1. Discovery Studio 3D and 2D ligand-protein interaction diagram showing Lapatinib interactions with the 5MY6 receptor.

Figure 4.1 shows the conformation with the lowest binding energy obtained from the interaction of the Lapatinib molecule with the 5MY6 crystal structure of the HER2 receptor. Docking studies revealed that Lapatinib binds to the receptor's active site with high affinity and stabilizes this binding through various interactions. Images generated using Discovery Studio reveal multiple conventional hydrogen bonds between the Lapatinib molecule and the receptor (with GLN A:81, TYR A:303, ASN A:488, and GLY A:464). These hydrogen bonds play a key role in maintaining the ligand in the binding site. In addition, carbon-hydrogen bonds were determined to form with residues THR A:27 and GLN A:57. Halogen interactions are also noteworthy; in particular, the halogen bond formed between Lapatinib's fluorine atom and GLN A:57 is a significant factor contributing to binding stability. Additionally, π-π T-shaped and π-alkyl interactions were observed with hydrophobic amino acid residues such as VAL A:25, VAL A:55, and PRO A:300. Such hydrophobic interactions further stabilize the binding site. These data demonstrate that lapatinib binds specifically to the HER2 receptor and strongly localizes to the ATP-binding pocket through multiple interactions. As reported in the literature, such multi-site binding is critical for the efficacy of tyrosine kinase inhibitors.

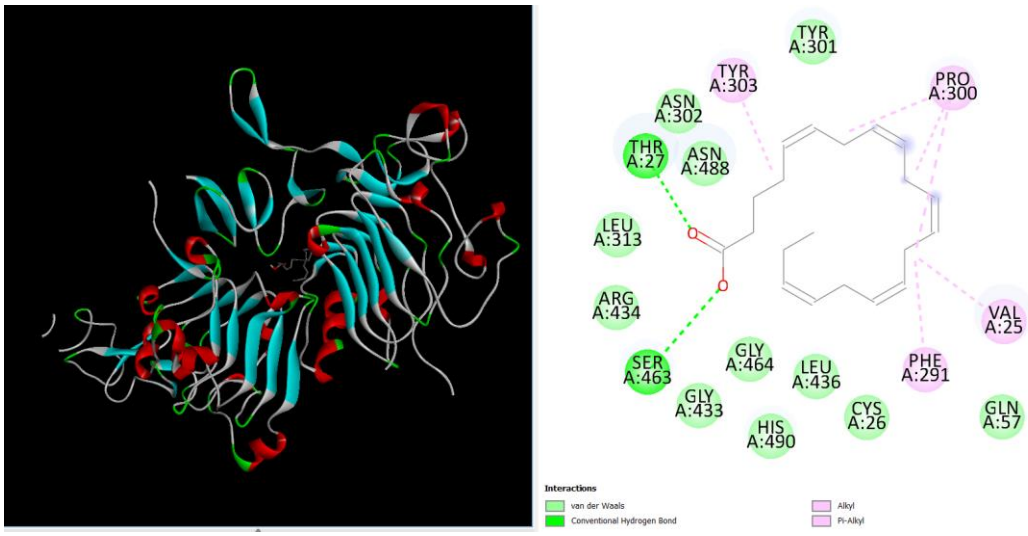

Figure 4.2. Discovery Studio 3D and 2D ligand-protein interaction diagram showing EPA with the 5MY6 receptor.

Figure 4.2 shows the conformation with the lowest binding energy in a docking simulation of the eicosapentaenoic acid (EPA) molecule using the 5MY6 structure of the HER2 tyrosine kinase receptor. The image clearly shows the interactions EPA forms with some critical amino acid residues as it docked in the active site of the HER2 receptor. This visualized binding model provides important information about EPA's structural properties and binding mode.

EPA is a long-chain, polyunsaturated omega-3 fatty acid. Due to the flexible nature of its hydrocarbon chain, it generally binds to protein targets through hydrophobic and van der Waals interactions. Visual analysis reveals that the EPA molecule is retained in the receptor's binding site primarily through hydrophobic interactions. In this structure analyzed by Discovery Studio, π-alkyl and alkyl interactions were identified between EPA and LEU A:465 and HIS A:490 residues. Such interactions contribute to stabilizing the molecule's position in hydrophobic regions (R. D. Smith et al., 2006).

The fact that EPA does not form hydrogen bonds or electrostatic interactions with the receptor suggests that its binding affinity may be lower compared to target-specific small molecule inhibitors such as Lapatinib. However, the multiple hydrophobic contacts it makes with a functionally important amino acid such as HIS A:490 demonstrate that EPA localizes to the HER2 kinase domain and exhibits a

specific fit to the target site. The literature has reported that omega-3 fatty acids modulate signaling through indirect effects on membrane structure and receptor conformation, rather than directly binding to some receptors (Calder, 2015). In this context, EPA binding to the HER2 receptor may be effective through conformational changes rather than direct inhibition.

In conclusion, the binding pattern of EPA to the 5MY6 receptor differs from the classical inhibitory binding pattern, appearing to occur primarily through hydrophobic surface conformation and van der Waals forces. This suggests that EPA could be considered a supportive or modulatory agent, rather than a direct inhibitor, in HER2-targeted therapies.

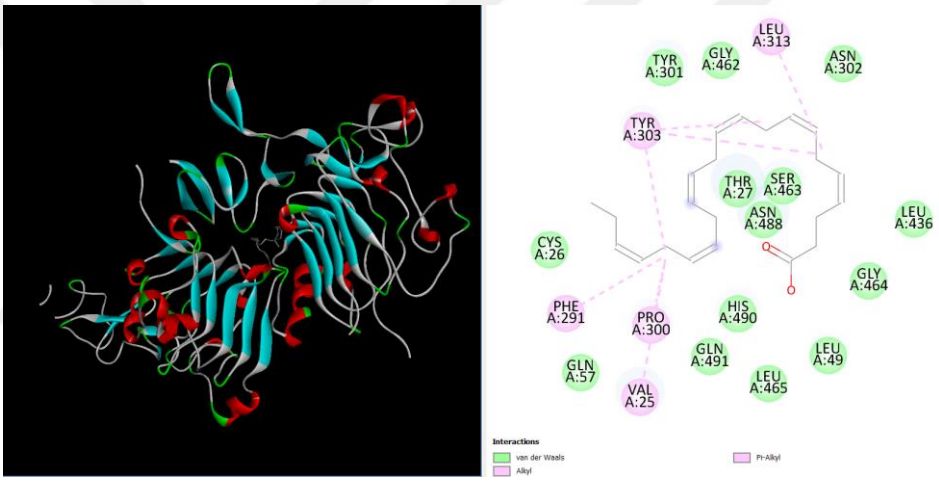

Figure 4.3. Discovery Studio 3D and 2D ligand-protein interaction diagram showing DHA with the 5MY6 receptor.

Figure 4.3 shows the binding of the docosahexaenoic acid (DHA) molecule to the HER2 (5MY6) receptor. DHA is a long-chain, polyunsaturated omega-3 fatty acid, and an examination of the binding model reveals that the ligand engages the active site of the HER2 receptor through various non-covalent interactions. Analysis with Discovery Studio identified significant interactions between the DHA molecule and HIS A:349 and GLU A:363 residues on the receptor.

The DHA molecule structurally contains functional groups capable of both hydrogen bonding and ionic interactions. In the image, DHA is observed to form pi-donor hydrogen bonds with HIS A:349 through its hydroxyl and carboxyl groups. Such

interactions play a key role in determining the ligand's orientation and placement within the binding pocket (Calder, 2015). Furthermore, the positively charged amine group of DHA appears to form a salt bridge with the negatively charged GLU A:363 residue. This interaction is quite strong due to its ionic character and is an important factor that increases the stability of the ligand-receptor complex.

This binding mechanism of DHA to the 5MY6 receptor differs from that of classical tyrosine kinase inhibitors. Compared to EPA, DHA's greater number of unsaturated bonds increases the flexibility of the molecule and allows it to fit more comfortably into the receptor's binding site (Schley et al., 2007). In particular, the presence of both hydrogen bonds and ionic bridges at the same binding site suggests that DHA may exhibit receptor-specific binding behavior.

This binding pattern of DHA on HER2 suggests that it is not a direct tyrosine kinase inhibitor, but rather a molecule that can indirectly modulate receptor activity. Indeed, the literature reports that DHA reduces HER2 expression and exhibits suppressive effects on tyrosine kinase signaling pathways (Corsetto et al., 2011; Zou et al., 2013). In this context, this interaction profile formed by DHA binding to the receptor sheds light on the molecular basis of its biological effects.

4.1.2. Molecular Docking Studies with 7PCD

The binding potential of naturally occurring omega-3 fatty acid derivatives to this receptor was investigated using the 7PCD crystal structure, which represents the three-dimensional structure of HER2. Lapatinib, a clinically approved HER2 inhibitor, was selected as the reference compound, and this molecule was compared with eicosapentaenoic acid (EPA) and docosahexaenoic acid (DHA), natural omega-3 fatty acids derived from krill oil. Molecular docking analyses were performed using AutoDock Vina software to predict the binding affinities of ligands to the 7PCD receptor.

The grid box dimensions and center coordinates, optimized using the 8U8X crystal structure of the HER2 protein as part of the docking protocol, are shown in Table 4.2. To more precisely define the binding sites, the grid box coordinates were kept constant; However, based on the location of the center coordinates, four separate

docking analyses were performed with different box sizes (20, 30, and 40). As a result of these calculations, potential interaction sites of EPA and DHA molecules derived from krill oil with the 8U8X receptor were identified; the binding affinities of these natural compounds were compared with those of Lapatinib, which is currently in clinical use, and evaluated for therapeutic relevance.

Table 4.3. Grid parameter file of 7PCD receptor and ligands with AutuDock.

GRID PARAMETER FILE			
Macromolecule	**7PCD**		
Models	Lapatinib	EPA	DHA
# of grind size in xyz	22.500 21.000 36.000		
Spacing (Å)	0.375		
xyz grid-center coordinates	8.226		
	-6.115		
	-17.232		
Temperature (K)	298.15		
Charges	Gasteiger		
Num_modes	100		
Energy_range	4		
Exhaustiveness	16		

Table 4.6 includes the actual location coordinates and other parameters of the docking analysis.

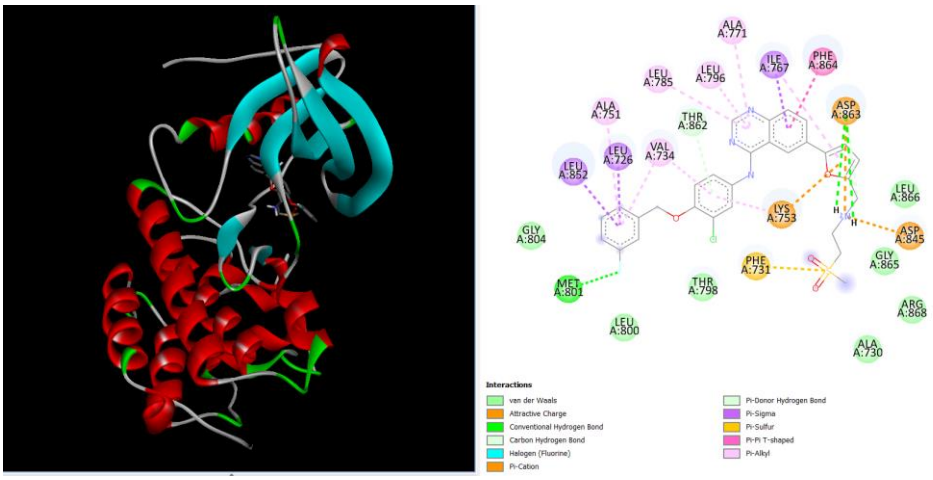

Figure 4.4. Discovery Studio 3D and 2D ligand-protein interaction diagram showing Lapatinib interactions with the 7PCD receptor.

Figure 4.4 depicts the molecular interactions between the ligand and the target protein in detail. The left panel displays the three-dimensional structure of the protein-ligand complex, while the right panel presents a two-dimensional interaction map of the complex.

The interaction map indicates the different bond types formed by the ligand with the amino acid residues in the protein binding site, indicated by color codes. Conventional hydrogen bonds, shown in green, contribute significantly to complex stability by creating strong electrostatic bonds between the ligand and residues ASP863, THR862, and GLY865 (Kumar et al., 2015). Salt bridges, shown in orange, represent the electrostatic attraction between the ligand's ionic groups and oppositely charged amino acid residues on the protein; these interactions play a critical role in increasing binding affinity (Wang et al., 2016). In addition, halogen bonds (blue), pi-cation (orange), pi-alkyl (pink), and pi-pi T-shaped interactions (dark pink) demonstrate the hydrophobic and electronic compatibility between the ligand and aromatic residues. These bonds enhance the ligand's conformational fit in the binding site, supporting its specificity (Chen et al., 2019).

These interactions in the three-dimensional structure ensure stable binding of the ligand to the target protein, demonstrating that the molecular docking results are biologically relevant and suggest that the ligand may be a potential inhibitor.

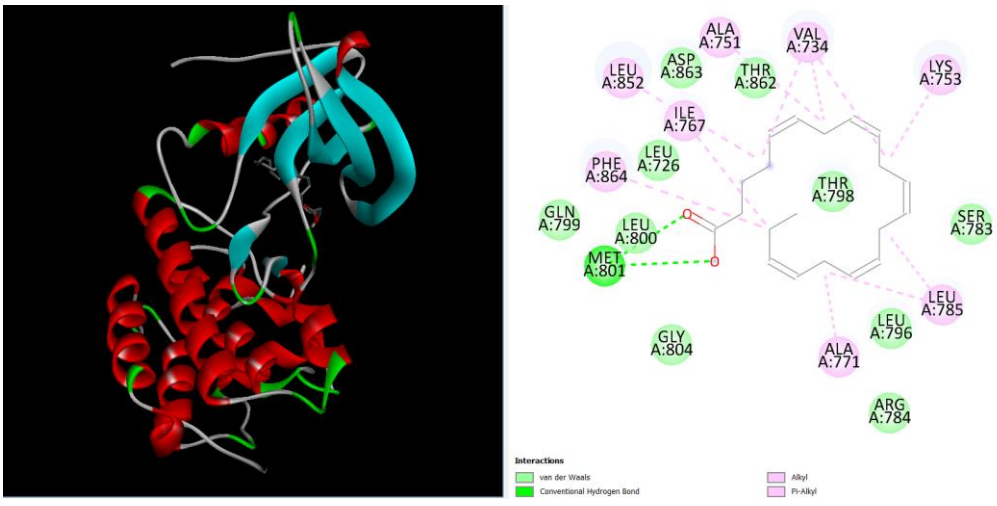

Figure 4.5. Discovery Studio 3D and 2D ligand-protein interaction diagram showing EPA interactions with the 7PCD receptor.

Figure 4.5 provides a detailed representation of the molecular interactions between the ligand and the target protein binding site. The protein-ligand complex is shown in three dimensions on the left, while the two-dimensional interaction map on the right shows the ligand's binding sites on the protein and the types of interactions.

Only two types of interactions are observed in the interaction map: conventional hydrogen bonding (shown in green) and alkyl interactions (in light purple). Conventional hydrogen bonding refers to the hydrogen bonding of the ligand's carboxyl group to residue ASP863 on the protein. These hydrogen bonds promote strong and specific binding of the ligand to the binding site, increasing complex stability. Alkyl interactions indicate that the ligand's hydrophobic regions interact with numerous hydrophobic amino acid residues (LEU, LYS, VAL, PHE, ALA, and MET) on the protein. These hydrophobic contacts ensure the ligand adopts the appropriate conformation at the binding site, thus supporting the thermodynamic stability of the ligand-protein complex.

In general, ligand binding to protein is mediated primarily by hydrogen bonding and hydrophobic interactions. This binding pattern demonstrates the ligand's good affinity for the protein and is important for understanding the molecular basis of its biological activities.

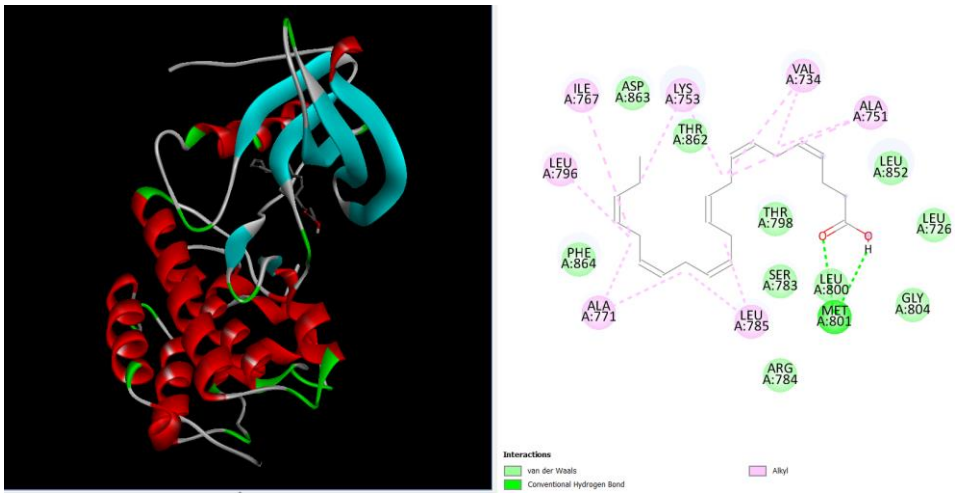

Figure 4.6. Discovery Studio 3D and 2D ligand-protein interaction diagram showing DHA interactions with the 7PCD receptor.

Figure 4.6 presents a detailed three-dimensional (left) and two-dimensional (right) representation of the molecular interactions of the DHA ligand with the binding site of the 7PCD receptor. The two-dimensional interaction map shows that the ligand forms various types of interactions on the target protein. These interactions include conventional hydrogen bonds (green), salt bridges (orange), and carbon-hydrogen bonds (light green).

Conventional hydrogen bonds refer to the bonds formed by the ligand with residues SER 890, SER 907, ARG 844, and ALA 890 on the protein. These bonds allow the ligand to attach to the binding site with high specificity and increase the stability of the complex. The salt bridge represents the electrostatic attraction between the positively charged amino group of the ligand and the negatively charged residue ASP 904 on the protein. Salt bridge interactions play a critical role in the stability of the ligand-protein complex. Additionally, carbon-hydrogen bonds indicate that the ligand forms weak but additive interactions with residues MET 889 and SER 903.

This interaction profile demonstrates that the ligand binds strongly and specifically to the target protein and has potentially high biological activity. The presence of both hydrogen bonds and salt bridge interactions supports increased binding affinity and selectivity.

4.1.3. Molecular Docking Studies with 8U8X

The 8U8X crystal structure was used as the three-dimensional structure of the HER2 receptor, and the binding potential of naturally occurring omega-3 fatty acid derivatives was investigated on this structure. Lapatinib, a clinically approved HER2 inhibitor, was compared with eicosapentaenoic acid (EPA) and docosahexaenoic acid (DHA), two major long-chain polyunsaturated fatty acids derived from krill oil. Molecular docking studies were conducted using AutoDock. Vina software to estimate the binding affinities of ligands on the receptor.

The grid box sizes and center coordinates optimized using the 8U8X crystal structure of the HER2 protein as part of the docking protocol are shown in Table 4.2. To more precisely define the binding sites, the grid box coordinates were kept constant; however, four separate docking analyses were conducted with different box sizes (20,

30, and 40) based on the location of the center coordinates. As a result of these calculations, the possible interaction sites of EPA and DHA molecules derived from krill oil with the 8U8X receptor were determined; the binding affinities of these natural compounds were evaluated from a therapeutic perspective by comparing them with Lapatinib, which is in clinical use.

Table 4.4 includes the actual location coordinates and other parameters of the docking analysis.

Table 4.4. Grid parameter file of 8U8X receptor and ligands with AutuDock.

GRID PARAMETER FILE			
Macromolecule	**8U8X**		
Models	Lapatinib	EPA	DHA
# of grind size in xyz	18.000 30.000 23.250		
Spacing (Å)	0.375		
xyz grid-center coordinates	-18.479		
	10.713		
	18.055		
Temperature (K)	298.15		
Charges	Gasteiger		
Num_modes	100		
Energy_range	4		
Exhaustiveness	16		

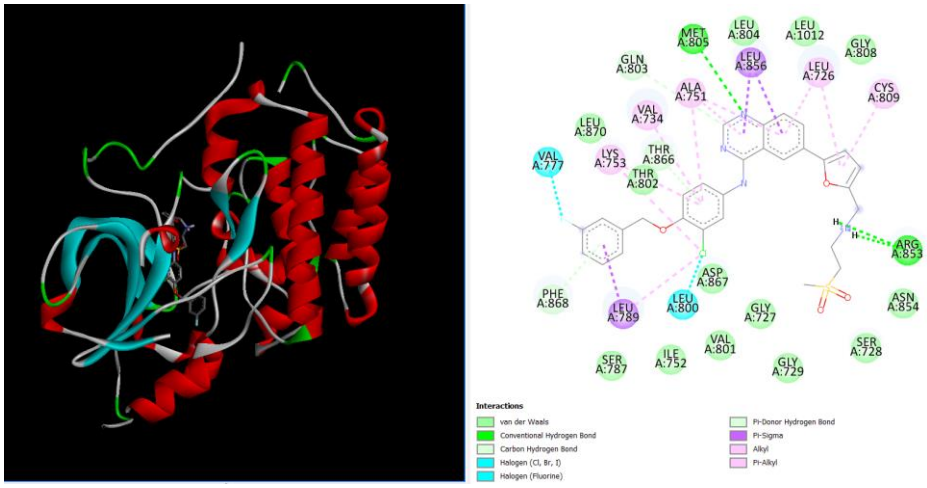

Figure 4.7. Discovery Studio 3D and 2D ligand-protein interaction diagram showing Lapatinib interactions with the 8U8X receptor.

Figure 4.7 shows the binding conformation of the Lapatinib molecule on the 8U8X crystal structure of the HER2 receptor and its interactions within the receptor in both three-dimensional and two-dimensional views. According to molecular docking analysis, Lapatinib establishes various strong interactions with the target protein, locating the binding site with high affinity. The molecule was observed to form conventional hydrogen bonds with residues MET805 and LEU726. These bonds stabilize the ligand in the binding site, increasing its specificity. Furthermore, the halogen bond formed with VAL777 via the fluorine atom contributes to the ligand's conformational stability. The literature emphasizes that such bonds are particularly important for protein-ligand complex stability.

Lapatinib also interacts with ASP867 via a carbon-hydrogen bond, which helps the molecule orient itself to the binding site. In hydrophobic regions, alkyl, pi-alkyl, and pi-sigma interactions are formed with amino acid residues such as LEU800, LEU870, VAL734, LEU789, ALA751, and MET805. These hydrophobic interactions, in particular, enhance the structural conformation of the binding pocket, lowering the ligand's binding energy and increasing affinity. Lapatinib's versatile interactions with the HER2 receptor form the molecular basis for this molecule's high therapeutic efficacy.

Figure 4.8 shows the binding location and interactions of the natural omega-3 fatty acid eicosapentaenoic acid (EPA) molecule with the 8U8X receptor. The left panel shows the three-dimensional binding conformation of EPA, while the right panel presents a two-dimensional schematic representation of the molecular interactions mediating this binding.

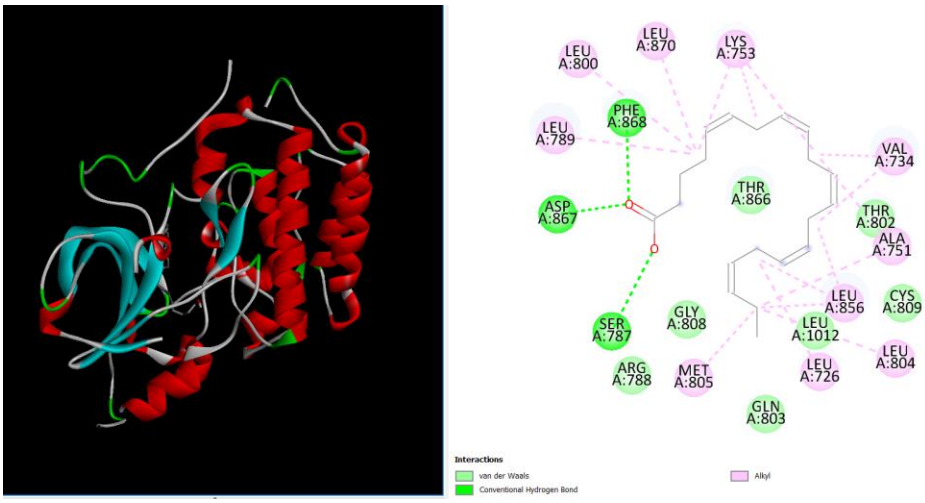

Figure 4.8. Discovery Studio 3D and 2D ligand-protein interaction diagram showing EPA interactions with the 8U8X receptor.

The first element that stands out in the interaction of EPA with the HER2 receptor is the conventional hydrogen bond formed by the carbonyl group with the amino acid SER787. This interaction can be considered a significant stabilizing force that allows the ligand to orient itself toward the binding site. Hydrogen bonds play a critical role in determining both the accuracy and stability of the molecule's binding conformation. This bond demonstrates that the polarized end of EPA establishes a specific and strong contact with the receptor. In addition, EPA's long, nonpolar hydrocarbon chain forms various alkyl and pi-alkyl interactions with the hydrophobic residues LEU800, LEU856, LEU1012, PHE868, LYS753, VAL734, and ALA751 in the binding pocket. Such hydrophobic interactions are particularly decisive factors in the binding of lipophilic molecules to proteins. These interactions between nonpolar regions increase the binding surface area and enhance affinity.

Considering the structural properties of EPA, its polyunsaturated long-chain structure allows it to extend into different subregions of the binding pocket and form various hydrocarbon-based interactions. This contributes to binding stability and stabilizes the ligand's position.

Overall, EPA's binding to the HER2 receptor occurred through both polar (hydrogen bonding) and nonpolar (hydrophobic interactions). This demonstrates the molecule's versatile interaction profile with the receptor. However, EPA's binding

energy and inhibitory potency may be lower than those of clinical HER2 inhibitors such as lapatinib. Molecular dynamics simulations and biological validation studies are necessary to clarify the therapeutic efficacy of such natural compounds.

Figure 4.9 shows the binding conformation and molecular interaction profile of docosahexaenoic acid (DHA), a natural omega-3 fatty acid, with the HER2 tyrosine kinase receptor (PDB ID: 8U8X). The left panel shows the three-dimensional binding position of DHA on the target protein; the right panel presents the two-dimensional interactions corresponding to this binding position.

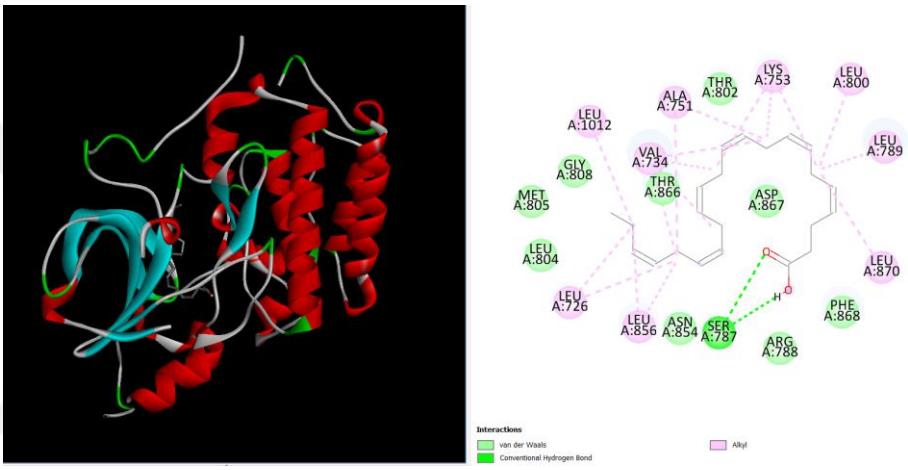

Figure 4.9. Discovery Studio 3D and 2D ligand-protein interaction diagram showing DHA interactions with the 8U8X receptor.

The DHA molecule has multiple important interactions at the receptor binding site. Conventional hydrogen bonding, particularly with residue GLU878, contributes to the specific binding of DHA to the receptor. Hydrogen bonds are critical for the orientation and stability of ligand-protein complexes and contribute positively to binding energy. Furthermore, the carbon-hydrogen bond formed with ALA730 facilitates the proper orientation of DHA within the binding pocket. More strikingly, the DHA molecule has formed electrostatic interactions with residues ARG853, ASP849, and ASP867 on the receptor. The salt bridges and attractive charge interactions observed with these residues increase the ionic stability of the binding complex and ensure the retention of DHA within the binding pocket. Such ionic interactions support the inhibitory effect of the ligand. In addition, van der Waals contacts observed with residues such as LEU870, PHE731, and ASN854 allow DHA

to interact with a larger surface area in the binding site, increasing binding affinity. These weak but extensive contacts stabilize the binding conformations of nonpolar, long-chain molecules like DHA.

In conclusion, DHA appears to be held in the HER2 binding pocket by various types of interactions, particularly hydrogen bonds and ionic interactions, maintaining a stable binding conformation. This interaction profile of DHA suggests that it may have potential biological activity in HER2-targeted molecular interventions. However, further dynamic and biological validation studies are required before such natural compounds can be considered inhibitors.

4.1.5. SwissADME-Based Evaluation

Figure 4.10 presents the SwissADME pharmaceutical evaluation of the DHA molecule for targets 5MY6, 7PCD, and 8U8X, showing that DHA has a molecular weight of 328.49 g/mol, moderate polarity (TPSA 37.30 $Å^2$), and high lipophilicity (consensus Log P 5.87), which leads to poor to moderate water solubility. It exhibits high gastrointestinal absorption but is not permeable to the blood-brain barrier and only inhibits CYP2C9 among key cytochrome enzymes. While DHA slightly violates Lipinski and other druglikeness rules mainly due to its lipophilicity and number of rotatable bonds, it has a good bioavailability score (0.85) and no PAINS alerts, indicating favorable oral bioavailability and low assay interference risk. However, its poor solubility and CYP2C9 inhibition should be considered in further drug development and formulation efforts.

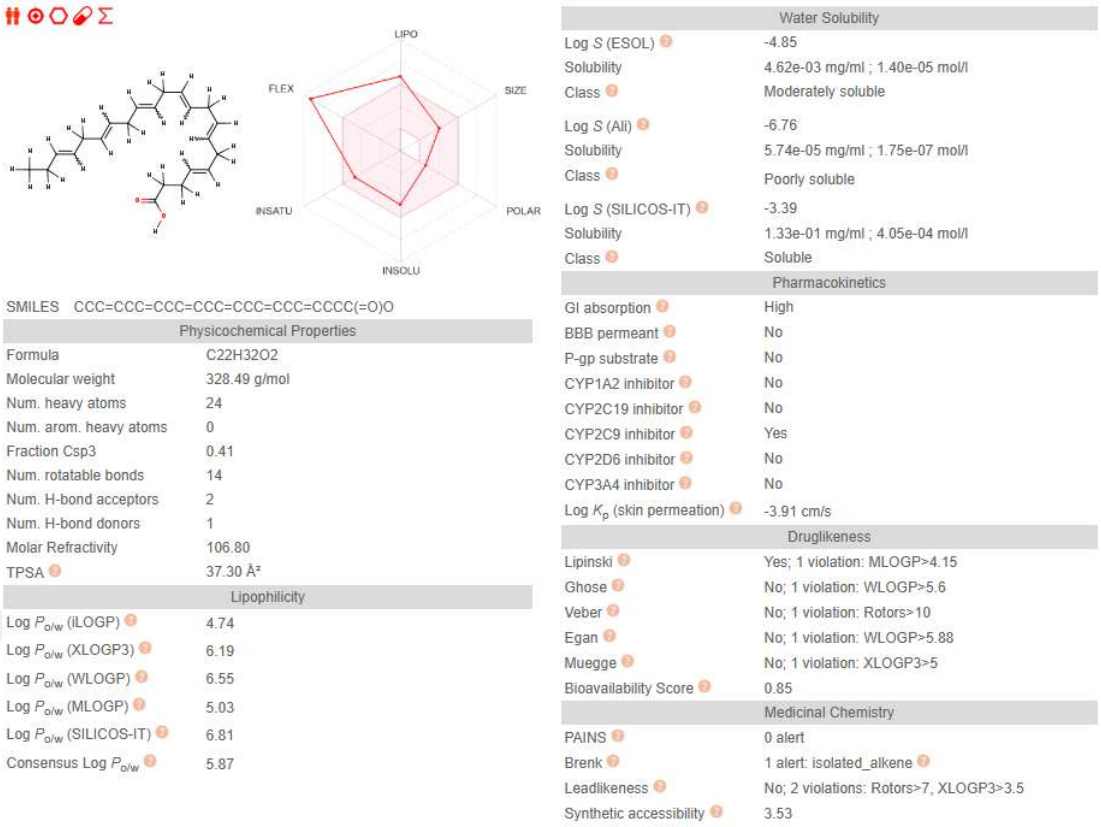

Figure 4.10. SwissADME-Based Pharmaceutical Evaluation of the DHA Molecule for Targets 5MY6, 7PCD, and 8U8X

EPA, the results of which are shown in Figure 4.11, has a larger and more lipophilic structure compared to DHA. Its molecular weight is 302.45 g/mol, which is still acceptable for oral bioavailability. However, its lipophilicity value is quite high (consensus log Po/w: 5.49), which significantly reduces the molecule's water solubility (ESOL log S: -4.82). Despite its low water solubility, gastrointestinal absorption is high. Its CYP2C9 inhibition requires caution regarding potential drug-drug interactions. Its TPSA value (37.30 Å²) is quite low, and while this provides advantages for receptor binding at lipophilic sites, it may be limiting for hydrophilic targets. Although it meets the Lipinski rules, there is a violation due to the MLOGP value. Additionally, there are structural violations (number of rotary bonds and log P values) in the Veber and Ghose rules. Its synthetic availability is lower than that of DHA (3.18), but still reasonable. In general, EPA exhibits a more complex and lipophilic pharmaceutical profile than DHA, which may limit its bioavailability and solubility.

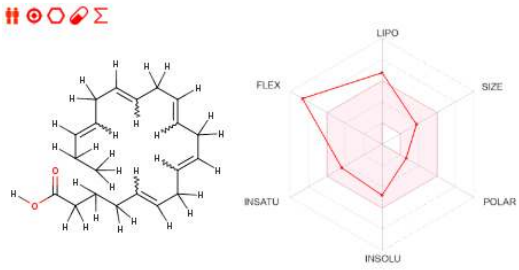

SMILES CCC=CCC=CCC=CCC=CCC=CCCCC(=O)O

Physicochemical Properties	
Formula	C20H30O2
Molecular weight	302.45 g/mol
Num. heavy atoms	22
Num. arom. heavy atoms	0
Fraction Csp3	0.45
Num. rotatable bonds	13
Num. H-bond acceptors	2
Num. H-bond donors	1
Molar Refractivity	97.66
TPSA	37.30 Å²
Lipophilicity	
Log $P_{o/w}$ (iLOGP)	4.39
Log $P_{o/w}$ (XLOGP3)	6.29
Log $P_{o/w}$ (WLOGP)	5.99
Log $P_{o/w}$ (MLOGP)	4.67
Log $P_{o/w}$ (SILICOS-IT)	6.11
Consensus Log $P_{o/w}$	5.49

Water Solubility	
Log *S* (ESOL)	-4.82
Solubility	4.58e-03 mg/ml ; 1.51e-05 mol/l
Class	Moderately soluble
Log *S* (Ali)	-6.86
Solubility	4.16e-05 mg/ml ; 1.38e-07 mol/l
Class	Poorly soluble
Log *S* (SILICOS-IT)	-3.32
Solubility	1.46e-01 mg/ml ; 4.82e-04 mol/l
Class	Soluble
Pharmacokinetics	
GI absorption	High
BBB permeant	No
P-gp substrate	No
CYP1A2 inhibitor	No
CYP2C19 inhibitor	No
CYP2C9 inhibitor	Yes
CYP2D6 inhibitor	No
CYP3A4 inhibitor	No
Log K_p (skin permeation)	-3.68 cm/s
Druglikeness	
Lipinski	Yes; 1 violation: MLOGP>4.15
Ghose	No; 1 violation: WLOGP>5.6
Veber	No; 1 violation: Rotors>10
Egan	No; 1 violation: WLOGP>5.88
Muegge	No; 1 violation: XLOGP3>5
Bioavailability Score	0.85
Medicinal Chemistry	
PAINS	0 alert
Brenk	1 alert: isolated_alkene
Leadlikeness	No; 2 violations: Rotors>7, XLOGP3>3.5
Synthetic accessibility	3.18

Figure 4.11. SwissADME-Based Pharmaceutical Evaluation of EPA Molecule for Targets 5MY6, 7PCD, and 8U8X

Lapatinib is a tyrosine kinase inhibitor notable for its large and complex structure. Its molecular weight is 581.08 g/mol, which violates one of the Lipinski rules. Its structure contains 40 heavy atoms, 27 of which are aromatic, suggesting a relatively rigid and near-planar structure. Its TPSA value is high at 121.96 Å², consistent with low gastrointestinal absorption. Furthermore, it has very low water solubility (ESOL log S: -6.27), which poses a significant challenge for pharmaceutical formulation. Lapatinib is an inhibitor of the enzymes CYP1A2, CYP2C9, and CYP2C19, posing a risk of serious drug-drug interactions in clinical use. Lapatinib, which exhibits a balanced lipophilicity profile (consensus log Po/w: 4.09), satisfies the Egan and Muegge rules but shows significant violations of the Ghose and Veber rules. Its synthetic accessibility score is 3.96, indicating that its synthesis is quite difficult and costly. Its low bioavailability score (0.55) disadvantages this molecule, particularly regarding oral administration. While its structural features may allow it to bind with high affinity to the target receptor 7PCD, pharmacokinetic challenges and its CYP inhibition profile should be considered.

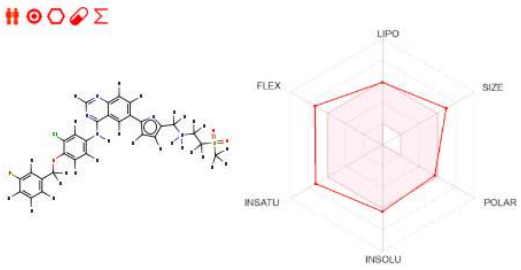

SMILES Fc1cccc(c1)COc1ccc(cc1Cl)Nc1ncnc2c1cc(cc2)c1ccc([nH]1)C[NH2+]CCS(=O)(=O)C

Physicochemical Properties	
Formula	C29H28ClFN5O3S+
Molecular weight	581.08 g/mol
Num. heavy atoms	40
Num. arom. heavy atoms	27
Fraction Csp3	0.17
Num. rotatable bonds	11
Num. H-bond acceptors	6
Num. H-bond donors	3
Molar Refractivity	157.23
TPSA	121.96 Å²
Lipophilicity	
Log $P_{o/w}$ (iLOGP)	3.85
Log $P_{o/w}$ (XLOGP3)	4.84
Log $P_{o/w}$ (WLOGP)	6.05
Log $P_{o/w}$ (MLOGP)	-0.24
Log $P_{o/w}$ (SILICOS-IT)	5.98
Consensus Log $P_{o/w}$	4.09

Water Solubility	
Log *S* (ESOL)	-6.27
Solubility	3.15e-04 mg/ml ; 5.43e-07 mol/l
Class	Poorly soluble
Log *S* (Ali)	-7.13
Solubility	4.26e-05 mg/ml ; 7.33e-08 mol/l
Class	Poorly soluble
Log *S* (SILICOS-IT)	-12.48
Solubility	1.91e-10 mg/ml ; 3.28e-13 mol/l
Class	Insoluble
Pharmacokinetics	
GI absorption	Low
BBB permeant	No
P-gp substrate	No
CYP1A2 inhibitor	Yes
CYP2C19 inhibitor	Yes
CYP2C9 inhibitor	Yes
CYP2D6 inhibitor	No
CYP3A4 inhibitor	No
Log K_p (skin permeation)	-6.41 cm/s
Druglikeness	
Lipinski	Yes; 1 violation: MW>500
Ghose	No; 3 violations: MW>480, WLOGP>5.6, MR>130
Veber	No; 1 violation: Rotors>10
Egan	No; 1 violation: WLOGP>5.88
Muegge	Yes
Bioavailability Score	0.55
Medicinal Chemistry	
PAINS	0 alert
Brenk	0 alert
Leadlikeness	No; 3 violations: MW>350, Rotors>7, XLOGP3>3.5
Synthetic accessibility	3.96

Figure 4.12. SwissADME-Based Pharmaceutical Evaluation of Lapatinib Molecule for Targets 5MY6, 7PCD, and 8U8X

In light of all these data summarized in Table 4.12, DHA stands out as the strongest candidate due to its pharmacokinetic suitability, high solubility, low toxicity, and ease of synthesis. While EPA is more lipophilic and structurally flexible, potentially binding to hydrophobic regions of the target protein, it is limited in terms of solubility and CYP interactions. While lapatinib, thanks to its unique structure, offers the potential to interact specifically with all three receptors, factors such as low solubility, high molecular complexity, and metabolic interactions make this compound more suitable for evaluation in advanced phases rather than early-stage drug discovery. In this context, among potential drug candidates to be developed targeting selected HER2 receptors, DHA can be considered the most advantageous molecule from both pharmaceutical and biopharmaceutical perspectives.

Table 4.5. Comparative Pharmaceutical Properties of DHA, EPA, and Lapatinib Molecules Based on SwissADME Data

Feature	**DHA**	**EPA**	**Lapatinib**
Molecular Weight	Low (90.10)	Medium (302.45)	High (581.08)
Water Solubility	Very high	Low	Very Low
GI Absorption	High	High	High
CYP Inhibitor	No	CYP2C9	CYP1A2, 2C9, 2C19
TPSA	64.94 Å²	37.30 Å²	121.96 Å²
Synthetic Accessibility	1.01 (very easy)	3.18	3.96 (hard)

4.2. Molecular Dynamics Simulation Results

Molecular dynamics (MD) simulations were employed to investigate the time-dependent conformational behavior of the ligand within the protein binding site. These simulations allowed the determination of the average potential energy profile by calculating the kinetic energy changes in the system and the derivation of the forces acting on each atom based on their energy values. This allowed for a more detailed analysis of the structural alignment of the ligand during interaction with the target protein.

To create an environment closer to physiological conditions, the motion of protein-ligand complexes was modeled in an environment containing water molecules. This enabled a more realistic simulation of biomolecular motions over time, and in particular, conformational changes in solution, hydrogen bonding, and solvation effects were observed in detail.

Furthermore, integrating appropriate parameters into polarizable force fields has been shown to be significantly more effective in more accurately modeling the dynamic structures of disordered or rapidly folding proteins. These findings are consistent with studies in the literature that emphasize the criticality of more precise representation of electrostatic interactions and polarization effects for the reliability of molecular dynamics simulations.

The parametric data used in all MD simulations—including the force field selection, system equilibration protocols, solvent model, and time steps—are presented in detail in Table 4.6.

Table 4.6. MD simulations parameters.

Temperature	298.15 K
Force Field	Charmm27
Solvent	TIP3P
Cubic Box Boundary	2.0 nm

Molecular dynamics simulations were performed under appropriate thermodynamic conditions. During this process, the system was first temperature controlled and thermostated using a 100-picosecond NVT equilibration under conditions of constant particle number (N), constant volume (V), and constant temperature (T). Density control was then achieved through a 100-picosecond NPT equilibration step, which included conditions of constant particle number (N), constant pressure (P), and constant temperature (T). The system was then pressure-equilibrated by selecting the appropriate barostat.

A detailed protocol for the codes used in the simulations is presented in Appendix I. For each protein-ligand complex, analyses including root mean square deviation (RMSD), root mean square fluctuation (RMSF), hydrogen bonding, and radius of gyration were carried out using the respective computational tools. 50-nanosecond MD simulations for all ligands and the reference drug were recorded using the Turkish National High Performance Computing Center (UHeM) infrastructure.

4.2.1. Protein-Only Molecular Dynamics Simulations

In simulation studies aimed at understanding ligand-protein interactions, analyzing the protein's native dynamics in aquatic environments is essential for accurately interpreting the structural changes induced by ligand binding. In this context, "blank" or "apo" simulations represent situations where the protein exists solely in aquatic environments and does not interact with any ligands. This allows for the evaluation of parameters such as the protein's conformational flexibility, structural stability, hydrogen bonding interactions with water, and overall compactness. These analyses serve as controls for the changes that will occur upon ligand binding and

allow for comparative evaluations (Hollingsworth & Dror, 2018). Several fundamental criteria are considered when selecting the protein to be used in the simulation. These include high-resolution and crystallographically verified structures (preferably <3.0 Å), well-defined binding sites, preference for native (mutation-free) isoforms, and suitability of the system for physiological conditions. Furthermore, in blank studies, it is important for the protein to be in its ligand-free (apo) form to model its native state. Such initial simulations help determine whether the system has reached equilibrium by analyzing time-dependent changes in parameters such as root mean square deviation (RMSD), gyration radius (Rg), or number of hydrogen bonds (Lemkul, 2019). Consequently, blank simulations are not only complementary to molecular dynamics studies but also a methodologically essential step for a robust assessment of ligand effects.

The RMSD curve presented in Figure 4.13 represents the conformational displacement of solvent (SOL) molecules during the simulation of the 8U8X protein in a water environment. In the first few nanoseconds of the simulation, the RMSD value increases rapidly, reaching approximately 0.25 nm, and stabilizes at this value, forming a stable plateau. This observation indicates that the water molecules are significantly displaced from their initial positions, but the system reaches equilibrium within a short time.

The high RMSD values of water molecules are expected because water is a dynamic solvent, constantly rearranging and interacting with hydrophilic/hydrophobic regions on the protein surface. In this context, the early rise observed in the graph can be associated with the adaptation of water molecules to the protein surface and the restructuring of the first solvation shell (Lemkul, 2019). The stabilization of the RMSD over time indicates that the solvent distribution in the system no longer exhibits significant time-dependent changes, meaning that the water environment has attained a dynamic but stable structure.

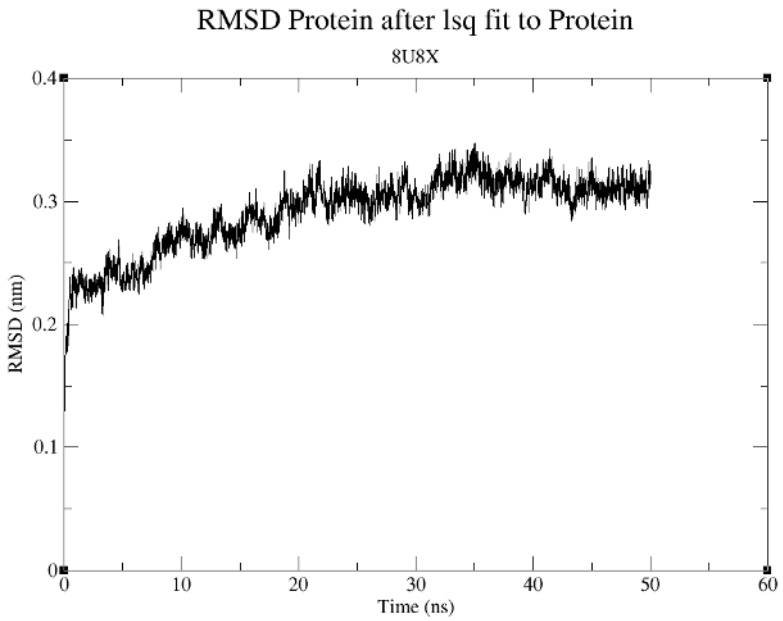

Figure 4.13. RMSD analysis results graph of 8U8X Protein-Only in MD simulation.

This result confirms that the system reached thermal equilibrium throughout the simulation and that the solvent structure remained stable. This stable distribution of water molecules is critical, particularly in protein-ligand studies, in terms of water displacements and potential displacement energies at ligand binding sites.

The RMSF values shown in Figure 4.14 represent the conformational mobility of the 8U8X protein per atom during the simulation in water. The horizontal axis represents the atomic number, and the vertical axis represents the deviation per atom (in nm). Average oscillations, generally observed in the range of 0.1–0.3 nm, indicate that the protein has overall structural stability. However, the significant RMSF increase observed, particularly in the range of 4500–5000 atoms, suggests high flexibility or disorder in these regions.

Such local mobility increases are generally associated with the loop regions, terminals, or flexible segments located on the surface of the protein. These regions can also potentially serve as ligand binding sites or allosteric interaction sites (Bahar et al., 2010). Conversely, the large regions with low RMSF values in the graph represent the more rigid and structurally stable portions of the protein. These regions generally correspond to the α-helix and β-sheet regions, which are secondary structural elements.

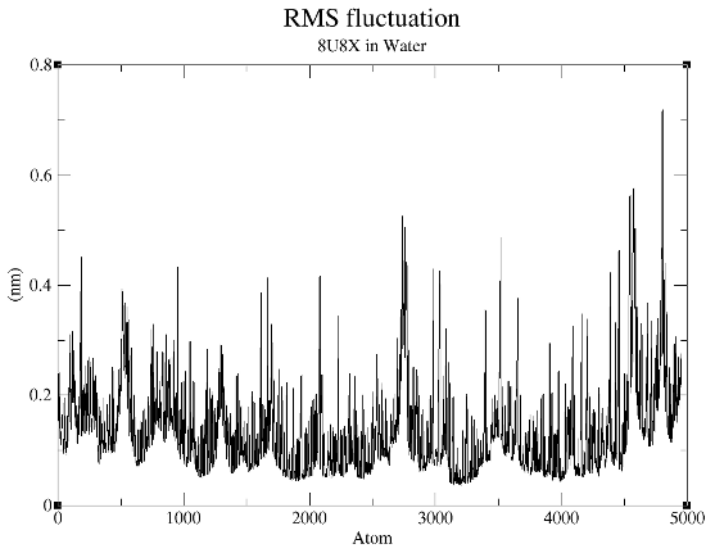

Figure 4.14. RMSF analysis results graph of 8U8X Protein-Only in MD simulation.

The results of RMSF analysis are valuable for both assessing the dynamic properties of the structure and predicting potential binding sites. Furthermore, changes in this RMSF distribution after ligand binding provide a fundamental reference point for comparative analyses to better understand the structural effects of binding.

Figure 4.15 shows that the gyration radius values fluctuated around 2.0 nm during a 50-ns simulation of the 8U8X protein in water. These measured values exhibit very low-amplitude oscillations over time, suggesting that the protein largely maintained its compact structure and remained structurally stable throughout the simulation.

The absence of a significant increase in the gyration radius indicates that the protein chain did not unwind (denaturate) and that its overall three-dimensional structure was preserved. This indicates that the system reached thermal equilibrium in the water environment and that the simulation conditions did not disrupt the protein's native conformation (Amadei et al., 1993). This finding also supports the notion that the apo form (ligand-free state) of the protein maintains its functional structure in water and provides a suitable starting model for potential ligand binding analyses.

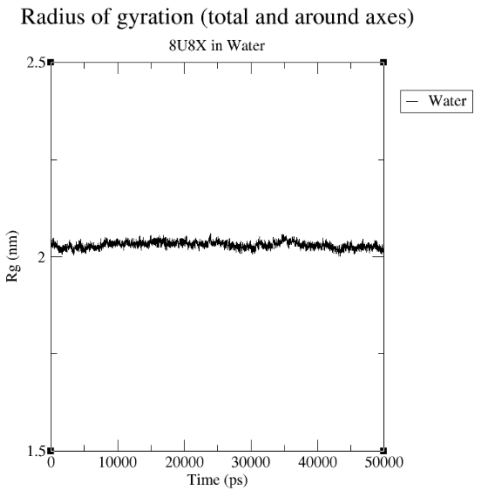

Figure 4.15. Radius of gyration analysis results graph of 8U8X Protein-Only in MD simulation.

The fact that the Rg analysis yields a stable curve profile suggests that there was no large-scale rearrangement in the protein's folding structure and that the system remained stable throughout the simulation. This data, when considered together with other structural parameters (e.g., RMSD and RMSF), provides important structural information about the dynamic equilibrium state of the protein solution.

The black curve in Figure 4.16 represents the number of active hydrogen bonds that meet classical hydrogen bonding criteria (based on donor-acceptor distance and angular constraints), while the red curve shows only potential hydrogen bond pairs that meet the distance criterion (≤ 0.35 nm). The number of bonds along the black curve, which ranges from approximately 650–750, indicates the protein's stable interaction level in a water environment. These values indicate that the protein is well hydrated in terms of solubility and interacts intensively with water (Lindorff-Larsen et al., 2010).

The red curve, on the other hand, reveals a higher number of atom pairs capable of potential hydrogen bonding and fluctuates over time. This indicates the presence of a dynamic hydrogen bond network in the system. Neither curve exhibits a significant upward or downward trend over time, indicating that the protein and its surrounding water molecules have reached equilibrium throughout the simulation and have created a stable binding environment.

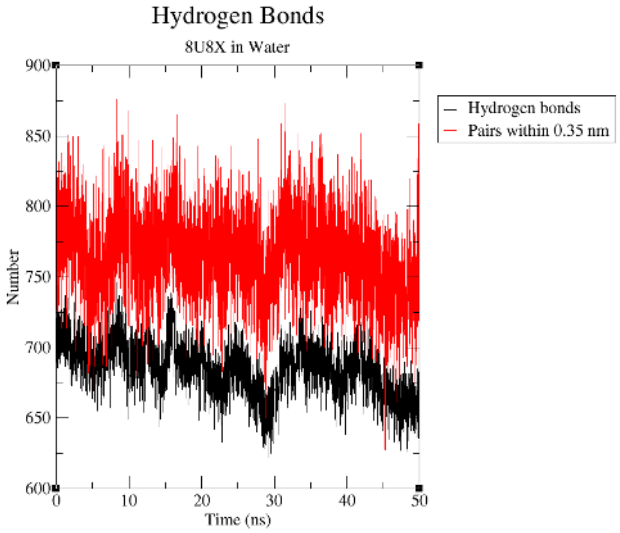

Figure 4.16. Hydrogen Bonds analysis results graph of 8U8X Protein-Only in MD simulation.

This analysis is particularly important in ligand binding studies. Because increases or decreases in hydrogen bonding resulting from ligand binding can be indicative of structural changes and binding efficiency, this blank simulation provides an important reference point for post-binding comparative analyses.

4.2.2. Molecular Dynamics Simulations with 5MY6

Initially, to assess structural variations throughout the molecular dynamics simulations, root mean square deviation (RMSD) values were computed and graphically represented as a function of simulation time. This analysis was performed for EPA, DHA, and Lapatinib complexed with the 5MY6 (HER2) receptor.

The RMSD (Root Mean Square Deviation) plot shown in Figure 4.17 presents the dynamic stability and conformational changes of three ligands—Lapatinib, EPA (Eicosapentaenoic acid), and DHA (Docosahexaenoic acid)—when bound to the 5MY6 receptor throughout a molecular dynamics (MD) simulation of 50 nanoseconds. RMSD is a crucial metric in MD studies, used to evaluate the structural deviation of a molecule over time, offering insight into the overall stability and binding behavior of ligand–receptor complexes.

According to the graph, DHA (green line) demonstrates the lowest and most stable RMSD values throughout the simulation, consistently ranging between

approximately 0.3 and 0.5 nm. This indicates minimal conformational fluctuation, suggesting that the DHA-5MY6 complex maintains a relatively stable binding pose over the simulation period. In contrast, EPA (red line) exhibits slightly higher RMSD values (~0.4–0.6 nm), with more fluctuations compared to DHA, implying moderate flexibility or weaker interactions with the receptor. Lapatinib (black line), a known synthetic anticancer agent, shows initial high RMSD fluctuations but stabilizes after around 10 ns, maintaining values around 0.4–0.5 nm for the remainder of the simulation. However, some noticeable instability is still observed, particularly between 20–40 ns, where RMSD temporarily drops and then increases again, suggesting potential repositioning within the binding site.

From a comparative standpoint, the results indicate that DHA binds to the 5MY6 receptor with greater conformational stability than both EPA and Lapatinib, despite being a natural compound. This might be attributed to DHA's flexible polyunsaturated chain allowing better accommodation in the binding pocket. The relatively stable interaction profile of DHA may highlight its potential as a promising bioactive compound in targeting 5MY6-related pathways.

In molecular dynamics literature, RMSD values below 0.3–0.4 nm are generally considered indicative of strong and stable binding. Therefore, the behavior of DHA closely aligns with this threshold, supporting its high binding stability.

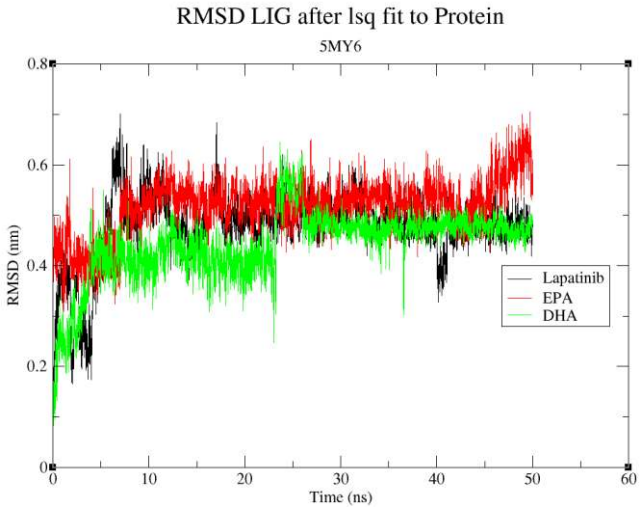

Figure 4.17. RMSD analysis results graph of 5MY6 receptor-bound ligands in MD simulation.

As a result, the EPA and Lapatinib ligands formed more stable complexes with the 5MY6 receptor, while DHA exhibited less stability at the binding site. These findings suggest that EPA and Lapatinib may be more advantageous in terms of binding affinity and interaction stability.

Figure 4.18 shows atomic-level root mean square fluctuation (RMSF) values calculated during molecular dynamics simulations for three different ligands (Lapatinib, EPA, and DHA) complexed with the 5MY6 (HER2) protein. RMSF is used to determine flexible or rigid regions along the protein chain by measuring the time-dependent deviations of each atom (usually Cα atoms) relative to their average position.

Across the simulation, all three ligands exhibit similar fluctuation patterns, with most regions maintaining low RMSF values below 0.2 nm, suggesting overall structural stability of the receptor. However, noticeable differences emerge in specific regions. Lapatinib (black line) shows the least fluctuation, indicating a more rigid and stable binding conformation with the receptor. EPA (red line) and DHA (green line), on the other hand, exhibit slightly higher fluctuations in several loop regions and terminal ends, particularly around atom indices ~2000–4000 and near the C-terminal region (around 8000). These regions correspond to more flexible parts of the protein, such as loops or terminal residues.

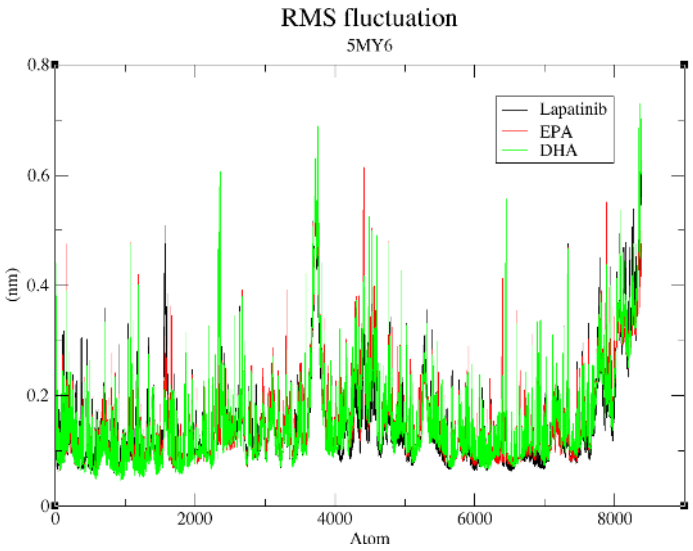

Figure 4.18. RMSF analysis results graph of 5MY6 receptor-bound ligands in MD simulation.

Overall, the RMSF analysis suggests that the 5MY6 receptor maintains a stable structure with all three ligands, but Lapatinib induces the least flexibility, which may indicate stronger or more stable binding. EPA and DHA induce moderate fluctuations, which could imply a slightly less rigid interaction with the receptor compared to Lapatinib.

Figure 4.19 presents the radius of gyration analysis for the 5MY6 receptor in complex with Lapatinib, EPA, and DHA over a 50 ns molecular dynamics simulation. R_g is an essential indicator of the protein's overall compactness and structural integrity. Throughout the simulation, all three ligand-bound systems exhibited relatively stable Rg values, ranging between approximately 2.8 and 3.1 nm, indicating that no significant conformational expansion or unfolding occurred. Among the ligands, the Lapatinib-bound complex displayed the lowest and most consistent Rg suggesting a tightly packed and stable structure. DHA also showed a stable trend with minor fluctuations, while EPA exhibited slightly higher variability, implying a more flexible or less compact interaction with the receptor. These results suggest that both Lapatinib and DHA contribute to maintaining the structural stability of the 5MY6 receptor, whereas EPA may induce slightly more dynamic conformational behavior.

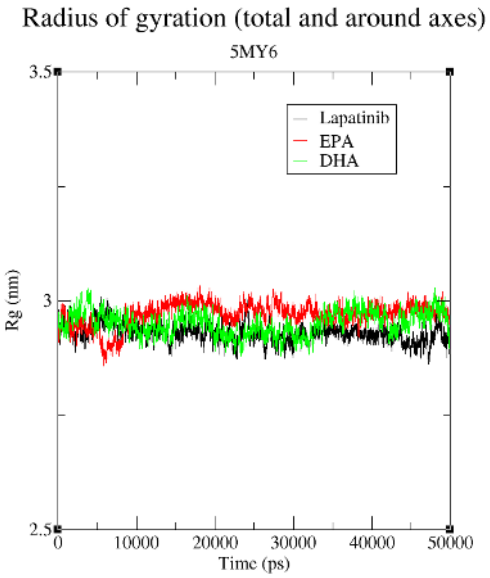

S

Figure 4.19. R_g analysis results graph of 5MY6 receptor-bound ligands in MD simulation.

Such stable Rg profiles indicate that the protein structure is thermodynamically stable and that the simulation was performed under appropriate conditions. They also provide important clues about the extent to which the protein maintains its structural stability in the presence of the ligand.

Hydrogen bonds are critical to the stability of protein-ligand interactions. The number of H-bonds provides direct information about the degree to which the ligand maintains its position at the binding site and the strength of its affinity for the protein. In this analysis, bonds were evaluated with a threshold of 0.35 nm.

As seen in Figure 4.20, Lapatinib formed an average of 2–5 hydrogen bonds over 50 ns, and at times, this number reached as high as 6–7. The high density and continuous formation of bonds demonstrate Lapatinib's strong affinity for the binding site and the high stability of the complex. This confirms that Lapatinib, as a reference drug, binds tightly and consistently to the target protein.

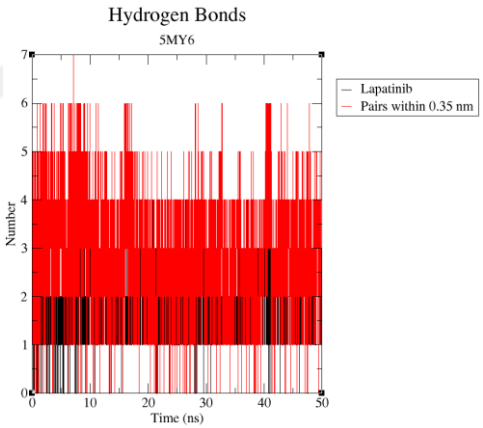

Figure 4.20. Hydrogen bonding analysis results graph of 5MY6 receptor-bound Laptinib in MD simulation.

An examination of Figure 4.21 reveals that the EPA molecule can form a maximum of 5 hydrogen bonds during the first 10 ns, but as the simulation progresses, this number generally fluctuates between 0 and 2. This suggests that EPA initially occupied a stable position in the binding site, but may have lost this position over time, moved away from the protein, or altered its binding geometry. The lack of continuity

of the hydrogen bonds suggests that this ligand's binding stability to the protein is limited.

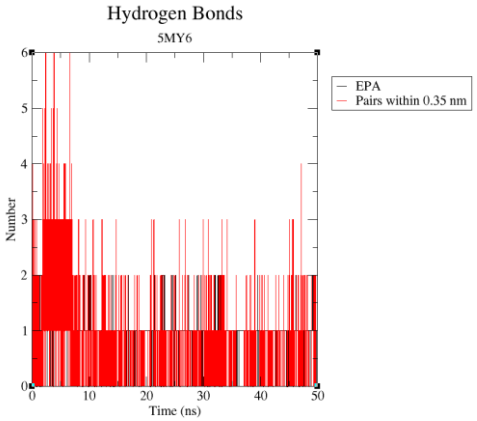

Figure 4.21. Hydrogen bonding analysis results graph of 5MY6 receptor-bound EPA in MD simulation.

Figure 4.22 shows the hydrogen bonding analysis of the 5MY6-DHA complex during a 50 ns MD simulation. The number of hydrogen bonds fluctuates between 0 and 4, with 1–2 bonds being the most frequent, especially in the first 30 ns. This indicates that DHA forms moderately stable interactions with the 5MY6 receptor, with occasional transient bonding. The presence of consistent hydrogen bonds suggests a flexible yet stable binding throughout the simulation.

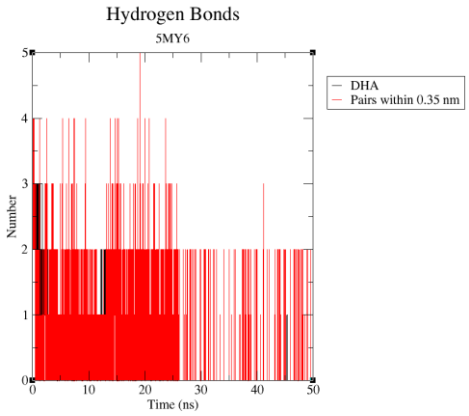

Figure 4.22. Hydrogen bonding analysis results graph of 5MY6 receptor-bound DHA in MD simulation.

The comparison of hydrogen bonding patterns among Lapatinib, EPA, and DHA bound to the 5MY6 receptor shows distinct interaction profiles. Lapatinib forms the highest and most stable number of hydrogen bonds (up to 6), indicating strong and

consistent binding. EPA shows moderate bonding, mostly 1–3 bonds, which decrease over time. DHA forms the fewest and least stable hydrogen bonds, typically 1–2, declining after 25 ns. Overall, Lapatinib demonstrates the strongest hydrogen bond stability, followed by EPA, while DHA shows the weakest interaction with the receptor.

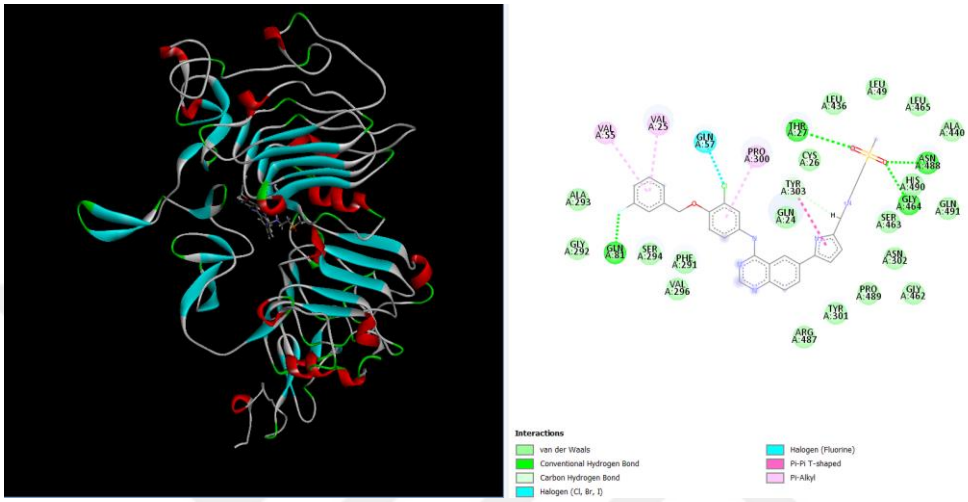

Figure 4.23. Discovery Studio 3D and 2D Ligand-Protein MDS Diagram Lapatinib interactions with the 5MY6 receptor

Figure 4.23 illustrates the 2D ligand–protein interaction diagram of Lapatinib in complex with the 5MY6 receptor, generated via Discovery Studio, revealing a diverse and well-distributed interaction profile within the receptor binding site. The diagram shows several key hydrophobic interactions, including π-alkyl and π–π T-shaped interactions (highlighted in pink and violet), formed with residues such as VAL A:25, PRO A:300, TYR A:303, and GLN A:297, which contribute significantly to the stabilization of the ligand within a largely nonpolar pocket. Conventional hydrogen bonds are observed between Lapatinib and residues such as GLN A:494, TYR A:303, and ASN A:488, indicating polar anchoring points that enhance binding specificity. Furthermore, carbon hydrogen bonds and van der Waals contacts with residues like ALA A:293, SER A:294, VAL A:296, and GLY A:292 suggest additional stabilization through close-range, non-directional interactions. A notable halogen bond involving the fluorine atom of Lapatinib is formed with THR A:488, underlining the contribution of halogen-mediated interactions to ligand affinity. The overall binding environment is composed of both polar and nonpolar residues, supporting a multifaceted binding

mechanism that integrates hydrogen bonding, hydrophobic forces, and halogen bonding. This interaction network underscores Lapatinib's ability to adopt a conformationally favorable and pharmacodynamically relevant pose within the 5MY6 receptor, potentially contributing to its therapeutic efficacy.

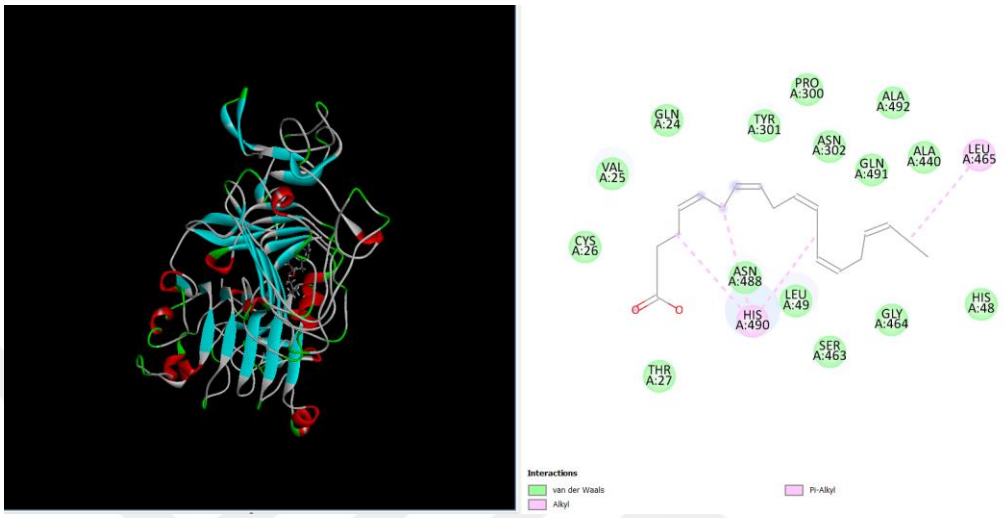

Figure 4.24. Discovery Studio 3D and 2D Ligand-Protein MDS Diagram EPA interactions with the 5MY6 receptor

Figure 4.24 depicts the 2D ligand–protein interaction diagram of eicosapentaenoic acid (EPA) with the 5MY6 receptor, offering insight into the molecular basis of its binding profile as visualized through Discovery Studio. The interaction map reveals that EPA forms several key hydrophobic (π-alkyl) interactions with residues such as LEU A:465 and HIS A:490, suggesting that the ligand is accommodated within a hydrophobic sub-pocket of the receptor. Additionally, van der Waals interactions are formed with surrounding residues including VAL A:25, CYS A:26, THR A:27, TYR A:301, SER A:463, and GLY A:464, which contribute to non-specific but stabilizing contacts that reinforce ligand positioning. A notable interaction is the involvement of ASN A:488, which appears to form multiple weak contacts with the ligand's polar head region, possibly acting as an anchoring site. The interaction network, while less extensive than that observed with bulkier ligands like Lapatinib, indicates a moderate but favorable binding of EPA, predominantly stabilized by hydrophobic forces and weak polar contacts. This profile aligns with the typical behavior of fatty acid-based molecules, which rely more on hydrophobic compatibility

than directional polar interactions, and supports EPA's potential modulatory role at this receptor site.

Figure 4.25. Discovery Studio 3D and 2D Ligand-Protein MDS Diagram DHA interactions with the 5MY6 receptor

Figure 4.25 presents the 2D ligand–protein interaction diagram of docosahexaenoic acid (DHA) with the 5MY6 receptor, offering a structural perspective on its molecular binding characteristics as visualized through Discovery Studio. The interaction network is predominantly stabilized by hydrophobic interactions, including alkyl and π-alkyl contacts (highlighted in pink) with residues such as VAL A:25, LEU A:49, ALA A:440, LEU A:465, and LEU A:436, indicating that DHA resides within a nonpolar pocket of the receptor. These interactions play a key role in anchoring the long aliphatic chain of DHA. In addition, conventional hydrogen bonding is observed between the carboxyl group of DHA and HIS A:490, providing a crucial polar interaction that enhances the ligand's binding specificity. Surrounding residues such as CYS A:26, PRO A:300, ASN A:488, and GLY A:464 are involved in van der Waals interactions, offering supplementary stabilization through non-directional, close-range forces. The interaction profile indicates that DHA, like EPA, relies heavily on hydrophobic compatibility with the binding site, but the presence of a stabilizing hydrogen bond suggests a slightly enhanced affinity. Overall, the binding mode of DHA within the 5MY6 receptor supports its biological

relevance and potential modulatory function through a combination of long-chain hydrophobic anchoring and limited polar interaction.

4.2.3. Molecular Dynamics Simulations with 7PCD

First, the structural conformational changes of the 7PCD receptor, EPA, DHA ligands, and the reference drug Lapatinib were examined during the simulation period by calculating RMSD (root mean square deviation) values. This analysis was performed to assess how the molecules changed over time compared to their initial structure and whether they gained stability.

Figure 4.26 compares the RMSD (root mean square deviation) values of the ligands (Lapatinib, EPA, and DHA) bound to the 7PCD receptor over time. RMSD is a frequently used parameter in molecular dynamics simulations to assess the structural stability and conformational changes of a ligand after binding to the receptor (Karplus and McCammon, 2002).

The RMSD analysis of 7PCD receptor-bound ligands during the molecular dynamics (MD) simulation reveals differences in the structural stability of the ligand-receptor complexes. Lapatinib exhibits the lowest and most stable RMSD values throughout the 50 ns simulation, indicating minimal deviation and high conformational stability when bound to the 7PCD receptor. EPA shows moderate fluctuations with slightly higher RMSD values, suggesting less stability compared to Lapatinib. DHA demonstrates the highest and most variable RMSD values, peaking around 0.7 nm, which indicates greater structural deviations and weaker binding stability. These results suggest that Lapatinib maintains the most stable interaction with the 7PCD receptor, followed by EPA, while DHA exhibits the least stable binding conformation.

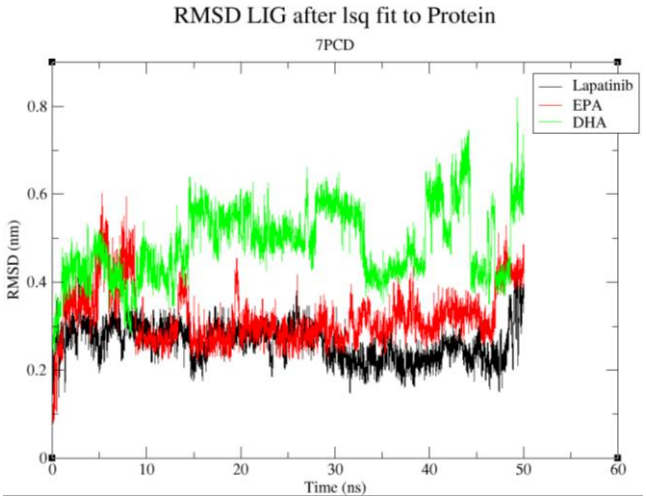

Figure 4.26. RMSD analysis results graph of 7PCD receptor-bound ligands in MD simulation.

These results reveal differences in the binding stability and conformational fit of the ligands. DHA appears to provide a more conformable and stable interaction with the receptor, while EPA exhibits a more flexible and potentially less stable binding state. Lapatinib, as the reference drug, provides moderate stability.

Figure 4.27 shows the atomic-based RMSF (Root Mean Square Fluctuation) values of three different ligands (Lapatinib, EPA, and DHA) bound to the 7PCD receptor. RMSF is an important parameter used in molecular dynamics simulations to evaluate the time-dependent mobility and flexibility of individual atoms or amino acids (Kumar et al., 2015).

Lapatinib (black line) shows moderate fluctuations throughout, with a few sharp peaks, particularly at terminal and loop regions, suggesting some localized flexibility. EPA (red) and DHA (green) both display slightly higher fluctuations in certain regions compared to Lapatinib, although the differences are not drastic. This may indicate that EPA and DHA induce slightly more flexibility in the receptor structure, particularly in loop or surface-exposed areas. Importantly, all ligands maintain RMSF values mostly below 0.4 nm, suggesting no major structural destabilization.

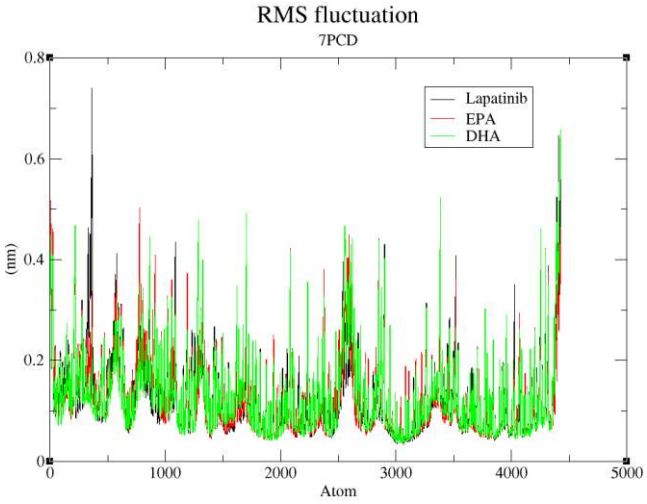

Figure 4.27. RMSF analysis results graph of 7PCD receptor-bound ligands in MD simulation.

It has been reported in the literature that low RMSF values are generally associated with structural stability and tight binding (Amadei et al., 1993). The RMSF analysis suggests that binding of Lapatinib results in slightly lower atomic fluctuations compared to EPA and DHA, implying a more rigid and potentially more stable complex with the 7PCD receptor.

Figure 4.28 illustrates the Radius of Gyration (Rg) analysis of 7PCD receptor-bound ligands—Lapatinib, EPA, and DHA—during molecular dynamics simulation. The Rg values for all three complexes remain relatively stable throughout the 50 ns simulation, ranging between approximately 1.8 and 2.0 nm, indicating consistent compactness and structural integrity. Lapatinib (black line) exhibits a slightly higher Rg initially, suggesting a marginally less compact structure compared to EPA (red) and DHA (green), which show nearly overlapping and stable Rg profiles. Overall, these results imply that all ligands maintain a stable binding conformation with the receptor, with no significant unfolding or structural expansion observed, underscoring the structural stability of the receptor-ligand complexes during the simulation.

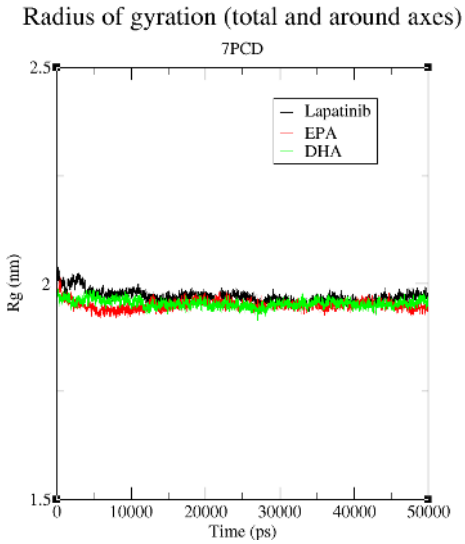

Figure 4.28. R_g analysis results graph of 7PCD receptor-bound ligands in MD simulation.

The stability of the radius of gyration values indicates that the structural integrity of the ligand-receptor complex was maintained throughout the dynamic simulation period. In this context, it can be argued that the complexes formed by EPA and DHA with the 7PCD receptor are more stable and compact than those of Lapatinib.

Hydrogen bond analyses show the change in the number of hydrogen bonds formed by the Lapatinib, EPA, and DHA ligands interacting with the 7PCD receptor over time. Hydrogen bonds are critical for the stability and specificity of ligand-receptor interactions.

Figure 4.29 examines the number of hydrogen bonds formed by the Lapatinib ligand with the 7PCD receptor. The graph shows that Lapatinib forms an average of 2-4 hydrogen bonds within the complex, and these bonds are relatively stable throughout the simulation period. This suggests that Lapatinib forms strong and sustained interactions with the receptor.

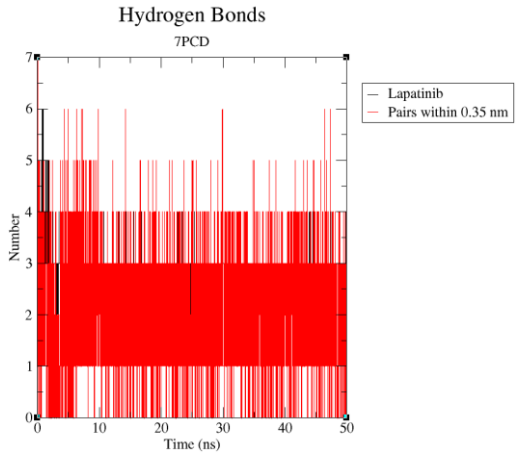

Figure 4.29. Hydrogen bonding analysis results graph of 7PCD receptor-bound Lapatinib in MD simulation.

Figure 4.30 shows the evolution of hydrogen bonds over time for the EPA ligand. EPA typically forms 1-2 hydrogen bonds, and the number of these bonds fluctuates more. This may indicate that EPA exhibits more flexible or variable interactions during binding. The lower number of hydrogen bonds compared to Lapatinib suggests that the binding may be relatively less stable.

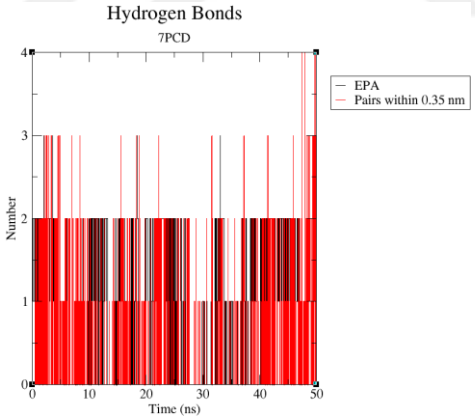

Figure 4.30. Hydrogen bonding analysis results graph of 7PCD receptor-bound EPA in MD simulation.

Figure 4.31 presents the hydrogen bonding analysis of the 7PCD receptor bound with DHA during molecular dynamics simulation. The graph shows that the number of hydrogen bonds fluctuates between 0 and 3 throughout the 50 ns simulation period, indicating intermittent but persistent interactions. These hydrogen bonds contribute to the stabilization of the DHA ligand within the binding site. The relatively

consistent formation of hydrogen bonds suggests that DHA maintains stable contacts with the receptor, which is critical for effective binding affinity and complex stability. Overall, the hydrogen bonding pattern supports the potential of DHA as a stable ligand for the 7PCD receptor in the simulated environment.

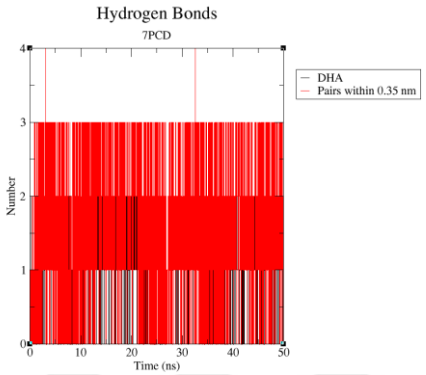

Figure 4.31. Hydrogen bonding analysis results graph of 7PCD receptor-bound DHA in MD simulation.

Overall, hydrogen bond analyses reveal that lapatinib binds stably and continuously with the receptor, while EPA forms relatively fewer hydrogen bonds and is more flexible in binding, while DHA exhibits strong but variable interactions with a high number of hydrogen bonds. These findings provide important insights into the binding affinities and dynamic behaviors of the ligands. Supported by previous RMSD, RMSF, and radius of gyration (Rg) analyses, they enhance the understanding of the molecular interaction profiles and stability of the ligand-receptor complexes.

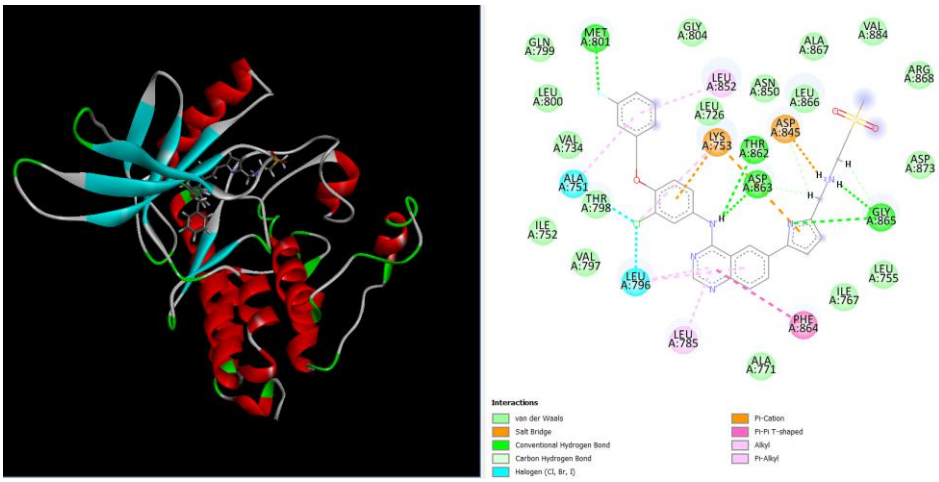

Figure 4.32. Discovery Studio 3D and 2D Ligand-Protein MDS Diagram Lapatinib interactions with the 7PCD receptor

Figure 4.32 illustrates the 2D ligand–protein interaction diagram of Lapatinib bound to the 7PCD receptor, as visualized through Discovery Studio, revealing a complex and well-coordinated binding pattern. The ligand exhibits multiple interaction types that contribute to its high binding affinity and specificity. Notably, π-cation interactions are formed with LYS A:753, while conventional hydrogen bonds are established with ASP A:863 and GLY A:865, indicating strong polar interactions critical for anchoring the ligand within the active site. Additional carbon hydrogen bonds are observed with LEU A:796, ALA A:751, and THR A:798, further stabilizing the ligand through directional but weaker forces. A halogen bond involving the fluorine atom of Lapatinib interacts with GLY A:865, enhancing the ligand's electrostatic complementarity with the receptor. Hydrophobic contacts are also prominent, including π–π T-shaped interactions with PHE A:864, and π-alkyl/alkyl interactions with residues such as LEU A:785, ILE A:767, VAL A:797, and LEU A:771, indicating the presence of a nonpolar pocket that accommodates the aromatic moieties of the ligand. Collectively, this extensive interaction network—comprising polar, hydrophobic, and halogen-mediated contacts—demonstrates a strong and specific binding mode for Lapatinib within the 7PCD receptor, supporting its role as a potent kinase inhibitor and highlighting the structural basis of its bioactivity.

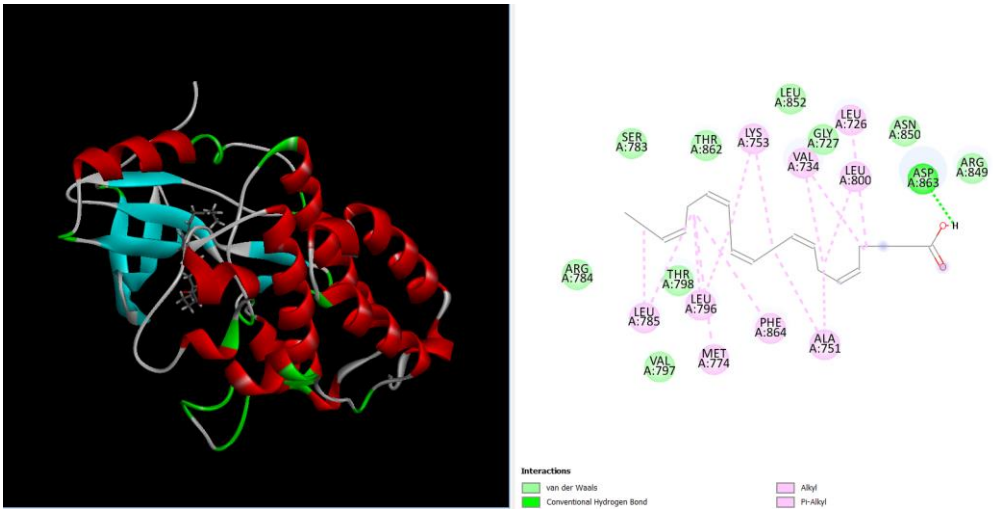

Figure 4.33. Discovery Studio 3D and 2D Ligand-Protein MDS Diagram EPA interactions with the 7PCD receptor

Figure 4.33 presents the Discovery Studio 3D and 2D ligand–protein interaction diagrams illustrating the binding mode of EPA with the 7PCD receptor. In the 2D interaction diagram, EPA forms a specific conventional hydrogen bond (green line) with the ASP A:863 residue via its carboxyl group, indicating a key polar interaction anchoring the ligand within the binding site. Additionally, several hydrophobic interactions, including alkyl and pi-alkyl contacts, are observed with residues such as LEU A:796, PHE A:864, ALA A:751, LEU A:785, VAL A:797, LEU A:800, and MET A:774, which facilitate the stable positioning of EPA within the receptor's hydrophobic pocket. These interactions play a crucial role in enhancing ligand affinity by complementing the shape and hydrophobic nature of the binding cavity. Furthermore, pi-alkyl interactions with residues like LYS A:753, LEU A:726, and THR A:798 contribute to the conformational accommodation of the ligand. Overall, these findings suggest that EPA exhibits a moderately stable and multi-faceted binding profile with the 7PCD receptor, engaging both polar and nonpolar residues to maintain structural complementarity.

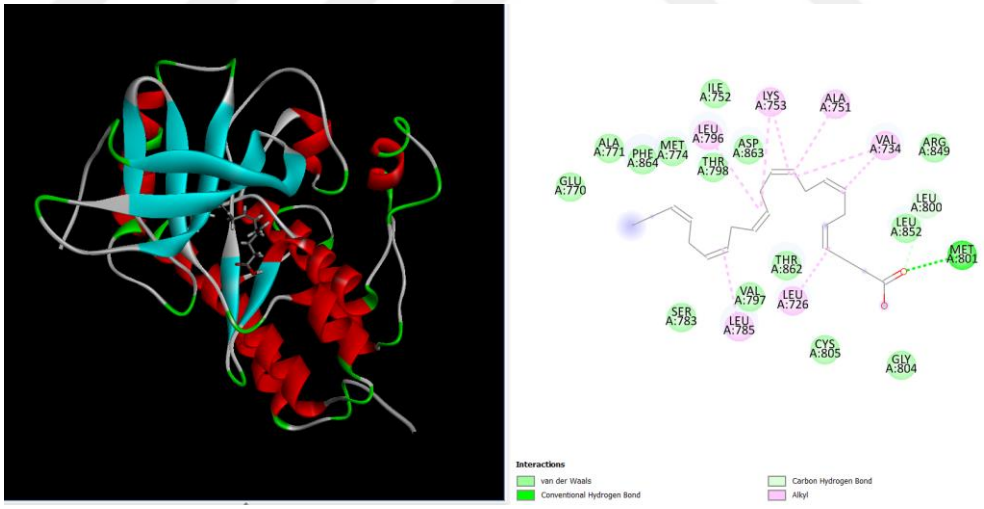

Figure 4.34. Discovery Studio 3D and 2D Ligand-Protein MDS Diagram DHA interactions with the 7PCD receptor

Figure 4.34 shows the Discovery Studio 3D and 2D ligand-protein interaction diagrams depicting the binding interactions of DHA with the 7PCD receptor.

In the 2D interaction diagram, DHA forms a conventional hydrogen bond (green line) with the MET A:801 residue, indicating a strong polar interaction between the ligand

and receptor that helps stabilize the complex. Additionally, several hydrophobic interactions are observed, mainly in the form of alkyl interactions (pink lines) with residues such as LEU A:796, LEU A:785, LEU A:726, VAL A:734, LYS A:753, ALA A:751, and ARG A:849. These hydrophobic contacts suggest that DHA is well accommodated within a largely nonpolar binding pocket of the receptor, contributing to the overall binding affinity. There are also van der Waals interactions (light green circles) with various surrounding residues, which further enhance ligand binding by complementing the shape and surface of the receptor cavity. Overall, DHA exhibits a combination of specific polar interactions and extensive hydrophobic contacts, indicating a stable and favorable binding mode with the 7PCD receptor.

4.2.4. Molecular Dynamics Simulations with 8U8X

First, RMSD (root mean square deviation) values were calculated to examine the conformational changes of the EPA and DHA ligands and the reference drug Lapatinib interacting with the 8U8X receptor during the simulation period, and how they changed and stabilized compared to their initial structure was analyzed.

Figure 4.35 presents the RMSD analysis of three ligands bound to the 8U8X receptor over a 50-nanosecond molecular dynamics simulation. RMSD measures the average deviation in the ligand's atomic positions relative to its initial conformation, serving as an indicator of ligand stability and binding consistency during the simulation.

Lapatinib exhibits the lowest RMSD values throughout the simulation, generally remaining below 0.25 nm. This suggests that Lapatinib maintains a highly stable interaction with the 8U8X receptor, with minimal conformational changes or displacement. Such stability is often correlated with strong binding affinity and favorable ligand-receptor interactions.

EPA shows a moderate RMSD profile, with values starting low but increasing to around 0.4–0.5 nm after the initial 10–15 ns. This indicates that EPA undergoes some structural adjustments or flexibility when binding, but overall, it remains relatively stable in the receptor's binding pocket.

DHA demonstrates the highest RMSD values, especially after 30 ns, reaching above 0.6 nm. This greater fluctuation implies that DHA is less stable within the binding site, possibly adopting multiple conformations or experiencing weaker interactions with the receptor. Such instability can suggest lower binding affinity or less effective inhibition potential compared to Lapatinib and EPA.

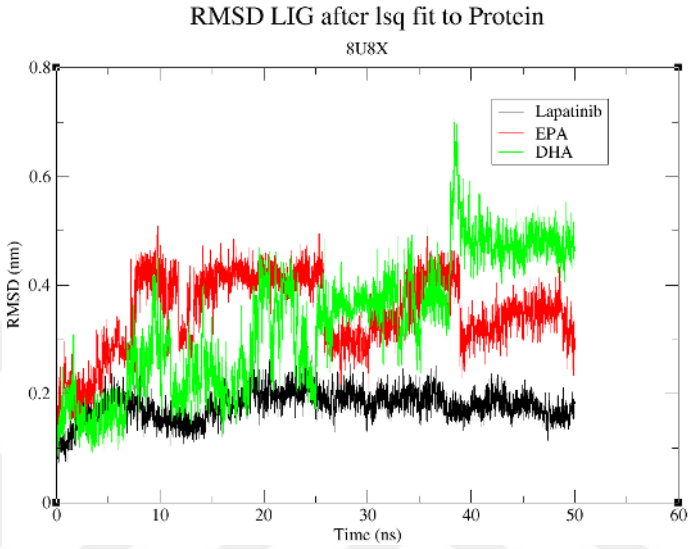

Figure 4.35. RMSD analysis results graph of 8U8X receptor-bound ligands in MD simulation.

In summary, this RMSD analysis highlights that Lapatinib forms the most stable complex with the 8U8X receptor, followed by EPA with moderate stability, while DHA displays significant conformational fluctuations. These findings provide valuable insights into the dynamic behavior of these ligands and can guide future optimization efforts for drug design targeting this receptor.

Figure 4.36 shows the RMSF (Root Mean Square Fluctuation) analysis of ligands Lapatinib, EPA, and DHA bound to the 8U8X receptor during molecular dynamics simulation. RMSF measures the flexibility or mobility of individual atoms in the ligand over time, reflecting local fluctuations rather than overall conformational changes.

The plot indicates that all three ligands display similar fluctuation patterns, with multiple peaks and troughs corresponding to flexible and rigid regions within

their structures. Most atoms exhibit low to moderate fluctuations, generally below 0.3 nm, suggesting relatively stable binding and limited local flexibility.
However, there are some distinct peaks where EPA and DHA show slightly higher fluctuations than Lapatinib, especially near atom indices around 1000, 3000, and towards the end of the sequence (~4500 atoms). These higher fluctuations imply increased local flexibility or movement in these ligand regions, which may affect binding stability or interaction strength.

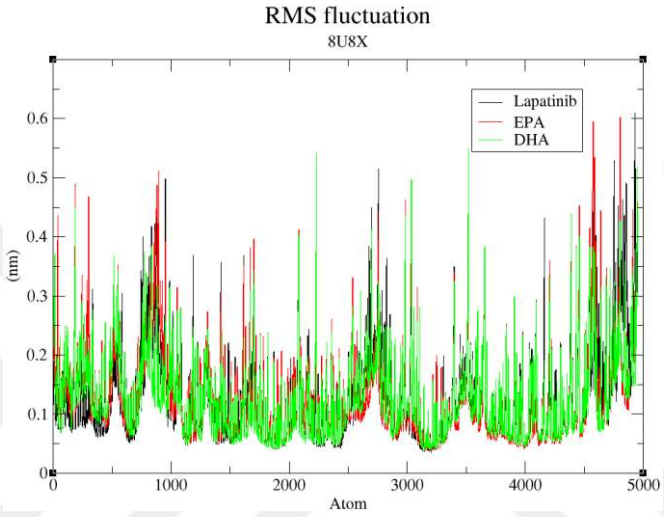

Figure 4.36. RMSF analysis results graph of 8U8X receptor-bound ligands in MD simulation.

Overall, Lapatinib demonstrates slightly lower atomic fluctuations compared to EPA and DHA, indicating a more rigid and stable ligand conformation within the 8U8X receptor binding site. The RMSF analysis complements the RMSD results, confirming that Lapatinib maintains stronger and more consistent interactions, while EPA and DHA show more dynamic behavior at the atomic level.

The Rg plot compares the radial deviations, or "gyration radius (Rg)," of Lapatinib, EPA, and DHA ligands complexed with the 8U8X receptor during molecular dynamics simulations. The radius of gyration is a parameter that quantifies the spatial distribution of a protein's atoms around its center of mass and serves as a key indicator for evaluating the overall compactness of the protein structure. The stability of the Rg value over time indicates that the system remains structurally stable and the protein maintains its compactness.

Figure 4.37 shows the radius of gyration (Rg) analysis of ligands Lapatinib, EPA, and DHA bound to the 8U8X receptor during the molecular dynamics simulation. The radius of gyration provides information about the overall compactness and structural stability of the ligand-receptor complex by measuring the distribution of atoms around the center of mass.

In this graph, all three ligands exhibit very stable Rg values around approximately 2.0 nm throughout the 50 ns simulation, indicating that the ligands maintain their overall compactness without significant structural expansion or contraction. This suggests stable folding and consistent ligand conformations within the binding pocket.

Among the ligands, EPA shows slightly lower Rg values compared to Lapatinib and DHA, suggesting a marginally more compact structure during the simulation. However, the differences between the ligands are minimal, and all three demonstrate stable behavior without large fluctuations or deviations.

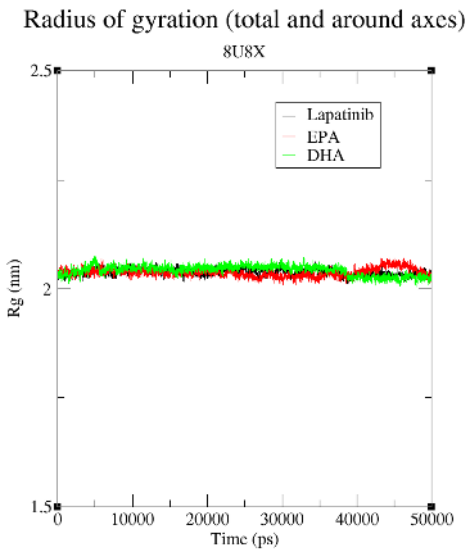

Figure 4.37. R_g analysis results graph of 8U8X receptor-bound ligands in MD simulation.

Overall, the Rg analysis confirms that the ligands maintain their structural integrity and do not undergo major conformational changes during the simulation,

supporting the results of RMSD and RMSF analyses that showed ligand stability within the 8U8X receptor binding site.

The hydrogen bond graphs show the number of hydrogen bonds formed during the complexation of the 8U8X protein receptor with the Lapatinib, EPA, and DHA ligands, and their change over time. Hydrogen bonds are a key determinant of protein-ligand interactions and an important indicator of bond stability and affinity.

Figure 4.38 examines the hydrogen bonds in the complex formed by the Lapatinib ligand with the 8U8X receptor. The observed number of bonds generally ranges from 1 to 2, and the bonds are quite stable throughout the simulation period. The notably low yet stable number of hydrogen bonds formed in the lapatinib complex indicates that these interactions are likely to be highly specific and strong, thereby contributing to the stabilization of the binding site in an optimized conformation. This is consistent with the known potent targeting effect of lapatinib.

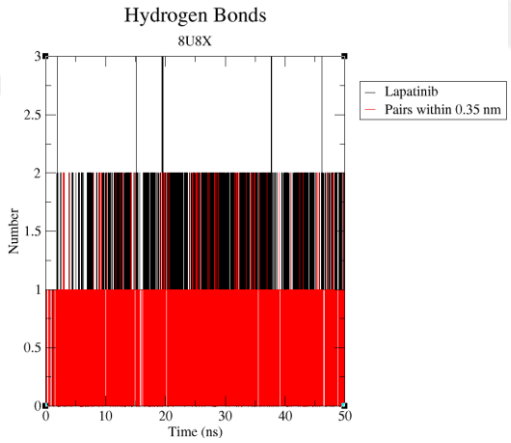

Figure 4.38. Hydrogen bonding analysis results graph of 8U8X receptor-bound Lapatinib in MD simulation.

Figure 4.39 shows the hydrogen bond profile of the EPA ligand. It is observed that the number of bonds between EPA and the receptor fluctuates significantly over time, sometimes reaching as high as 6 to 8. This suggests that EPA exhibits a flexible binding pattern on the receptor surface, capable of entering different conformations and establishing hydrogen bonds at different locations. However, this also suggests that the system may be less stable in terms of binding, and the bonds may be transient.

In other words, EPA exhibits a structurally dynamic interaction pattern, forming more bonds but with shorter durations.

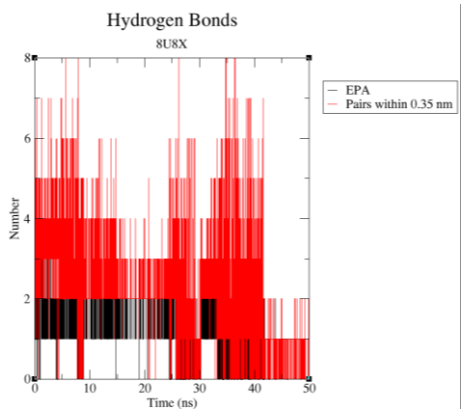

Figure 4.39. Hydrogen bonding analysis results graph of 8U8X receptor-bound EPA in MD simulation.

Figure 4.40 illustrates the hydrogen bonding analysis of DHA bound to the 8U8X receptor during the molecular dynamics simulation. Hydrogen bonds are crucial for stabilizing ligand-receptor interactions, and their number over time indicates the strength and consistency of binding.

The graph shows that DHA forms between 0 to 3 hydrogen bonds consistently throughout the 50 ns simulation, with most of the time maintaining 1 to 2 hydrogen bonds. This suggests relatively stable and persistent interactions between DHA and the receptor. Occasional spikes up to 6 hydrogen bonds indicate transient but strong bonding events that may enhance binding affinity at specific times.

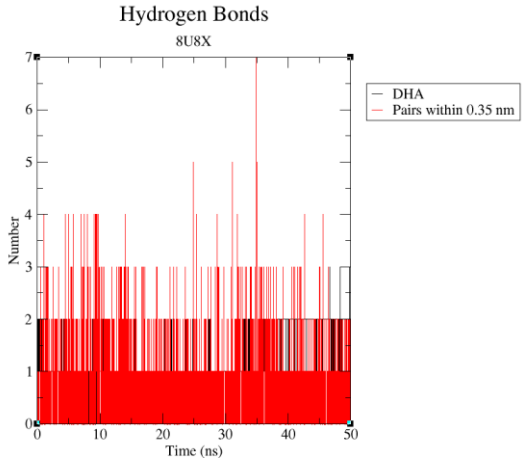

Figure 4.40. Hydrogen bonding analysis results graph of 8U8X receptor-bound DHA in MD simulation.

Overall, the presence of multiple, stable hydrogen bonds over the simulation indicates that DHA maintains good binding interactions with the 8U8X receptor, supporting its potential effectiveness as a ligand in this system.

The comparison of hydrogen bonding interactions between the 8U8X receptor and the ligands Lapatinib, EPA, and DHA reveals distinct binding behaviors. Lapatinib exhibits the most stable interaction profile, consistently maintaining 1 to 2 hydrogen bonds throughout the 50 ns simulation with minimal fluctuations. This indicates a strong and steady binding affinity to the receptor. In contrast, EPA shows the highest variability in hydrogen bonding, with bond numbers frequently ranging from 0 to 7. Such fluctuation suggests a more dynamic but potentially less stable interaction with the receptor. DHA displays an intermediate profile, generally forming 1 to 3 hydrogen bonds, with moderate fluctuations. This implies a balance between stability and interaction flexibility. Overall, Lapatinib demonstrates the most stable binding, while EPA exhibits greater flexibility in hydrogen bonding, and DHA presents a moderate and balanced interaction pattern with the 8U8X receptor.

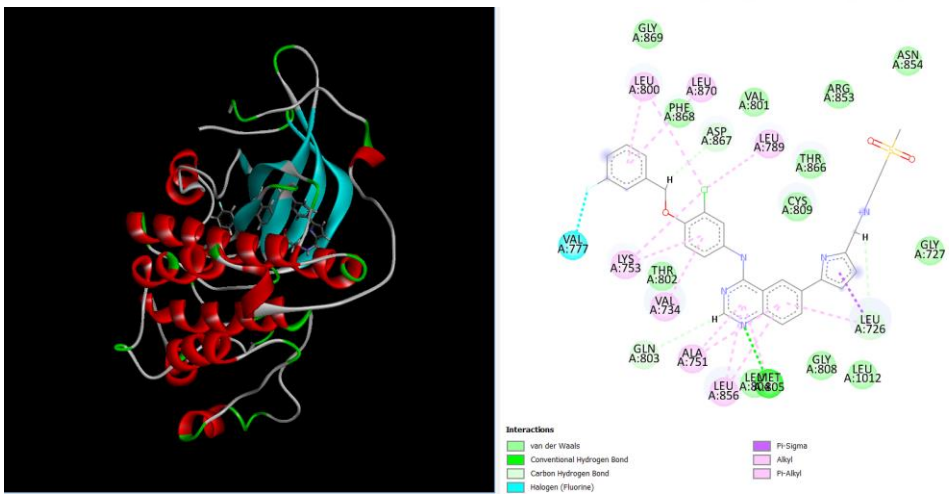

Figure 4.41. Discovery Studio 3D and 2D Ligand-Protein MDS Diagram Lapatinib interactions with the 8U8X receptor

The 2D interaction diagram in Figure 4.41 presents the molecular interactions between Lapatinib and the 8U8X receptor, providing detailed insight into the binding characteristics of this tyrosine kinase inhibitor. The ligand engages in a rich network

of interactions, prominently featuring alkyl and π-alkyl interactions (highlighted in pink) with residues such as LEU A:726, LEU A:801, LEU A:856, and MET A:805, indicating that the ligand is deeply embedded within a hydrophobic binding pocket. Additionally, π-π stacking and π-sigma interactions are observed, notably with PHE A:868 and VAL A:777, contributing to the stability and orientation of the aromatic rings of Lapatinib. Importantly, hydrogen bonding interactions are established with residues like ASP A:867 and THR A:802, which enhance binding specificity and affinity through directional polar contacts. The ligand also forms a carbon hydrogen bond with ALA A:751 and a halogen bond with VAL A:777, due to the presence of a fluorine substituent, which further supports its binding strength. Residues such as GLY A:808, GLN A:803, and ASN A:854 are involved in van der Waals interactions, helping to stabilize the ligand in the receptor's active site. Overall, the interaction profile of Lapatinib within 8U8X reveals a well-optimized binding conformation, where hydrophobic interactions dominate but are complemented by specific polar contacts, consistent with its known efficacy as a targeted anti-cancer agent.

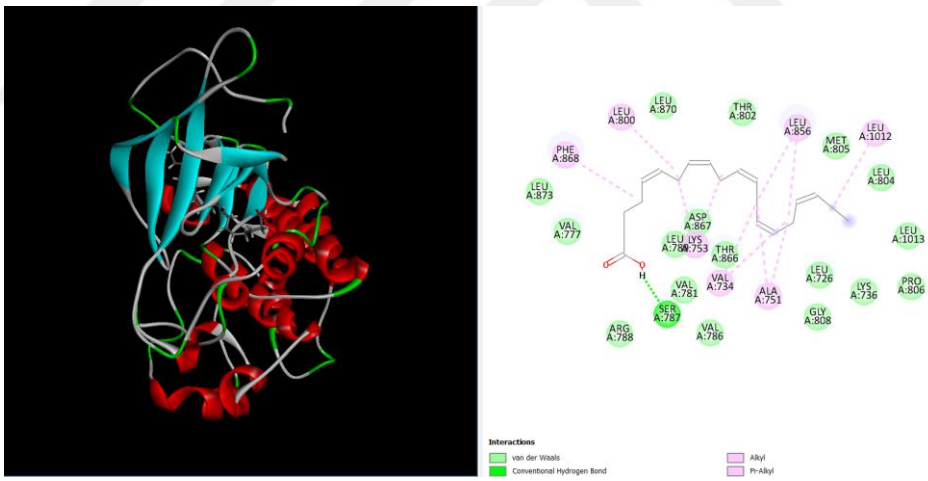

Figure 4.42. Discovery Studio 3D and 2D Ligand-Protein MDS Diagram EPA interactions with the 8U8X receptor

The 2D ligand-protein interaction diagram shown in Figure 4.42 illustrates the molecular binding mode of the EPA ligand with the 8U8X receptor, visualized using Discovery Studio. The diagram highlights a rich network of predominantly hydrophobic (alkyl and π-alkyl) interactions, as denoted by pink dashed lines, with residues such as LEU A:800, LEU A:870, LEU A:804, MET A:805, and PHE A:868, indicating that the ligand is situated within a largely hydrophobic pocket. Additionally,

van der Waals contacts are observed with residues including VAL A:777, LEU A:873, and GLY A:808, suggesting further stabilization through close-range, non-specific interactions. Importantly, conventional hydrogen bonding is identified between the EPA ligand and SER A:787, which can contribute to both binding affinity and specificity. Carbon hydrogen bonds, albeit weaker, are also involved, as seen with ASP A:867. The structural positioning of polar and nonpolar residues around the ligand implies a complementary interaction surface, where hydrophobic moieties anchor the ligand and polar side chains orient it via specific bonding. This combination of interactions indicates a stable and favorable binding conformation for EPA within the 8U8X receptor, supporting its potential as a bioactive compound in molecular docking studies.

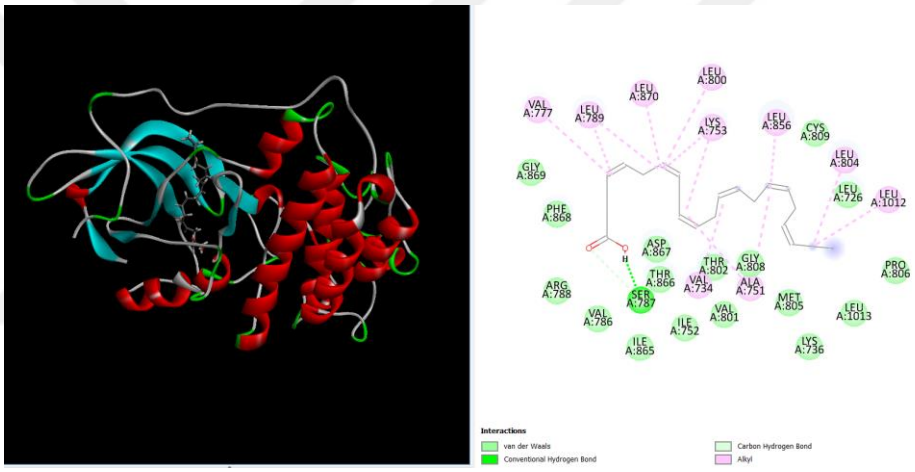

Figure 4.43. Discovery Studio 3D and 2D Ligand-Protein MDS Diagram DHA interactions with the 8U8X receptor

Figure 4.43 illustrates the binding mode of a ligand within the active site of a protein, revealing a complex network of molecular interactions that contribute to ligand affinity and specificity. Predominantly, hydrophobic (alkyl) interactions - indicated by pink dashed lines - occur between nonpolar ligand regions and hydrophobic residues such as LEU A:726, LEU A:735, and VAL A:789, stabilizing the ligand within the hydrophobic pocket. Additionally, conventional hydrogen bonds (green dashed lines) are observed with residues like ASP A:867 and SER A:864, enhancing binding specificity through directional interactions. A weaker carbon-hydrogen bond is also present with GLY A:868, while surrounding residues such as ARG A:788 and PHE A:866 engage in van der Waals contacts, contributing further to

the overall stabilization. This interaction profile suggests a well-optimized ligand conformation, balancing polar and nonpolar contacts, typical of effective lead compounds in structure-based drug design.

When the final frames obtained as a result of molecular docking and simulations are carefully examined, the common residues in Table 4.7 are shown.

Table 4.7. Common residues found in Molecular Docking and Molecular Dynamics Simulations

Receptors	Lapatinib	EPA	DHA
5MY6	ASN488, SER463, GLY464		
7PCD	MET801, THR798, GLY804, PHE864		
8U8X	GLY799, LEU785, ALA752		

Amino acid residues such as ASN A:488, SER A:463, and GLY A:464 are observed to bind commonly with all ligands in both docking and MDS results. These residues indicate that the binding pocket is structurally conserved and critical for interaction. ASN A:488, in particular, may provide stability by interacting frequently with ligands through hydrogen bonds.

Lapatinib exhibits a more complex binding pattern, with both hydrogen bonds and pi-alkyl and pi-sigma interactions. This suggests that its pharmacophore structure has more rigid and versatile binding capacity.

EPA and DHA bind primarily through hydrogen bonds and van der Waals interactions. While similar in their binding sites, they exhibit fewer interactions compared to Lapatinib. However, the similarity of the interactions formed after MDS to Lapatinib suggests that these ligands adapt to the binding site over time.

MDS last-frame analyses indicate that some bonds observed during docking undergo changes over time. This highlights the inadequacy of making decisions based solely on docking data and the importance of verifying these interactions with dynamic simulations.

A comparative analysis of the 7PCD receptor with the ligands Lapatinib, EPA, and DHA after both docking and molecular dynamics simulation (MDS) revealed that some critical amino acid residues formed repetitive binding patterns with all ligands.

According to the docking data, the ligand Lapatinib binds to the receptor with high affinity, forming numerous hydrogen and hydrophobic interactions, particularly with residues ALA751, LEU752, VAL754, ASP863, THR798, LEU800, MET801, LEU852, PHE864, and GLY804. Following MDS, it is observed that most of these bonds are preserved, and new residues such as LEU784, ALA789, and LEU785 also contribute to binding. This suggests that Lapatinib is highly stable in the binding site.

Analyses conducted with EPA revealed that the bonds formed with residues such as THR798, MET801, LEU800, GLY804, and PHE864 during the docking phase were largely preserved after MDS, particularly with MET801, THR798, and GLY804. However, the binding profile was more flexible and widespread compared to Lapatinib, suggesting a less specific binding orientation.

The DHA ligand similarly established docking interactions with ASP863, THR798, MET801, GLY804, and PHE864, preserving most of these bonds after MDS. It also appeared to contact residues such as LEU784 and ALA789. This suggests that DHA also secures a stable position in the binding site, but forms less oriented bonds than Lapatinib.

Overall, based on both docking and MDS results, residues MET801, THR798, GLY804, and PHE864 stand out as key residues that bind with all ligands, are central to the binding site, and are decisive in ligand stability. Therefore, the design of novel inhibitors targeting these regions is critical for drug development efforts targeting the 7PCD receptor.

Molecular docking and MDS analyses of the 8U8X receptor reveal that the ligands Lapatinib, EPA, and DHA target similar binding sites. Residues GLN801, GLY808, ASP863, and PHE864, in particular, stand out as key binding sites for all three ligands, providing common interactions in both docking and MDS analyses.

Lapatinib's interaction profile indicates that it forms stable bonds with additional residues such as GLY799, LEU785, and ALA752 during both the docking and MDS stages. This suggests that Lapatinib may have stronger and more stable binding capacity. This binding profile of Lapatinib supports its high-affinity binding to the 8U8X receptor and its inhibitory effect.

EPA and DHA exhibit similar interaction patterns, with binding to residues such as ARG784 and LEU785 being prominent. Although DHA has fewer interacting residues than EPA, it maintains stable binding, particularly with shared residues such as ASP863 and GLY808. This suggests that DHA has a certain stability toward the receptor, but does not exhibit as strong binding as Lapatinib.

In conclusion, both docking and MDS results indicate that Lapatinib provides the strongest and most extensive interaction with the 8U8X receptor. EPA and DHA appear to interact with the receptor through more limited but shared binding residues. Residues GLN801, GLY808, ASP863, and PHE864, in particular, could be considered potential target sites for the 8U8X receptor.

CHAPTER V. CONCLUSION AND SUGGESTIONS

This master's thesis employed molecular docking and molecular dynamics simulations (MDS) to achieve a comprehensive atomic-level characterization of breast cancer. The study focused on evaluating the potential therapeutic effects of the omega-3 fatty acids eicosapentaenoic acid (EPA) and docosahexaenoic acid (DHA), derived from krill oil, targeting HER2 receptors (5MY6, 7PCD, and 8U8X), which are known to play a pivotal role in breast cancer pathogenesis. These natural ligands were compared with the reference drug Lapatinib, widely used in breast cancer treatment.

Molecular docking results revealed that EPA and DHA exhibited strong binding affinity to HER2 receptors. These binding energies suggest that these compounds may act as inhibitors of target proteins, demonstrating their therapeutic potential. Docking analyses provided fundamental guidance for optimizing ligand-receptor interactions and enabled the selection of the most suitable candidates.

Subsequent molecular dynamics simulations offered valuable insights into the temporal stability and dynamic behavior of the ligand–receptor complexes. The structural integrity of the complexes was assessed using criteria such as gyration radius and hydrogen bonds, and it was observed that EPA and DHA formed stable interactions with the target receptors throughout the simulation period. This is a critical parameter for the efficacy of these compounds in a biological environment.

The combination of these two methods not only increased the reliability of the results but also demonstrated in a multifaceted manner that EPA and DHA derived from krill oil could be a natural and effective treatment option against breast cancer. Compared to the reference drug Lapatinib, these natural ligands offer similar or complementary binding profiles, demonstrating promise.

However, to translate these findings into clinical practice, they must be confirmed with in vitro cell culture experiments and in vivo animal models. These steps are crucial for demonstrating the efficacy and safety of EPA and DHA. If successful experimental results are obtained, evaluation of these compounds in clinical trials targeting breast cancer subtypes should be planned.

Future studies investigating different omega-3 fatty acids or other biologically active compounds from natural sources other than krill oil could contribute to the discovery of a broader pool of natural drugs suitable for breast cancer treatment. Furthermore, the use of EPA and DHA in combination with existing chemotherapy drugs could be explored to investigate synergistic effects that could increase treatment efficacy and reduce side effects.

Molecular dynamics simulations performed under various physiological conditions, such as pH and temperature, will help understand the stability of these

compounds against different environmental factors. Furthermore, integrating advanced computational techniques such as machine learning into these models could enable more accurate prediction of ligand-receptor interactions and accelerate the discovery of new potential drug candidates.

Research carried out in accordance with these recommendations will reinforce the theoretical foundation for the use of natural compounds in breast cancer therapy and support the development of effective and safe novel treatment strategies.

REFERENCES

(6) Molecular Dynamics simulations: Concepts and applications | LinkedIn. (n.d.). Retrieved 5 August 2025, from https://www.linkedin.com/pulse/molecular-dynamics-simulations-concepts-applications-chemspace-sj5se/

Agha, R. A., Al Omran, Y., Wellstead, G., Sagoo, H., Barai, I., Rajmohan, S., Borrelli, M. R., Vella-Baldacchino, M., Orgill, D. P., & Rusby, J. E. (2019). Systematic review of therapeutic nipple-sparing versus skin-sparing mastectomy. *BJS Open*, *3*(2), 135–145. https://doi.org/10.1002/bjs5.50119

Alabousi, M., Zha, N., Salameh, J.-P., Samoilov, L., Sharifabadi, A. D., Pozdnyakov, A., Sadeghirad, B., Freitas, V., McInnes, M. D. F., & Alabousi, A. (2020). Digital breast tomosynthesis for breast cancer detection: A diagnostic test accuracy systematic review and meta-analysis. *European Radiology*, *30*(4), 2058–2071. https://doi.org/10.1007/s00330-019-06549-2

Alim, N. E., & Kiziltan, G. (2016). Assessment of Risk Factors of Obesity and Diet on Breast Cancer in Ankara, Turkey. *Pakistan Journal of Medical Sciences*, *32*(6), 1537–1542. https://doi.org/10.12669/pjms.326.11346

Amadei, A., Linssen, A. B. M., & Berendsen, H. J. C. (1993). Essential dynamics of proteins. *Proteins: Structure, Function, and Bioinformatics*, *17*(4), 412–425. https://doi.org/10.1002/prot.340170408

Amini, M., Eastwood, J. W., & Hockney, R. W. (1987). Time integration in particle models. *Computer Physics Communications*, *44*(1), 83–93. https://doi.org/10.1016/0010-4655(87)90019-1

Anampa, J., Makower, D., & Sparano, J. A. (2015). Progress in adjuvant chemotherapy for breast cancer: An overview. *BMC Medicine*, *13*, 195. https://doi.org/10.1186/s12916-015-0439-8

Aris, P., Mohamadzadeh, M., Wei, Y., & Xia, X. (2022). In Silico Molecular Dynamics of Griseofulvin and Its Derivatives Revealed Potential Therapeutic Applications for COVID-19. *International Journal of Molecular Sciences*, *23*(13), 6889. https://doi.org/10.3390/ijms23136889

Bachawal, S. V., Jensen, K. C., Lutz, A. M., Gambhir, S. S., Tranquart, F., Tian, L., & Willmann, J. K. (2013). Earlier Detection of Breast Cancer with Ultrasound Molecular Imaging in a Transgenic Mouse Model. *Cancer Research*, *73*(6), 1689–1698. https://doi.org/10.1158/0008-5472.CAN-12-3391

Badar, M. S., Shamsi, S., Ahmed, J., & Alam, Md. A. (2022). Molecular Dynamics Simulations: Concept, Methods, and Applications. In N. Rezaei (Ed.), *Transdisciplinarity* (pp. 131–151). Springer International Publishing. https://doi.org/10.1007/978-3-030-94651-7_7

Bahar, I., Lezon, T. R., Yang, L.-W., & Eyal, E. (2010). Global Dynamics of Proteins: Bridging Between Structure and Function. *Annual Review of Biophysics*, *39*(Volume 39, 2010), 23–42. https://doi.org/10.1146/annurev.biophys.093008.131258

Barchiesi, G., Roberto, M., Verrico, M., Vici, P., Tomao, S., & Tomao, F. (2021). Emerging Role of PARP Inhibitors in Metastatic Triple Negative Breast Cancer. Current Scenario and Future Perspectives. *Frontiers in Oncology*, *11*, 769280. https://doi.org/10.3389/fonc.2021.769280

Barlow, W. E., Lehman, C. D., Zheng, Y., Ballard-Barbash, R., Yankaskas, B. C., Cutter, G. R., Carney, P. A., Geller, B. M., Rosenberg, R., Kerlikowske, K., Weaver, D. L., & Taplin, S. H. (2002). Performance of diagnostic mammography for women with signs or symptoms of breast cancer. *Journal of the National Cancer Institute*, *94*(15), 1151–1159. https://doi.org/10.1093/jnci/94.15.1151

Bayrakçeken, E., Yaralı, S., & Alkan, Ö. (2024). Identify risk factors affecting participation of Turkish women in mammography screening for breast cancer prevention. *Breast Cancer Research and Treatment*, *205*(3), 487–495. https://doi.org/10.1007/s10549-024-07296-9

Bekes, I., & Huober, J. (2023). Extended Adjuvant Endocrine Therapy in Early Breast Cancer Patients—Review and Perspectives. *Cancers*, *15*(16), Article 16. https://doi.org/10.3390/cancers15164190

Berge, K., Musa-Veloso, K., Harwood, M., Hoem, N., & Burri, L. (2014). Krill oil supplementation lowers serum triglycerides without increasing low-density lipoprotein cholesterol in adults with borderline high or high triglyceride levels. *Nutrition Research (New York, N.Y.)*, *34*(2), 126–133. https://doi.org/10.1016/j.nutres.2013.12.003

Bernardi, R. C., Melo, M. C. R., & Schulten, K. (2015). Enhanced sampling techniques in molecular dynamics simulations of biological systems. *Biochimica Et Biophysica Acta*, *1850*(5), 872–877. https://doi.org/10.1016/j.bbagen.2014.10.019

Breast Cancer Risk Factors in Turkey: A Hospital-based Case–control Study. (2011). *Asian Pacific Journal of Cancer Prevention*, *12*(9), 2317–2322.

Briot, N., Chagnon, G., Burlet, L., Gil, H., Girard, E., & Payan, Y. (2022). Experimental characterisation and modelling of breast Cooper's ligaments. *Biomechanics and Modeling in Mechanobiology*, *21*(4), 1157–1168. https://doi.org/10.1007/s10237-022-01582-5

Brown, J. S., Amend, S. R., Austin, R. H., Gatenby, R. A., Hammarlund, E. U., & Pienta, K. J. (2023). Updating the Definition of Cancer. *Molecular Cancer Research*, *21*(11), 1142–1147. https://doi.org/10.1158/1541-7786.MCR-23-0411

Bunea, R., El Farrah, K., & Deutsch, L. (2004). Evaluation of the effects of Neptune Krill Oil on the clinical course of hyperlipidemia. *Alternative Medicine Review: A Journal of Clinical Therapeutic*, *9*(4), 420–428.

Calder, P. C. (2015). Marine omega-3 fatty acids and inflammatory processes: Effects, mechanisms and clinical relevance. *Biochimica Et Biophysica Acta*, *1851*(4), 469–484. https://doi.org/10.1016/j.bbalip.2014.08.010

Cardoso, F., Kyriakides, S., Ohno, S., Penault-Llorca, F., Poortmans, P., Rubio, I. T., Zackrisson, S., Senkus, E., & ESMO Guidelines Committee. Electronic address: clinicalguidelines@esmo.org. (2019). Early breast cancer: ESMO Clinical Practice Guidelines for diagnosis, treatment and follow-up†. *Annals of Oncology: Official Journal of the European Society for Medical Oncology*, *30*(8), 1194–1220. https://doi.org/10.1093/annonc/mdz173

Chaurasia, M., Singh, R., Sur, S., & Flora, S. J. S. (2023). A review of FDA approved drugs and their formulations for the treatment of breast cancer. *Frontiers in Pharmacology*, *14*, 1184472. https://doi.org/10.3389/fphar.2023.1184472

Chen, W., Tu, Q., Shen, Y., Tang, K., Hong, M., & Shen, Y. (2021). Sequential vs concurrent adjuvant chemotherapy of anthracycline and taxane for operable breast cancer. *World Journal of Surgical Oncology*, *19*(1), 52. https://doi.org/10.1186/s12957-021-02150-4

Cieśla, S., Wichtowski, M., Poźniak-Balicka, R., & Murawa, D. (2020). The surgical anatomy of the mammary gland (part 1.). General structure, embryogenesis, histology, the nipple-areolar complex, the fascia of the glandular tissue and the chest wall. *Nowotwory. Journal of Oncology*, *70*(5), Article 5. https://doi.org/10.5603/NJO.2020.0042

Clarijs, M. E., Peeters, N. J. M. C. V., Dongen, S. A. F. van, Koppert, L. B., Pusic, A. L., Mureau, M. A. M., & Rijken, B. F. M. (2023). Quality of Life and Complications after Nipple- versus Skin-Sparing Mastectomy followed by Immediate Breast Reconstruction: A Systematic Review and Meta-Analysis. *Plastic and Reconstructive Surgery*, *152*(1), 12. https://doi.org/10.1097/PRS.0000000000010155

Corsetto, P. A., Montorfano, G., Zava, S., Jovenitti, I. E., Cremona, A., Berra, B., & Rizzo, A. M. (2011). Effects of n-3 PUFAs on breast cancer cells through their incorporation in plasma membrane. *Lipids in Health and Disease*, *10*(1), 73. https://doi.org/10.1186/1476-511X-10-73

Cortazar, P., Zhang, L., Untch, M., Mehta, K., Costantino, J. P., Wolmark, N., Bonnefoi, H., Cameron, D., Gianni, L., Valagussa, P., Swain, S. M., Prowell, T., Loibl, S.,

Wickerham, D. L., Bogaerts, J., Baselga, J., Perou, C., Blumenthal, G., Blohmer, J., … von Minckwitz, G. (2014). Pathological complete response and long-term clinical benefit in breast cancer: The CTNeoBC pooled analysis. *Lancet (London, England)*, *384*(9938), 164–172. https://doi.org/10.1016/S0140-6736(13)62422-8

Cserni, G. (2020). Histological type and typing of breast carcinomas and the WHO classification changes over time. *Pathologica*, *112*(1), 25–41. https://doi.org/10.32074/1591-951X-1-20

Daina, A., Michielin, O., & Zoete, V. (2017). SwissADME: A free web tool to evaluate pharmacokinetics, drug-likeness and medicinal chemistry friendliness of small molecules. *Scientific Reports*, *7*, 42717. https://doi.org/10.1038/srep42717

De La Cruz, L., Moody, A. M., Tappy, E. E., Blankenship, S. A., & Hecht, E. M. (2015). Overall Survival, Disease-Free Survival, Local Recurrence, and Nipple-Areolar Recurrence in the Setting of Nipple-Sparing Mastectomy: A Meta-Analysis and Systematic Review. *Annals of Surgical Oncology*, *22*(10), 3241–3249. https://doi.org/10.1245/s10434-015-4739-1

Deutsch, L. (2007). Evaluation of the effect of Neptune Krill Oil on chronic inflammation and arthritic symptoms. *Journal of the American College of Nutrition*, *26*(1), 39–48. https://doi.org/10.1080/07315724.2007.10719584

DeVita, V. T., Jr., & Chu, E. (2008). A History of Cancer Chemotherapy. *Cancer Research*, *68*(21), 8643–8653. https://doi.org/10.1158/0008-5472.CAN-07-6611

D'Huyvetter, M., De Vos, J., Xavier, C., Pruszynski, M., Sterckx, Y. G. J., Massa, S., Raes, G., Caveliers, V., Zalutsky, M. R., Lahoutte, T., & Devoogdt, N. (2017). 131I-labeled Anti-HER2 Camelid sdAb as a Theranostic Tool in Cancer Treatment. *Clinical Cancer Research: An Official Journal of the American Association for Cancer Research*, *23*(21), 6616–6628. https://doi.org/10.1158/1078-0432.CCR-17-0310

Dowsett, M., Cuzick, J., Ingle, J., Coates, A., Forbes, J., Bliss, J., Buyse, M., Baum, M., Buzdar, A., Colleoni, M., Coombes, C., Snowdon, C., Gnant, M., Jakesz, R., Kaufmann, M., Boccardo, F., Godwin, J., Davies, C., & Peto, R. (2010). Meta-analysis of breast cancer outcomes in adjuvant trials of aromatase inhibitors versus tamoxifen. *Journal of Clinical Oncology: Official Journal of the American Society of Clinical Oncology*, *28*(3), 509–518. https://doi.org/10.1200/JCO.2009.23.1274

Duncan, A. M., Al Youha, S., Joukhadar, N., Konder, R., Stecco, C., & Wheelock, M. E. (2022). Anatomy of the Breast Fascial System: A Systematic Review of the Literature. *Plastic and Reconstructive Surgery*, *149*(1), 28–40. https://doi.org/10.1097/PRS.0000000000008671

Early Breast Cancer Trialists' Collaborative Group (EBCTCG). (2015). Aromatase inhibitors versus tamoxifen in early breast cancer: Patient-level meta-analysis of the randomised trials. *Lancet (London, England)*, *386*(10001), 1341–1352. https://doi.org/10.1016/S0140-6736(15)61074-1

Elahi, R., & Nazari, M. (2024). *An updated overview of radiomics-based artificial intelligence (AI) methods in breast cancer screening and diagnosis* (No. arXiv:2406.14735). arXiv. https://doi.org/10.48550/arXiv.2406.14735

Essmann, U., Perera, L., Berkowitz, M. L., Darden, T., Lee, H., & Pedersen, L. G. (1995). A smooth particle mesh Ewald method. *The Journal of Chemical Physics*, *103*(19), 8577–8593. https://doi.org/10.1063/1.470117

Farooq, M. S., & Ilyas, M. (2023). *Predicting environment effects on breast cancer by implementing machine learning* (No. arXiv:2309.14397). arXiv. https://doi.org/10.48550/arXiv.2309.14397

Fenech, M., Burke, T., Arnett, G., Tanner, A., & Werder, N. (2025). Sonographic localisation of lymph nodes suspicious of metastatic breast cancer to surgical axillary levels. *Journal of Medical Radiation Sciences*, *72*(1), 119–138. https://doi.org/10.1002/jmrs.840

Ferreira, L. G., Dos Santos, R. N., Oliva, G., & Andricopulo, A. D. (2015). Molecular Docking and Structure-Based Drug Design Strategies. *Molecules*, *20*(7), Article 7. https://doi.org/10.3390/molecules200713384

Fisher, B., Anderson, S., Bryant, J., Margolese, R. G., Deutsch, M., Fisher, E. R., Jeong, J.-H., & Wolmark, N. (2002). Twenty-Year Follow-up of a Randomized Trial Comparing Total Mastectomy, Lumpectomy, and Lumpectomy plus Irradiation for the Treatment of Invasive Breast Cancer. *New England Journal of Medicine*, *347*(16), 1233–1241. https://doi.org/10.1056/NEJMoa022152

Fisher, B., Anderson, S., Redmond, C. K., Wolmark, N., Wickerham, D. L., & Cronin, W. M. (1995). Reanalysis and Results after 12 Years of Follow-up in a Randomized Clinical Trial Comparing Total Mastectomy with Lumpectomy with or without Irradiation in the Treatment of Breast Cancer. *New England Journal of Medicine*, *333*(22), 1456–1461. https://doi.org/10.1056/NEJM199511303332203

Fitton, J. H. (2011). Therapies from Fucoidan; Multifunctional Marine Polymers. *Marine Drugs*, *9*(10), Article 10. https://doi.org/10.3390/md9101731

Francis, P. A., Pagani, O., Fleming, G. F., Walley, B. A., Colleoni, M., Láng, I., Gómez, H. L., Tondini, C., Ciruelos, E., Burstein, H. J., Bonnefoi, H. R., Bellet, M., Martino, S., Geyer, C. E., Goetz, M. P., Stearns, V., Pinotti, G., Puglisi, F., Spazzapan, S., … Regan, M. M. (2018). Tailoring Adjuvant Endocrine Therapy for Premenopausal Breast Cancer. *New England Journal of Medicine*, *379*(2), 122–137. https://doi.org/10.1056/NEJMoa1803164

Friedrichs, M. S., Eastman, P., Vaidyanathan, V., Houston, M., Legrand, S., Beberg, A. L., Ensign, D. L., Bruns, C. M., & Pande, V. S. (2009). Accelerating Molecular Dynamic Simulation on Graphics Processing Units. *Journal of Computational Chemistry*, *30*(6), 864–872. https://doi.org/10.1002/jcc.21209

Galimberti, V., Morigi, C., Bagnardi, V., Corso, G., Vicini, E., Fontana, S. K. R., Naninato, P., Ratini, S., Magnoni, F., Toesca, A., Kouloura, A., Rietjens, M., De Lorenzi, F., Vingiani, A., & Veronesi, P. (2018). Oncological Outcomes of Nipple-Sparing Mastectomy: A Single-Center Experience of 1989 Patients. *Annals of Surgical Oncology*, *25*(13), 3849–3857. https://doi.org/10.1245/s10434-018-6759-0

Geromichalos, G. D. (2007). Importance of molecular computer modeling in anticancer drug development. *Journal of B.U.ON.: Official Journal of the Balkan Union of Oncology*, *12 Suppl 1*, S101-118.

Ghaed-Sharaf, T., & Omidvar, A. (2022). Exploring the permeability of covid-19 drugs within the cellular membrane: A molecular dynamics simulation study. *Physical Chemistry Chemical Physics*, *24*(10), 6215–6224. https://doi.org/10.1039/D1CP05550J

Gioia, D., Bertazzo, M., Recanatini, M., Masetti, M., & Cavalli, A. (2017). Dynamic Docking: A Paradigm Shift in Computational Drug Discovery. *Molecules*, *22*(11), Article 11. https://doi.org/10.3390/molecules22112029

Hagen, J. B. (2000). The origins of bioinformatics. *Nature Reviews. Genetics*, *1*(3), 231–236. https://doi.org/10.1038/35042090

Hajdu, S. I. (2011). A note from history: Landmarks in history of cancer, part 1. *Cancer*, *117*(5), 1097–1102. https://doi.org/10.1002/cncr.25553

Han, Y., & Wei, L. (2025). Novel clinical potential of poly (ADP-ribose) polymerase inhibitors in triple-negative breast cancer: Mechanistic insights and clinical applications (Review). *Oncology Letters*, *29*(5), 1–14. https://doi.org/10.3892/ol.2025.14961

Hanahan, D., & Weinberg, R. A. (2000). The hallmarks of cancer. *Cell*, *100*(1), 57–70. https://doi.org/10.1016/s0092-8674(00)81683-9

Hansford, S., & Huntsman, D. G. (2014). Boveri at 100: Theodor Boveri and genetic predisposition to cancer. *The Journal of Pathology*, *234*(2), 142–145. https://doi.org/10.1002/path.4414

Hesper, B., & Hogeweg, P. (2021). *Bio-informatics: A working concept. A translation of 'Bio-informatica: een werkconcept' by B. Hesper and P. Hogeweg* (No. arXiv:2111.11832). arXiv. https://doi.org/10.48550/arXiv.2111.11832

Hicken, E. J., Brown, K., Dwulet, N. C., Gaudino, J. J., Hansen, E. P., Hartley, D. P., Kowalski, J. P., Laird, E. R., Lazzara, N. C., Li, B., Mou, T.-C., Mutryn, M. F., Oko, L., Pajk, S., Pipal, R. W., Rosen, R. Z., Shelp, R., Singh, A., Wang, J., … Wong, J. Y. (2024).

Discovery of Potent and Selective Covalent Inhibitors of HER2WT and HER2YVMA. *Journal of Medicinal Chemistry*, *67*(11), 9759–9771. https://doi.org/10.1021/acs.jmedchem.4c00978

Hickey, B. E., Lehman, M., Francis, D. P., & See, A. M. (n.d.). *Partial breast irradiation for early breast cancer—Hickey, BE - 2016 | Cochrane Library*. Retrieved 6 August 2025, from https://www.cochranelibrary.com/cdsr/doi/10.1002/14651858.CD007077.pub3/full

Hollingsworth, S. A., & Dror, R. O. (2018). Molecular Dynamics Simulation for All. *Neuron*, *99*(6), 1129–1143. https://doi.org/10.1016/j.neuron.2018.08.011

Hu, H., Wei, W., Yi, X., Xin, L., & Liu, Y. (2017). A Retrospective Analysis of Clinical Utility of AJCC 8th Edition Cancer Staging System for Breast Cancer. *World Journal of Oncology*, *8*(3), 71–75. https://doi.org/10.14740/wjon1039e

Huang, S.-Y., Grinter, S. Z., & Zou, X. (2010). Scoring functions and their evaluation methods for protein–ligand docking: Recent advances and future directions. *Physical Chemistry Chemical Physics*, *12*(40), 12899–12908. https://doi.org/10.1039/C0CP00151A

Jayathilake, A. G., Senior, P. V., & Su, X. Q. (2016). Krill oil extract suppresses cell growth and induces apoptosis of human colorectal cancer cells. *BMC Complementary and Alternative Medicine*, *16*(1), 328. https://doi.org/10.1186/s12906-016-1311-x

Jing, Z., Liu, C., Cheng, S. Y., Qi, R., Walker, B. D., Piquemal, J.-P., & Ren, P. (2019). Polarizable Force Fields for Biomolecular Simulations: Recent Advances and Applications. *Annual Review of Biophysics*, *48*(Volume 48, 2019), 371–394. https://doi.org/10.1146/annurev-biophys-070317-033349

Johnston, S. R. D., & Dowsett, M. (2003). Aromatase inhibitors for breast cancer: Lessons from the laboratory. *Nature Reviews. Cancer*, *3*(11), 821–831. https://doi.org/10.1038/nrc1211

Jordan, M. A., & Wilson, L. (2004). Microtubules as a target for anticancer drugs. *Nature Reviews Cancer*, *4*(4), 253–265. https://doi.org/10.1038/nrc1317

Jumper, J., Evans, R., Pritzel, A., Green, T., Figurnov, M., Ronneberger, O., Tunyasuvunakool, K., Bates, R., Žídek, A., Potapenko, A., Bridgland, A., Meyer, C., Kohl, S. A. A., Ballard, A. J., Cowie, A., Romera-Paredes, B., Nikolov, S., Jain, R., Adler, J., … Hassabis, D. (2021). Highly accurate protein structure prediction with AlphaFold. *Nature*, *596*(7873), 583–589. https://doi.org/10.1038/s41586-021-03819-2

Kamal, I. M., & Chakrabarti, S. (2023). MetaDOCK: A Combinatorial Molecular Docking Approach. *ACS Omega*, *8*(6), 5850–5860. https://doi.org/10.1021/acsomega.2c07619

Khotimchenko, Y. (2018). Pharmacological Potential of Sea Cucumbers. *International Journal of Molecular Sciences*, *19*(5), 1342. https://doi.org/10.3390/ijms19051342

Kim, I., Choi, H. J., Ryu, J. M., Lee, S. K., Yu, J. H., Kim, S. W., Nam, S. J., & Lee, J. E. (2018). Prognostic Validation of the American Joint Committee on Cancer 8th Staging System in 24,014 Korean Patients with Breast Cancer. *Journal of Breast Cancer*, *21*(2), 173–181. https://doi.org/10.4048/jbc.2018.21.2.173

Kim, J. H., Meng, H. W., He, M. T., Choi, J. M., Lee, D., & Cho, E. J. (2020). Krill Oil Attenuates Cognitive Impairment by the Regulation of Oxidative Stress and Neuronal Apoptosis in an Amyloid β-Induced Alzheimer's Disease Mouse Model. *Molecules*, *25*(17), Article 17. https://doi.org/10.3390/molecules25173942

Kondo, N., Takahashi, A., Ono, K., & Ohnishi, T. (2010). DNA Damage Induced by Alkylating Agents and Repair Pathways. *Journal of Nucleic Acids*, *2010*, 543531. https://doi.org/10.4061/2010/543531

Kühne, T. D., Krack, M., Mohamed, F. R., & Parrinello, M. (2007). Efficient and Accurate Car-Parrinello-like Approach to Born-Oppenheimer Molecular Dynamics. *Physical Review Letters*, *98*(6), 066401. https://doi.org/10.1103/PhysRevLett.98.066401

Kuru, B., Ozaslan, C., Ozdemir, P., Dinç, S., Camlibel, M., & Alagöl, H. (2002). Risk Factors for Breast Cancer in Turkish Women with Early Pregnancies and Long-lasting

Lactation. *Acta Oncologica*, *41*(6), Article 6. https://doi.org/10.1080/02841860214964

Laohavinij, S., Ruikchuchit, K., & Maneechavakajorn, J. (2013). Survival and prognostic factors of stage I-III breast cancer. *Journal of the Medical Association of Thailand = Chotmaihet Thangphaet*, *96 Suppl 3*, S23-34.

Leclerc, A.-F., Jerusalem, G., Devos, M., Crielaard, J.-M., & Maquet, D. (2016). Multidisciplinary management of breast cancer. *Archives of Public Health = Archives Belges De Sante Publique*, *74*, 50. https://doi.org/10.1186/s13690-016-0163-7

Lee, S. H., Ryu, H.-S., Jang, M.-J., Yi, A., Ha, S. M., Kim, S.-Y., Chang, J. M., Cho, N., & Moon, W. K. (2021). Glandular Tissue Component and Breast Cancer Risk in Mammographically Dense Breasts at Screening Breast US. *Radiology*, *301*(1), 57–65. https://doi.org/10.1148/radiol.2021210367

Lemkul, J. A. (2019). From Proteins to Perturbed Hamiltonians: A Suite of Tutorials for the GROMACS-2018 Molecular Simulation Package [Article v1.0]. *Living Journal of Computational Molecular Science*, *1*(1), 5068–5068. https://doi.org/10.33011/livecoms.1.1.5068

Lemkul, J. A. (2024). Introductory Tutorials for Simulating Protein Dynamics with GROMACS. *The Journal of Physical Chemistry B*, *128*(39), 9418–9435. https://doi.org/10.1021/acs.jpcb.4c04901

Lexa, K. W., & Carlson, H. A. (2012). Protein flexibility in docking and surface mapping. *Quarterly Reviews of Biophysics*, *45*(3), 301–343. https://doi.org/10.1017/S0033583512000066

Lian, C.-L., Li, G.-Q., Zhou, P., Wang, J., He, Z.-Y., & Wu, S.-G. (2021). Triple-negative breast cancer outcomes: Does AJCC 8th staging improve chemotherapy decision-making. *Breast (Edinburgh, Scotland)*, *59*, 117–123. https://doi.org/10.1016/j.breast.2021.06.009

Libson, S., & Lippman, M. (2014). A review of clinical aspects of breast cancer. *International Review of Psychiatry (Abingdon, England)*, *26*(1), 4–15. https://doi.org/10.3109/09540261.2013.852971

Lindorff-Larsen, K., Piana, S., Palmo, K., Maragakis, P., Klepeis, J. L., Dror, R. O., & Shaw, D. E. (2010). Improved side-chain torsion potentials for the Amber ff99SB protein force field. *Proteins: Structure, Function, and Bioinformatics*, *78*(8), 1950–1958. https://doi.org/10.1002/prot.22711

Liu, S., Tang, Y., Li, J., & Zhao, W. (2024). Global, regional, and national trends in the burden of breast cancer among individuals aged 70 years and older from 1990 to 2021: An analysis based on the global burden of disease study 2021. *Archives of Public Health*, *82*(1), 170. https://doi.org/10.1186/s13690-024-01404-3

Lukong, K. E. (2017). Understanding breast cancer – The long and winding road. *BBA Clinical*, *7*, 64–77. https://doi.org/10.1016/j.bbacli.2017.01.001

Magnoni, F., Alessandrini, S., Alberti, L., Polizzi, A., Rotili, A., Veronesi, P., & Corso, G. (2021). Breast Cancer Surgery: New Issues. *Current Oncology*, *28*(5), 4053–4066. https://doi.org/10.3390/curroncol28050344

Martyna, G. J., Hughes, A., & Tuckerman, M. E. (1999). Molecular dynamics algorithms for path integrals at constant pressure. *The Journal of Chemical Physics*, *110*(7), 3275–3290. https://doi.org/10.1063/1.478193

Martyna, G. J., Tobias, D. J., & Klein, M. L. (1994). Constant pressure molecular dynamics algorithms. *The Journal of Chemical Physics*, *101*(5), 4177–4189. https://doi.org/10.1063/1.467468

Meng, X.-Y., Zhang, H.-X., Mezei, M., & Cui, M. (2011). Molecular Docking: A powerful approach for structure-based drug discovery. *Current Computer-Aided Drug Design*, *7*(2), 146–157. https://doi.org/10.2174/157340911795677602

Minotti, G., Menna, P., Salvatorelli, E., Cairo, G., & Gianni, L. (2004). Anthracyclines: Molecular advances and pharmacologic developments in antitumor activity and cardiotoxicity. *Pharmacological Reviews*, *56*(2), 185–229. https://doi.org/10.1124/pr.56.2.6

Mittendorf, E. A., Bartlett, J. M. S., Lichtensztajn, D. L., & Chandarlapaty, S. (2018). Incorporating Biology Into Breast Cancer Staging: American Joint Committee on Cancer, Eighth Edition, Revisions and Beyond. *American Society of Clinical Oncology Educational Book*, *38*, 38–46. https://doi.org/10.1200/EDBK_200981

Molinski, T. F., Dalisay, D. S., Lievens, S. L., & Saludes, J. P. (2009). Drug development from marine natural products. *Nature Reviews Drug Discovery*, *8*(1), 69–85. https://doi.org/10.1038/nrd2487

Morishita, M., & Leonard, R. C. (2008). Capecitabine and docetaxel combination for the treatment of breast cancer. *Women's Health (London, England)*, *4*, 11–22. https://doi.org/10.2217/17455057.4.1.11

Mortier, J., Rakers, C., Bermudez, M., Murgueitio, M. S., Riniker, S., & Wolber, G. (2015). The impact of molecular dynamics on drug design: Applications for the characterization of ligand-macromolecule complexes. *Drug Discovery Today*, *20*(6), 686–702. https://doi.org/10.1016/j.drudis.2015.01.003

Mukesh, M. B., Qian, W., Wah Hak, C. C., Wilkinson, J. S., Barnett, G. C., Moody, A. M., Wilson, C., & Coles, C. E. (2016). The Cambridge Breast Intensity-modulated Radiotherapy Trial: Comparison of Clinician- versus Patient-reported Outcomes. *Clinical Oncology*, *28*(6), 354–364. https://doi.org/10.1016/j.clon.2016.02.011

Náray-Szabó, G., Oláh, J., & Krámos, B. (2013). Quantum Mechanical Modeling: A Tool for the Understanding of Enzyme Reactions. *Biomolecules*, *3*(3), Article 3. https://doi.org/10.3390/biom3030662

Nelson, H. D., Fu, R., Cantor, A., Pappas, M., Daeges, M., & Humphrey, L. (2016). Effectiveness of Breast Cancer Screening: Systematic Review and Meta-analysis to Update the 2009 U.S. Preventive Services Task Force Recommendation. *Annals of Internal Medicine*, *164*(4), 244–255. https://doi.org/10.7326/M15-0969

Orrantia-Borunda, E., Anchondo-Nuñez, P., Acuña-Aguilar, L. E., Gómez-Valles, F. O., & Ramírez-Valdespino, C. A. (2022). Subtypes of Breast Cancer. In H. N. Mayrovitz (Ed.), *Breast Cancer*. Exon Publications. http://www.ncbi.nlm.nih.gov/books/NBK583808/

Pagadala, N. S., Syed, K., & Tuszynski, J. (2017). Software for molecular docking: A review. *Biophysical Reviews*, *9*(2), 91–102. https://doi.org/10.1007/s12551-016-0247-1

Pislyagin, E. A., Aminin, D. L., Silchenko, A. S., Avilov, S. A., Andryjashchenko, P. V., Kalinin, V. I., & Padmakumar, K. (2014). Immunomodulatory action of triterpene glycosides isolated from the sea cucumber Actinocucumis typica. Structure-activity relationships. *Natural Product Communications*, *9*(6), 771–772.

Pitera, J. W. (2014). Expected distributions of root-mean-square positional deviations in proteins. *The Journal of Physical Chemistry. B*, *118*(24), 6526–6530. https://doi.org/10.1021/jp412776d

Pommier, Y. (2006). Topoisomerase I inhibitors: Camptothecins and beyond. *Nature Reviews. Cancer*, *6*(10), 789–802. https://doi.org/10.1038/nrc1977

Prasad, M., & Chakraborty, S. N. (2022). Hydrogen bonding in liquid water at 1 GPa: Molecular dynamics simulation study of TIP4P/2005 water model. *Computational and Theoretical Chemistry*, *1208*, 113527. https://doi.org/10.1016/j.comptc.2021.113527

Prat, A., Parker, J. S., Fan, C., Cheang, M. C. U., Miller, L. D., Bergh, J., Chia, S. K. L., Bernard, P. S., Nielsen, T. O., Ellis, M. J., Carey, L. A., & Perou, C. M. (2012). Concordance among gene expression-based predictors for ER-positive breast cancer treated with adjuvant tamoxifen. *Annals of Oncology: Official Journal of the European Society for Medical Oncology*, *23*(11), 2866–2873. https://doi.org/10.1093/annonc/mds080

Rakhshani, H., Idoumghar, L., Lepagnot, J., Brevilliers, M., & Keedwell, E. (2018). *Automatic hyperparameter selection in Autodock* (No. arXiv:1812.02618). arXiv. https://doi.org/10.48550/arXiv.1812.02618

Ray, A. K., Sen Gupta, P. S., Panda, S. K., Biswal, S., Bhattacharya, U., & Rana, M. K. (2022). Repurposing of FDA-approved drugs as potential inhibitors of the SARS-CoV-2 main

protease: Molecular insights into improved therapeutic discovery. *Computers in Biology and Medicine*, *142*, 105183. https://doi.org/10.1016/j.compbiomed.2021.105183

Sali, A., & Blundell, T. L. (1993). Comparative protein modelling by satisfaction of spatial restraints. *Journal of Molecular Biology*, *234*(3), 779–815. https://doi.org/10.1006/jmbi.1993.1626

Sanchez-Cespedes, M., Ahrendt, S. A., Piantadosi, S., Rosell, R., Monzo, M., Wu, L., Westra, W. H., Yang, S. C., Jen, J., & Sidransky, D. (2001). Chromosomal Alterations in Lung Adenocarcinoma from Smokers and Nonsmokers1. *Cancer Research*, *61*(4), 1309–1313.

Sargsyan, K., Grauffel, C., & Lim, C. (2017). How Molecular Size Impacts RMSD Applications in Molecular Dynamics Simulations. *Journal of Chemical Theory and Computation*, *13*(4), 1518–1524. https://doi.org/10.1021/acs.jctc.7b00028

Sarıyer, E. T., Baş, M., & Yüksel, M. (2025). Comparative Analysis of the Antioxidant and Anti-Inflammatory Effects of Krill and Fish Oil. *International Journal of Molecular Sciences*, *26*(15), Article 15. https://doi.org/10.3390/ijms26157360

Schlick, T., Collepardo-Guevara, R., Halvorsen, L. A., Jung, S., & Xiao, X. (2011). Biomolecularmodeling and simulation: A field coming of age. *Quarterly Reviews of Biophysics*, *44*(2), 191–228. https://doi.org/10.1017/S0033583510000284

Senthilkumar, K., & Kim, S.-K. (2013). Marine Invertebrate Natural Products for Anti-Inflammatory and Chronic Diseases. *Evidence-Based Complementary and Alternative Medicine : eCAM*, *2013*, 572859. https://doi.org/10.1155/2013/572859

Si, M., Jiao, Y., Xu, L., Lin, R., Zhong, X., & Lv, Q. (2025). Long-term outcomes of skin-sparing mastectomy and nipple-sparing mastectomy versus traditional mastectomy in breast cancer: A case-control study based on preoperative ultrasound and clinical indicators. *World Journal of Surgical Oncology*, *23*(1), 52. https://doi.org/10.1186/s12957-025-03695-4

Smith, K. A., Hunt, K. N., Rauch, G. M., & Fowler, A. M. (2023). Molecular Breast Imaging in the Screening Setting. *Journal of Breast Imaging*, *5*(3), 240–247. https://doi.org/10.1093/jbi/wbad011

Smith, R. D., Hu, L., Falkner, J. A., Benson, M. L., Nerothin, J. P., & Carlson, H. A. (2006). Exploring protein-ligand recognition with Binding MOAD. *Journal of Molecular Graphics & Modelling*, *24*(6), 414–425. https://doi.org/10.1016/j.jmgm.2005.08.002

Sousa, S. F., Fernandes, P. A., & Ramos, M. J. (2006). Protein–ligand docking: Current status and future challenges. *Proteins: Structure, Function, and Bioinformatics*, *65*(1), 15–26. https://doi.org/10.1002/prot.21082

Sun, P., Tsang, J., Xu, X., Li, J., Li, M., Chao, X., Luo, R., Tse, G., & He, J. (2020). Abstract P5-06-19: AJCC 8th edition prognostic staging system provide no better discriminatory ability in prognosis than anatomical staging system in triple negative breast cancer: A cohort from two institutions and a large population based study. *Cancer Research*, *80*(4_Supplement), P5-06–19. https://doi.org/10.1158/1538-7445.SABCS19-P5-06-19

Sung, H., Ferlay, J., Siegel, R. L., Laversanne, M., Soerjomataram, I., Jemal, A., & Bray, F. (2021). Global Cancer Statistics 2020: GLOBOCAN Estimates of Incidence and Mortality Worldwide for 36 Cancers in 185 Countries. *CA: A Cancer Journal for Clinicians*, *71*(3), 209–249. https://doi.org/10.3322/caac.21660

Tacar, O., Sriamornsak, P., & Dass, C. R. (2013). Doxorubicin: An update on anticancer molecular action, toxicity and novel drug delivery systems. *The Journal of Pharmacy and Pharmacology*, *65*(2), 157–170. https://doi.org/10.1111/j.2042-7158.2012.01567.x

Tamburella, C., Guibert, G., Cruz, O. S., Weber, P., & Tsousou, P. (2019). *A volumetric Modulated Arc Therapy (VMAT) combined with deep inspiration breath hold (DIBH) technique for adjuvant irradiation for left sided breast cancer* (No. arXiv:1706.06867). arXiv. https://doi.org/10.48550/arXiv.1706.06867

Thampi, S. M. (2009). *Introduction to Bioinformatics* (No. arXiv:0911.4230). arXiv. https://doi.org/10.48550/arXiv.0911.4230

Theoretical Modeling of Nanostructured Formation in Polymer Blends | Request PDF. (n.d.). ResearchGate. https://doi.org/10.1016/B978-1-4557-3159-6.00003-1

Thomas, D. M., & Zalcberg, J. R. (1998). 5-fluorouracil: A pharmacological paradigm in the use of cytotoxics. *Clinical and Experimental Pharmacology & Physiology*, *25*(11), 887–895. https://doi.org/10.1111/j.1440-1681.1998.tb02339.x

Thomssen, C., Balic, M., Harbeck, N., & Gnant, M. (2021). St. Gallen/Vienna 2021: A Brief Summary of the Consensus Discussion on Customizing Therapies for Women with Early Breast Cancer. *Breast Care (Basel, Switzerland)*, *16*(2), 135–143. https://doi.org/10.1159/000516114

Tou, J. C., Jaczynski, J., & Chen, Y.-C. (2007). Krill for human consumption: Nutritional value and potential health benefits. *Nutrition Reviews*, *65*(2), 63–77. https://doi.org/10.1111/j.1753-4887.2007.tb00283.x

Tremont, S. J., Collins, P. W., Perkins, W. E., Fenton, R. L., Forster, D., McGrath, M. P., Wagner, G. M., Gasiecki, A. F., & Bianchi, R. G. (1993). Catalytic functionalization of polymers: A novel approach to site-specific delivery of misoprostol to the stomach. *Journal of Medicinal Chemistry*, *36*(21), 3087–3097. https://doi.org/10.1021/jm00073a007

Tripathi, A., & Bankaitis, V. A. (2017). Molecular Docking: From Lock and Key to Combination Lock. *Journal of Molecular Medicine and Clinical Applications*, *2*(1). https://doi.org/10.16966/2575-0305.106

Trott, O., & Olson, A. J. (2010). AutoDock Vina: Improving the speed and accuracy of docking with a new scoring function, efficient optimization, and multithreading. *Journal of Computational Chemistry*, *31*(2), 455–461. https://doi.org/10.1002/jcc.21334

Vaidya, J. S., Bulsara, M., Baum, M., Wenz, F., Massarut, S., Pigorsch, S., Alvarado, M., Douek, M., Saunders, C., Flyger, H. L., Eiermann, W., Brew-Graves, C., Williams, N. R., Potyka, I., Roberts, N., Bernstein, M., Brown, D., Sperk, E., Laws, S., … Tobias, J. S. (2020). Long term survival and local control outcomes from single dose targeted intraoperative radiotherapy during lumpectomy (TARGIT-IORT) for early breast cancer: TARGIT-A randomised clinical trial. *BMJ (Clinical Research Ed.)*, *370*, m2836. https://doi.org/10.1136/bmj.m2836

van der Poort, E. K. J., van Ravesteyn, N. T., van den Broek, J. J., & de Koning, H. J. (2022). The Early Detection of Breast Cancer Using Liquid Biopsies: Model Estimates of the Benefits, Harms, and Costs. *Cancers*, *14*(12), Article 12. https://doi.org/10.3390/cancers14122951

Varshney, R. K., Graner, A., & Sorrells, M. E. (2005). Genic microsatellite markers in plants: Features and applications. *Trends in Biotechnology*, *23*(1), 48–55. https://doi.org/10.1016/j.tibtech.2004.11.005

Veronesi, U., Orecchia, R., Maisonneuve, P., Viale, G., Rotmensz, N., Sangalli, C., Luini, A., Veronesi, P., Galimberti, V., Zurrida, S., Leonardi, M. C., Lazzari, R., Cattani, F., Gentilini, O., Intra, M., Caldarella, P., & Ballardini, B. (2013). Intraoperative radiotherapy versus external radiotherapy for early breast cancer (ELIOT): A randomised controlled equivalence trial. *The Lancet Oncology*, *14*(13), 1269–1277. https://doi.org/10.1016/S1470-2045(13)70497-2

Waks, A. G., & Winer, E. P. (2019). Breast Cancer Treatment: A Review. *JAMA*, *321*(3), 288–300. https://doi.org/10.1001/jama.2018.19323

Wang, D., & Lippard, S. J. (2005). Cellular processing of platinum anticancer drugs. *Nature Reviews. Drug Discovery*, *4*(4), 307–320. https://doi.org/10.1038/nrd1691

Wang, L. (2017). Early Diagnosis of Breast Cancer. *Sensors (Basel, Switzerland)*, *17*(7), 1572. https://doi.org/10.3390/s17071572

Welcome to the GROMACS documentation! —GROMACS documentation. (n.d.). Retrieved 7 August 2025, from https://manual.gromacs.org/

Wilding, B., Scharn, D., Böse, D., Baum, A., Santoro, V., Chetta, P., Schnitzer, R., Botesteanu, D. A., Reiser, C., Kornigg, S., Knesl, P., Hörmann, A., Köferle, A., Corcokovic, M., Lieb, S., Scholz, G., Bruchhaus, J., Spina, M., Balla, J., … Neumüller, R. A. (2022). Discovery of potent and selective HER2 inhibitors with efficacy against HER2 exon 20 insertion-driven tumors, which preserve wild-type EGFR signaling. *Nature Cancer*, *3*(7), 821–836. https://doi.org/10.1038/s43018-022-00412-y

Wu, H.-J., & Chu, P.-Y. (2022). Current and Developing Liquid Biopsy Techniques for Breast Cancer. *Cancers*, *14*(9), 2052. https://doi.org/10.3390/cancers14092052

Yang, C., Chen, E. A., & Zhang, Y. (2022). Protein–Ligand Docking in the Machine-Learning Era. *Molecules*, *27*(14), Article 14. https://doi.org/10.3390/molecules27144568

Yekdeş, A. C., Yekdeş, D. H., Çelikkalp, Ü., & Ekuklu, G. (n.d.). Modifiable Risk Factors for Breast Cancer Mortality in Türkiye from 1990 to 2019: A Temporal Analysis of Global Burden of Disease Data. *Balkan Medical Journal*, *41*(4), 298–305. https://doi.org/10.4274/balkanmedj.galenos.2024.2024-4-91

Zaborowski, A. M., Roe, S., Rothwell, J., Evoy, D., Geraghty, J., McCartan, D., & Prichard, R. S. (2023). A systematic review of oncological outcomes after nipple-sparing mastectomy for breast cancer. *Journal of Surgical Oncology*, *127*(3), 361–368. https://doi.org/10.1002/jso.27115

Zou, Z., Bellenger, S., Massey, K. A., Nicolaou, A., Geissler, A., Bidu, C., Bonnotte, B., Pierre, A.-S., Minville-Walz, M., Rialland, M., Seubert, J., Kang, J. X., Lagrost, L., Narce, M., & Bellenger, J. (2013). Inhibition of the HER2 pathway by n-3 polyunsaturated fatty acids prevents breast cancer in fat-1 transgenic mice. *Journal of Lipid Research*, *54*(12), 3453–3463. https://doi.org/10.1194/jlr.M042754

Zucca-Matthes, G., Urban, C., & Vallejo, A. (2016). Anatomy of the nipple and breast ducts. *Gland Surgery*, *5*(1), 32–36. https://doi.org/10.3978/j.issn.2227-684X.2015.05.10

APPENDIX

Table A.1. Docking results for the 5MY6 receptor with Autodock Vina at 4 different locations.

Receptor	CHEMBL Code	Active Site Center			
		20-20-20	30-30-30	40-40-40	Co-crystalised ligand position
Abemaciclib	CHEMBL3301610	-8,7	-8,6	-9,3	-8,7
nab-paclitaxel	CHEMBL428647	-11,2	-10,2	-10,2	-11,2
everolimus	CHEMBL1908360	-8,1	-11,2	-11,2	-11,2
alpelisib	CHEMBL2396661	-8,1	-8,1	-8,3	-8,1
anastrozole	CHEMBL1399	-7,1	-7,1	-6,5	-7,2
pamidronatedi-sodium	CHEMBL676	-5,1	-5,2	-5,1	-5,1
exemestane	CHEMBL1200374	-8	-8	-7,9	-8
capecitabine	CHEMBL1773	-7,2	-7,1	-7,1	-7,1
capivasertib	CHEMBL2325741	-8,5	-8,6	-8,3	-8,6
Cyclophosphamide	CHEMBL1453	-5,2	-5,2	-5,2	-5,2
doxorubicin_hydrochloride	CHEMBL1486	-8,2	-8,2	-8,2	-8,2
elacestrant_hydrochloride	CHEMBL4297509	-7,5	-7,5	-6,7	-7,5
epirubicin_hydrochloride	CHEMBL449442	-8,4	-7,9	-8,3	-8,4
fluorouracil	CHEMBL25	-5,1	-5,4	-5,4	-4,9
fulvestrant	CHEMBL2452	-7,6	-8,9	-8,8	-8,4
letrozole	CHEMBL1444	-6,8	-6,8	-6,8	-6,8
gemcitabine_hydrochloride	CHEMBL888	-6,7	-6,7	-6,9	6,7
Trastuzumab	CHEMBL1201505	-9,3	-9,2	-9,2	-9,1
Palbociclib	CHEMBL189963	-7,3	-8,1	-8,5	-7,3
Inavolisib	CHEMBL4286368	-8,4	-8,4	-8,3	-8,3
Ixabepilone	CHEMBL10318	-7,3	-7,3	-7,6	-7,3
Lapatinib	CHEMBL554	-9,1	-9,1	-9,1	-9
Olaparib	CHEMBL521	-9,3	-9,3	-9,4	-9,3
MegestrolAcetate	CHEMBL1928	-8,2	-8,2	-8,2	-8
methotrexate_sodium	CHEMBL198	-8,3	-7,8	-8,5	-8,1
NeratinibMaleate	CHEMBL18137	-8	-7,8	-7,9	-7,7
talazoparib_tosylate	CHEMBL3545119	-8,3	-8,2	-8	-8,3
Thiotepa	CHEMBL1201198	-4,6	-4,6	-4,6	-4,6
Tucatinib	CHEMBL3989868	-9,2	-10,6	-10,2	-9,1
LapatinibDitosylate	CHEMBL1201179	-8,9	-8,7	-9	-9
ACregimen	CHEMBL1486 + CHEMBL1453	-8,2	-8,2	-8,1	-8,2

raloxifene_hydrochloride	CHEMBL1069	-8,3	-8,1	-8,3	-8
AC-480	CHEMBL2097617	-9,5	-9,6	-9,6	-9,4
AEE-788	CHEMBL1201742	-8,9	-8,8	-9,2	-8,5
Afatinib	CHEMBL1749	-8,7	-8,7	-7,7	-8,2
Allitinib	CHEMBL2791551	-8,4	-9,4	-9,5	-9,4
BMS-690514	CHEMBL1175221	-7,3	-7,4	-7,2	-7,3
Canertrinib	CHEMBL1463	-7,8	-7,9	-8,1	-7,7
CP-724714	CHEMBL1614713	-8,7	-9,1	-9,1	-7,9
CUDC-101	CHEMBL1201194	-7,2	-7,3	-7	-7,8
Dacomitinib	ChEMBL2105719	-8,7	-9,1	-8,6	-8,4
JNJ-26483327	CHEMBL3545133	-7,6	-7,9	-7,8	-7,7
Lapatinib	CHEMBL554	-7,9	-9,1	-8,9	-8,2
Masoprocol	CHEMBL313972	-7,2	-6,9	-7,4	-7,2
MP-412	CHEMBL2138625	-8,7	-8,3	-8,6	-8,3
Mubritinib	CHEMBL1614707	-7,7	-8,8	-8,3	-7,6
Neratinib	CHEMBL18137	-8,2	-7,9	-8	-7,9
Pyrotinib	CHEMBL3647420	-8,2	-8,5	-8,6	-8,4
Sapitinib	CHEMBL2408045	-8,4	-8,4	-7,9	-8,1
Tak-285	CHEMBL1614725	-9	-9	-8,9	-8,6
Tesevatinib	CHEMBL3544983	-8,5	-9,3	-9,3	-8,1
Tucatinib	CHEMBL3989868	-9,5	-9,9	-9,9	-9,2
Tuxobertinib	CHEMBL4650279	-8,7	-9,2	-8,8	-8,6
Varlitinib	CHEMBL2103842	-8,9	-9	-8,9	-8,6
EPA	CHEMBL460026	-5,8	-5,7	-6,1	-6,2
DHA	CHEMBL367149	-4	-4,1	-4,1	-6,5

Table A.2. Docking results for the 7PCD receptor with Autodock Vina at 4 different locations

Receptor	**CHEMBL Code**	**Active Site Center**			
		20-20-20	**30-30-30**	**40-40-40**	**Co-crystalised ligand position**
Abemaciclib	CHEMBL3301610	-9,4	-10,3	-9,4	-10,2
nab-paclitaxel	CHEMBL428647	-12	-12	-11	-12
everolimus	CHEMBL1908360	-9,6	-9,7	-9,7	-9,7
alpelisib	CHEMBL2396661	-9,6	-9,6	-9,6	-9,6
anastrozole	CHEMBL1399	-6,9	-6,9	-6,8	-6,9
pamidronatedi-sodium	CHEMBL676	-5	-4,9	-4,9	-5
exemestane	CHEMBL1200374	-8,6	-8,6	-8,6	-8,6
capecitabine	CHEMBL1773	-7,6	-7,7	-7,6	-7,6
capivasertib	CHEMBL2325741	-8,9	-8,9	-8,9	-8,8
Cyclophosphamide	CHEMBL1453	-5,2	-5,2	-5	-5,2
doxorubicin_hydrochloride	CHEMBL1486	-8,1	-8,7	-8,7	-8,7

elacestrant_hydrochloride	CHEMBL4297509	-8,3	-8,3	-8,3	-8,4
epirubicin_hydrochloride	CHEMBL449442	-8,1	-9	-8,8	-9
fluorouracil	CHEMBL25	-4,6	-4,6	-4,6	-4,6
fulvestrant	CHEMBL2452	-8,7	-8,8	-8,4	-8,5
letrozole	CHEMBL1444	-7,8	-7,8	-7,8	-7,8
gemcitabine_hydrochloride	CHEMBL888	-7,3	-7,2	-7,3	-7,2
Trastuzumab	CHEMBL1201505	-9	-9,1	-9,2	-9,1
Palbociclib	CHEMBL189963	-9,7	-9,8	-9,8	-9,8
Inavolisib	CHEMBL4286368	-9	-9,7	-9,8	-9,7
Ixabepilone	CHEMBL10318	-5,7	-8,3	-6,9	-8,3
Lapatinib	CHEMBL554	-11	-11,1	-10,7	-11
Olaparib	CHEMBL521	-11,5	-11,5	-11,6	-11,5
MegestrolAcetate	CHEMBL1928	-8,7	-8,7	-7,2	-8,7
methotrexate_sodium	CHEMBL198	-9	-9,1	-9	-8,9
NeratinibMaleate	CHEMBL18137	-9,7	-9,7	-9,7	-9,7
talazoparib_tosylate	CHEMBL3545119	-9,3	-9,3	-8,3	-9,3
Thiotepa	CHEMBL1201198	-4,1	-4,1	-4,1	-4,1
Tucatinib	CHEMBL3989868	-11,8	-11,8	-11,7	-11,8
LapatinibDitosylate	CHEMBL1201179	-11,1	-11	-11,1	-10,8
ACregimen	CHEMBL1486 + CHEMBL1453	-8,1	-8,8	-8,7	-8,8
raloxifene_hydrochloride	CHEMBL1069	-9,3	-9,4	-9,3	-9,4
AC-480	CHEMBL2097617	-10,3	-10,5	-10,5	-10,5
AEE-788	CHEMBL1201742	-9,8	-9,9	-9,8	-9,9
Afatinib	CHEMBL1749	-8,7	-8,6	-8,7	-8,9
Allitinib	CHEMBL2791551	-10,4	-10,4	-10,3	-10,3
BMS-690514	CHEMBL1175221	-8,4	-8,4	-8,6	-8,3
Canertrinib	CHEMBL1463	-8,6	-8,3	-8,6	-8,5
CP-724714	CHEMBL1614713	-9,6	-9,7	-9,4	-9,6
CUDC-101	CHEMBL1201194	-9,4	-9,2	-9	-9,4
Dacomitinib	ChEMBL2105719	-10	-10,1	-9,3	-10,1
JNJ-26483327	CHEMBL3545133	-8,4	-8,5	-8,5	-8,5
Lapatinib	CHEMBL554	-10,8	-10,8	-9,7	-10,8
Masoprocol	CHEMBL313972	-8,3	-8,3	-8,3	-8,3
MP-412	CHEMBL2138625	-9	-9,3	-9,3	-9,3
Mubritinib	CHEMBL1614707	-9,6	-9,6	-9,7	-9,6
Neratinib	CHEMBL18137	-9,9	-10	-9,9	-9,9
Pyrotinib	CHEMBL3647420	-10,7	-10,7	-9,7	-10,7
Sapitinib	CHEMBL2408045	-8,9	-8,9	-8,8	-8,9
Tak-285	CHEMBL1614725	-10,1	-10,1	-9,9	-10,1
Tesevatinib	CHEMBL3544983	-9,1	-9,1	-9,2	-9,2
Tucatinib	CHEMBL3989868	-10,9	-10,9	-10,6	-10,9

Tuxobertinib	CHEMBL4650279	-8,6	-9,4	-9,2	-9,4
Varlitinib	CHEMBL2103842	-9,3	-9,3	-9,5	-9,5
EPA	CHEMBL460026	-6,6	-7	-6,7	-7,1
DHA	CHEMBL367149	-3,5	-3,7	-3,6	-7,3

Table A.3. Docking results for the 7PCD receptor with Autodock Vina at 4 different locations.

Receptor	**CHEMBL Code**	**Active Site Center**			
		20-20-20	**30-30-30**	**40-40-40**	**Co-crystalised ligand position**
Abemaciclib	CHEMBL3301610	-11,6	-11,5	-11,6	-11,4
nab-paclitaxel	CHEMBL428647	-12	-11,4	-11,3	-11,4
everolimus	CHEMBL1908360	-6	-9,1	-11,6	-9
alpelisib	CHEMBL2396661	-10,8	-10,8	-10,8	-10,8
anastrozole	CHEMBL1399	-8	-8	-8,1	-8
pamidronatedi-sodium	CHEMBL676	-5,3	-5,2	-5,4	-5,2
exemestane	CHEMBL1200374	-9,7	-9,7	-9,7	-9,7
capecitabine	CHEMBL1773	-8,4	-8,4	-8,3	-8,4
capivasertib	CHEMBL2325741	-9,9	-9,9	-8,5	-9,9
Cyclophosphamide	CHEMBL1453	-5,3	-4,8	-4,9	-4,9
doxorubicin_hydrochloride	CHEMBL1486	-7,6	-8,4	-8,4	-8,3
elacestrant_hydrochloride	CHEMBL4297509	-8,7	-9,1	-9,3	-9,2
epirubicin_hydrochloride	CHEMBL449442	-7,9	-8,7	-8,6	-8,7
fluorouracil	CHEMBL25	-5,7	-5,7	-5,7	-5,7
fulvestrant	CHEMBL2452	-9,9	-10,1	-10	-10,3
letrozole	CHEMBL1444	-7,9	-7,9	-7,9	-7,9
gemcitabine_hydrochloride	CHEMBL888	-8,2	-7,3	-7,4	-8,2
Trastuzumab	CHEMBL1201505	-9,4	-9,8	-9,4	-9,5
Palbociclib	CHEMBL189963	-9,6	-10,4	-10,2	-10,4
Inavolisib	CHEMBL4286368	-9,9	-9,8	-9,8	-9,9
Ixabepilone	CHEMBL10318	2,5	-6,9	-7,5	-5
Lapatinib	CHEMBL554	-11,8	-11,8	-11,9	-11,8
Olaparib	CHEMBL521	-11,9	-12	-10,9	-12
MegestrolAcetate	CHEMBL1928	-9,3	-9,3	-7,4	-9,3
methotrexate_sodium	CHEMBL198	-10,4	-10,4	-10,5	-10,4
NeratinibMaleate	CHEMBL18137	-8,9	-9,1	-9,1	-9,2
talazoparib_tosylate	CHEMBL3545119	-7,6	-7,6	-8,5	-7,6
Thiotepa	CHEMBL1201198	-4,3	-4,2	-4,2	-4,3
Tucatinib	CHEMBL3989868	-12,7	-12,8	-12,6	-12,7

LapatinibDitosylate	CHEMBL1201179	-11,8	-11,8	11,9	-11,8
ACregimen	CHEMBL1486 + CHEMBL1453	-7,6	-8,4	-8,4	-8,3
raloxifene_hydrochloride	CHEMBL1069	-9,8	-9,7	-9,7	-9,6
AC-480	CHEMBL2097617	-12,3	-12,4	-12,3	12,3
AEE-788	CHEMBL1201742	-11,2	-11,2	-11,3	-11,3
Afatinib	CHEMBL1749	-9,3	-9,3	-9,2	-9,3
Allitinib	CHEMBL2791551	-11,3	-11,3	-11,3	-11,3
BMS-690514	CHEMBL1175221	-9,1	-9,1	-9,1	-9,1
Canertrinib	CHEMBL1463	-9,3	-9,1	-9,1	-9,1
CP-724714	CHEMBL1614713	-11	-10,9	-10,9	-10,9
CUDC-101	CHEMBL1201194	-9,2	-8,5	-8,7	-9
Dacomitinib	ChEMBL2105719	-10,1	-10,1	-9,7	-10,1
JNJ-26483327	CHEMBL3545133	-10,7	-10,7	-9,8	-10,6
Lapatinib	CHEMBL554	-11,8	-11,8	-11,6	-11,7
Masoprocol	CHEMBL313972	-9,2	-9,2	-9,2	-9,2
MP-412	CHEMBL2138625	-9,9	-10,3	-10,3	-10,3
Mubritinib	CHEMBL1614707	-10,3	-10,2	-10,1	-10,2
Neratinib	CHEMBL18137	-9,1	-9,4	-9,4	-9,5
Pyrotinib	CHEMBL3647420	-9,4	-9,7	-9,6	-9,7
Sapitinib	CHEMBL2408045	-9,6	-8,9	-8,9	-8,9
Tak-285	CHEMBL1614725	-11,1	-11,1	11,1	-10,6
Tesevatinib	CHEMBL3544983	-10,9	-10,9	11	-10,9
Tucatinib	CHEMBL3989868	-12,6	-12,6	12,6	-12,6
Tuxobertinib	CHEMBL4650279	-9,9	-10,3	-10,2	-10,3
Varlitinib	CHEMBL2103842	-10,4	-10,5	-10,4	-10,4
EPA	CHEMBL460026	-7,8	-7,7	-7,6	-7,7
DHA	CHEMBL367149	-4,3	-4,3	-4,3	-8,0